WIND-TUNNEL-WALL EFFECTS AND SCALE EFFECTS ON A VTOL CONFIGURATION WITH A FAN MOUNTED IN THE FUSELAGE

by Edwin E. Davenport and Richard E. Kuhn

Langley Research Center
Langley Station, Hampton, Va.

WIND-TUNNEL-WALL EFFECTS

AND SCALE EFFECTS ON A VTOL CONFIGURATION WITH

A FAN MOUNTED IN THE FUSELAGE

By Edwin E. Davenport and Richard E. Kuhn

Langley Research Center
Langley Station, Hampton, Va.

NATIONAL AERONAUTICS AND SPACE ADMINISTRATION

WIND-TUNNEL-WALL EFFECTS

AND SCALE EFFECTS ON A VTOL CONFIGURATION WITH

A FAN MOUNTED IN THE FUSELAGE

By Edwin E. Davenport and Richard E. Kuhn
Langley Research Center

SUMMARY

13574

An investigation of the aerodynamic characteristics of a model of a VTOL configuration with a lifting fan mounted in the fuselage has been conducted to determine the effects of scale and the effects of tunnel walls on the characteristics of this configuration, which had previously been investigated at full scale. The investigation was conducted in three phases: first, in the 17-foot test section of the Langley 300-MPH 7- by 10-foot tunnel in which significant differences between the model and full-scale results were found; second, in the 4.4- by 7.0-foot test section of the same tunnel to determine wall effects; and third, in the 4.4- by 7.0-foot test section to obtain detailed pressure distributions on the wing and fuselage to determine regions of possible scale effect.

The results of the investigation indicate that significant wall effects were encountered with the model in the small test section and with the full-scale configuration in the Ames 40- by 80-foot tunnel, and that adequate corrections for these wall effects could be made by Heyson's wall-correction theory (NASA TR R-124).

After correcting both model and full-scale data for wall effects and after considering differences in vane characteristics, the data with exit vanes deflected were in good agreement. However, with the vanes undeflected, significant differences between the model and full-scale data remain. These differences were found to be largely due to differences in the suction pressures induced on the bottom of the fuselage behind and beside the jet; and, to a smaller extent, to differences in the model and full-scale power-off characteristics; and to differences in the inlet mass flow for the model and full-scale configuration.

The differences between the model and full-scale suction pressures, induced on the lower surface of the fuselage by the exiting jet, were opposite to those expected on the basis of Reynolds number effects on the flow around a circular cylinder. The need for additional investigations of the effects of various obstructions near the exiting jet on the suction pressures induced by a jet is indicated. A large part of the wing lift induced on the model and the full-scale configuration at zero angle of attack was found to be due to the wall-induced upwash field in which the wing was operating.

INTRODUCTION

Wind-tunnel investigations of models have always been subject to some limitations due to the artificial boundary conditions created by the tunnel walls and to Reynolds number effects. With conventional airplane configurations these limitations have long been recognized. However, the previous experience is not always a sufficient guide in V/STOL investigating for several reasons. First, the wall effects are exaggerated by the large downwash angles associated with V/STOL configurations, and secondly, many of the V/STOL configurations embody features on which the effects of Reynolds number are unknown.

Investigations reported in references 1 and 2 have indicated that the "lift droop" phenomena associated with jet and buried-fan configurations (caused by suction pressures induced on the lower surface of the model by the exiting jet (refs. 3 and 4)) may be strongly influenced by scale effects. A direct comparison of large- and small-scale data is necessary in order to determine whether or not scale effects are significant on a particular type of configuration. The present investigation of a configuration with a lifting fan mounted in the fuselage was made because detailed large-scale data, particularly pressure distributions over the fuselage and wing, were available from investigations made in the Ames 40- by 80-foot tunnel (ref. 5).

The investigation was conducted in three phases: first, a 1/9-scale model of the fan-in-fuselage configuration was investigated in the 17-foot test section of the Langley 300-MPH 7- by 10-foot tunnel, in which significant differences between model and full-scale results were found; second, the same model was investigated in the 4.4- by 7.0-foot test section to investigate the possibility of tunnel-wall effects; and third, detailed pressure-distribution surveys were made over wing and fuselage and at fan inlet and exit to determine areas of significant scale effect.

SYMBOLS

A_F effective fan-exit area, $\frac{\pi}{4}\left(d_1^2 - d_2^2\right)$, 0.230 sq ft

b wing span, 3.92 ft

c wing chord, ft

$\bar{c}$ mean aerodynamic chord, 0.814 ft

C_D drag coefficient, D/qS

C_L lift coefficient, L/qS

C_m pitching-moment coefficient, $M/qS\bar{c}$

D	complete model drag, measured on main balance, lb
d_1	fan-shroud inside diameter, 7 in.
d_2	fan hub diameter, 2.6 in.
L	complete model lift, measured on main balance, lb
$L_{(\delta_v=0)}$	lift at zero exit-vane deflection, lb
M	complete model pitching moment, measured on main balance, ft-lb
N	fan rotational speed, rpm
n	fan rotational speed, rps
p_{atm}	atmospheric pressure, lb/sq ft
p_{st}	local static pressure, lb/sq ft
p_t	local total pressure, lb/sq ft
$p_{t,\infty}$	free-stream total pressure, lb/sq ft
q_∞	free-stream dynamic pressure, lb/sq ft
R	fan radius, 3.5 in.
r	local radius from fan axis, in.
S	wing area, 3.08 sq ft
T	fan thrust, normal force reading on fan beams, lb
T_o	fan thrust, normal force reading on fan beams at $\alpha = 0^o$ and $\delta_v = 0^o$, lb
V_j	jet-exit velocity, $\sqrt{\dfrac{T_o}{\rho A_F}}$, ft/sec
V_∞	free-stream velocity, ft/sec
y	spanwise distance perpendicular to plane of symmetry, ft
α	angle of attack, with reference to wing chord plane, deg

δ_v exit-vane deflection angle measured from fan rotational axis, positive deflection rearward, deg

η fraction of wing semispan, $2y/b$

θ turning angle of fan efflux measured from fan rotational axis, deg (see fig. 20)

ρ mass density, slugs/cu ft

ϕ radial station, deg (see fig. 28)

ΔC_L incremental lift coefficient obtained from wing pressure data,

$$C_{L\left(\frac{V_\infty}{V_j}\right)} - C_{L\left(\frac{V_\infty}{V_j}\right)=\infty}$$

$$\Delta L = \Delta C_L qS$$

MODEL AND APPARATUS

The model was a 1/9-scale version of the wing-fuselage configuration of reference 5. A drawing of the model, which did not incorporate a tail assembly, is shown in figure 1. A photograph of the model mounted in the 15.7- by 17.0-foot test section (hereinafter referred to as the 17-foot test section) is shown in figure 2. The fuselage consisted of a glass-fiber outer shell, to form the contour, supported by a steel and aluminum internal frame. This frame was in turn supported by a sting-mounted strain-gage balance with the sting being supported by a strut attached to a ceiling turn table. The wing employed an aluminum spar and was covered with wood to provide the contour of the NACA 63A210 airfoil section.

The fan used in the model was not constructed to scale, but was a commercially available unit. The fan was driven by high-pressure air jets exhausting from the tip of each of the four blades. Drive air for the fan was brought into the model through a 1/2-inch-diameter copper tube which was coiled around the fan to provide a flexible spring in the system for minimum interaction with the strain-gage balances. The air was brought into the hub support member through the forward strut and fed through the fan hub and through passages in the blades to the blade tips. The mass flow of air required to drive the fan was measured by a standard sharp-edge flow meter, and the pressure of the driving air was calibrated against the hub pressure which was measured for all tests. The rotational speed of the fan was measured by a pressure gage mounted in the shroud wall situated so as to pick up the pressure pulse of the passing fan blade. The fan inlet was constructed to scale and included an inlet guide vane. A set of exit vanes was included, but because of their small size, the vanes did not incorporate the scaled airfoil section. As shown in figure 3, the vanes consisted of flat stock 3/32 inch thick with a beveled trailing edge.

The entire fan, inlet, and exit-vane assembly was mounted on strain-gage beams to measure the fan thrust independently of the forces measured by the main model balance. A sponge seal was incorporated as shown in figure 3 to prevent air leakage through the joint between the inlet and the fuselage surface.

Insofar as possible pressure orifices were installed in the model at the same locations used in the full-scale investigation. These pressure orifices were connected to alcohol manometer boards, which were photographed to record the data. The photographs were read on special equipment which transcribed the data to punch cards for machine calculation.

For the wall-effects investigation, a special liner was installed in the throat of the Langley 300-MPH 7- by 10-foot tunnel to form a small test section. (See figs. 4 and 5.) This small test section was intended to approximate the Ames 40- by 80-foot tunnel in proper scale to the model. The height of the tunnel, 4.44 feet, was to scale; however, the semicircular ends of the tunnel were not incorporated, and the cross-sectional area of the small test section (hereinafter referred to as the 4.4- by 7.0-foot test section) was slightly less (31.10 square feet) than the scaled cross-sectional area (35.18 square feet) of the 40- by 80-foot tunnel. As shown in figure 5, the support struts for the model in the full-scale tunnel were also simulated.

The exit rake used to measure pressure distribution in the fan exit consisted of static- and total-pressure tubes at eight radial stations, which were 45° apart. Each radial station had four total-pressure tubes with a static tube offset about 3/4 inch from the row. The tubes were made from 1/16-inch-outside-diameter copper tubing and were supported by a steel wire grid.

The inlet rake used to measure pressure distribution in the fan inlet consisted of total- and static-pressure tubes at eight radial stations located 45° apart. All but the three rearmost stations had six total-pressure tubes and one static tube offset about 3/4 inch from the radial row. The three rearmost groups (at ϕ = 135°, 180°, and 225°) had only five total-pressure tubes with a static tube offset as before. The 1/16-inch-outside-diameter copper tubes used for the rake were supported by a steel wire grid built into the fan inlet.

TESTS AND PROCEDURE

Most of the tests were run at a fan speed of 20,000 rpm, and the tunnel speed was varied to achieve the desired velocity ratio. A few tests were run at reduced speeds of 12,000 and 16,000 rpm to determine the possible effects of fan disk loading. The investigation covered a range of angle of attack from -4° to 16° and a range of tunnel free-stream dynamic pressures from 0 to 18 pounds per square foot with corresponding free-stream velocities varying from 0 to 123 feet per second.

The airflow alinement angle for the 17-foot test section and the 4.4- by 7.0-foot test section of the Langley 300-MPH 7- by 10-foot tunnel was determined

by power-off tests of the model (with the inlet and exit sealed) by the standard technique of testing the model upright and inverted.

RESULTS AND DISCUSSION

Fan Characteristics

A comparison of the model and full-scale fan thrust coefficients for the disk loading range investigated is shown in figure 6. The mass flow and the hub pressures required to drive the model fan are shown in figure 7. The total-pressure distribution under static conditions at the model fan exit is shown in figure 8 and is considerably different than the distribution at the full-scale fan exit, which reached a maximum about midway between the hub and the tip. The model experienced a small region of reverse flow near the hub and extremely high velocities due to the driving jets on the outer wall.

Inasmuch as the fan was not constructed to scale it was not feasible to use the tip-speed ratio used in the full-scale investigation, as a nondimensional forward-speed parameter. For the purposes of presenting the model data and comparing the model data with the full-scale data, the ratio of free-stream velocity to jet velocity V_∞/V_j has been used in this investigation. The jet velocity is determined from the expression $V_j = \sqrt{T_o/\rho A_F}$, where the fan thrust T_o was determined by mounting the fan, inlet, and exit-vane assembly on strain-gage beams.

The primary problem of such an installation is determining where the inlet, in effect, stops and the fuselage begins. For the present investigation the inlet was assumed to extend to the point of tangency with the basic fuselage contour, which is the line shown in figure 1. In order to determine the adequacy of this assumption, the fan, installed in the model, was tested statically, and the thrust measured on the fan beams was compared with the model lift measured on the main balance. As can be seen in figure 9, all but 3 percent of the fan thrust is measured on the fan beams. The fan-thrust data have not been corrected for this; in all cases T_o is the actual load measured on the fan beams.

As a further check on the adequacy of the fan and inlet mounting system at forward speeds, the jet-exit velocity distribution was integrated for both static and forward-speed conditions. The thrust thus obtained is shown in figure 10 as the fan-exit momentum. At $V_\infty/V_j = 0$, there is a difference of 10 pounds between the fan-exit momentum and the thrust measured on the fan balance. This difference is due to the residual thrust of the tip jets which drive the fan. Inasmuch as the hub pressure and mass flow required to drive the fan decrease with forward speed (fig. 7(b)), this residual thrust also decreases. The residual thrust has been assumed to be a direct function of hub pressure and has been added to the measured fan-exit momentum. The resulting variation of thrust with forward velocity $\left(V_\infty/V_j\right)$ is in reasonably good agreement with the measured fan thrust, as shown in figure 10.

The difference between the static thrust values shown in figures 9 and 10 and the difference between the thrust obtained in the 17-foot test section and that obtained in the 4.4- by 7.0-foot test section are due to the losses caused by the inlet rake, which was not installed during the initial static calibration (fig. 9) or during the tests in the 17-foot test section. A typical comparison of the mass flow required to drive the fan through the speed range with the mass flow through the fan itself is shown in figure 11.

Effect of Disk Loading

The basic data of the investigation are presented in figures 12 to 16. Figures 12, 13, and 14 present the model data for three disk loadings as measured in the two test sections for a vane deflection angle of 0°. Figure 15 presents the data for the highest disk loading with the vanes deflected 30°, and figure 16 presents the data for the wing-off condition. A comparison of the data for different disk loadings through the velocity-ratio range at zero angle of attack is presented in figure 17. Within the accuracy of the data, there is no recognizable effect of disk loading within the range covered in this investigation.

Wall Effects

The data in figure 17 indicate that there is a significant wall effect on lift, as much larger values were measured in the 4.4- by 7.0-foot test section than in the 17-foot test section. Similar wall effects for a fan-in-wing configuration are presented in reference 6.

The data from the small test section have been corrected to the free-air condition by the method of reference 7 and are compared with the data from the large test section in figure 18. A sample calculation for the data at zero angle of attack in figure 18(c) is given in the appendix. Because of the small size of the model with respect to the tunnel in the large test section (ref. 6), these data represent essentially the free-air condition. The generally good agreement between the data from the 17-foot test section and the corrected data from the smaller test section indicates the adequacy of the method of reference 7. It should be pointed out that this observation applies only to the tail-off condition. As shown in reference 6, wall effects on the downwash at the tail are not correctly predicted by the method of reference 7.

Scale Effects

Power-off data.- A comparison of the model data with the full-scale data (ref. 5) for power off and for the fan inlet and exit sealed is presented in figure 19. The large difference in drag coefficient at zero lift is probably due to the externally mounted engine on the full-scale configuration. The engine and its associated support and accessories were not simulated on the model. The maximum lift coefficient of the model is lower than that of the full-scale configuration, as would be expected, because of the lower Reynolds

number. Although the lift-curve slope is in excellent agreement, there is a significant difference in the level of the lift coefficient. The reason for this difference is not known. The flow-alinement tests for the model were repeated when this difference was first encountered, but no significant difference in the flow angle was found.

Static data.- The effectiveness of the exit vanes in deflecting the fan-exit flow is presented in figure 20. The larger turning losses experienced by the model vanes are to be expected as a result of the "flat plate" airfoil section used on the model and the lower Reynolds number. The slightly lower slope of the variation of moment with vane deflection angle for the model is due to the lower forward component of the thrust vector (larger turning losses) obtained by the model.

The pitching-moment data for the full-scale configuration, as presented in reference 5, did not give zero moment at zero deflection. All the static data obtained in the full-scale tests were taken in the test section of the Ames 40- by 80-foot tunnel and considerable recirculation of the flow was experienced. The lift and drag data presented in reference 5 were adjusted to correct for the effects of this recirculation but the pitching-moment data were not. Apparently, the pitching moment measured at zero deflection (ref. 5) is due to these recirculation effects. The full-scale data presented in figure 20 have been adjusted to zero moment at zero deflection to correct for recirculation effects.

Power-on data.- The data from the present investigation are compared with the full-scale data in the transition speed range in figure 21. For the purpose of this comparison, the full-scale data have been corrected for wall effects by the method of reference 7. A cross plot of the data as a function of velocity ratio at zero angle of attack is presented in figure 22. As can be seen, there are significant differences in lift, L/T_O, and some differences in drag, D/T_O, remaining after all of the data have been corrected for wall effects. Part of the difference can be due to the differences in lift and drag characteristics of the model and full-scale configuration in the power-off condition, as shown in figure 19; however, this only accounts for about one-third of the difference between the model and full-scale values of L/T_O.

The agreement is considerably better for the condition of an exit-vane deflection angle of 30° than for a vane deflection of 0°, as shown in figure 22. Most of the differences between the model and full-scale data for an exit-vane deflection angle of 30° are a result of the differences in the vane effectiveness shown in figure 20.

Inlet characteristics.- The pressure recovery of the model inlet is compared with that of the full-scale inlet in figure 23(a). The model inlet losses were higher than the full-scale inlet losses; however, these are presented in terms of free-stream dynamic pressure and represent extremely small losses. The difference in inlet recovery for the model and full-scale configuration could not cause significant differences in the overall model force data.

Most of the total-pressure losses experienced by the inlet occurred on either side as shown in figure 23(b). The magnitude of the losses encountered in the extremely small areas indicates a vortex type of flow. Tuft studies indicated a vortex type of flow originating at the wing-fuselage juncture and entering the inlet at about the location shown. The observed inlet loss could be due to this flow or to the tip vortex from the inlet vane or to a combination of both.

Wing lift.- Pressure distributions were taken on the wing at the stations indicated in figure 24, which are the same stations used in the full-scale investigation. The resulting pressures were machine integrated and compared with the full-scale data in figure 25.

Both the model and the full-scale pressure-distribution data were obtained from tests in which wall effects were present. The wings would therefore be at an angle of attack due to the wall-induced upwash. The lift that would be generated on the wing due to the wall-induced upwash was calculated by means of the following equation:

$$\Delta L = \frac{\Delta C_L}{\Delta \alpha} \Delta \alpha q S$$

where $\Delta \alpha$ is computed by the theory of reference 7. A comparison of this calculated lift with the measured wing lift from the pressure distributions is given at the bottom of figure 25. This comparison clearly indicates that most of the wing lift, both model and full scale, is due to the wall-induced upwash rather than being induced by the fan inlet and exit flow. The slightly greater wall-induced lift for the full-scale configuration is due to the larger values of L/T_0 for the full-scale configuration (fig. 21).

The measured wing lift determined from pressure distributions is compared in figure 26 with the lift determined from force tests of the model with and without the wing in the small test section. The wing-off data are in good agreement with the data for the complete model in the 17-foot test section; thus, the data indicate that in the 17-foot test section, the wing lift was negligible. Subtraction of the wing lift, determined from pressure distributions, from the complete model data measured in the small test section results in a curve that is in fair agreement with that for the wing-off lift measured during force tests.

A similar comparison is shown for the full-scale configuration in figure 27. When the wing lift (as determined from pressure distributions) is subtracted from the uncorrected lift data for the complete full-scale configuration, the "wing-off" configuration (fuselage plus fan) exhibits an increase in lift-thrust ratio with speed; this phenomenon implies that there are lifting pressures on the fuselage of the full-scale configuration that are not accounted for in the exit momentum.

Fuselage pressure distributions.- Detailed pressure distributions were taken over the top and bottom of the fuselage at the points shown in figure 28. These data are presented in figure 29 to 34. These pressures are relatively

insensitive to angle of attack and, therefore, would not be influenced by wall effects. The pressures on the top and bottom of the model fuselage near the center line are generally in good agreement with the full-scale data for all exit-vane deflection angles investigated. The only exception are the pressures on the bottom of the fuselage ahead of the fan exit for the lowest velocity ratio investigated $\left(V_\infty/V_j \approx 0.15\right)$. In this region, the model suction pressure ratios $\left(\dfrac{p_{t,\infty} - p_{st}}{q_\infty}\right)$ are significantly greater than those for the full-scale configuration. However, these high pressure ratios occur at such a low free-stream dynamic pressure that the forces generated are negligible.

Because of the steep pressure gradients that can be encountered close to an exiting jet, the pressures on the lower surface beside the jet were measured along radials as shown in figure 28. The model orifices were located in this manner because of some uncertainty as to the exact lateral location of the pressure orifices used in the full-scale investigation. At exit-vane deflections of 20° and 35° the data (figs. 33 and 34) are in reasonable agreement. At a vane deflection of 0° (fig. 32), however, the suction pressures measured in the full-scale investigation are significantly lower than those measured on the model. The data for $\delta_V = 0^O$ are also compared with pressures measured on a large flat plate surrounding a jet. In comparison with the present model, which had relatively little surface area surrounding the jet, the flat-plate results can be considered as those for a plate that was almost infinite in extent. As can be seen by the agreement between the results for the present model and those for the flat plate, there is apparently little effect of the extent of the surface area surrounding the exiting stream.

The pressure distributions along the lower fuselage surfaces of the model and the full-scale configuration were not sufficiently detailed to determine the exact area over which significant differences in pressures occurred. On the basis of the pressure data available and in order to determine whether these pressure differences could cause significant differences in the overall force data, it was assumed that significant differences existed between the model and full-scale pressures in the regions indicated in the sketch at the top of figure 35. As shown at the bottom of figure 35, a pressure difference of two times the free-stream dynamic pressure occurring over the assumed area could cause a change in the lift-thrust ratio of the same order of magnitude as the difference between the model and full-scale values at $\delta_V = 0^O$ in figure 22(a). With the vanes deflected, the pressure data, as well as the force data, are in good agreement (fig. 22(b)).

Summary of model and full-scale comparisons.- A summary comparison of the lift data in terms of L/T_O at zero angle of attack as a function of velocity ratio is presented in figure 36. As shown, wall corrections to the full-scale data account for about half of the difference between the full-scale data and the model data obtained in the large test section. The combination of the suction pressure difference and the difference in the power-off lift accounts for most of the remaining difference.

10

A similar comparison for drag in terms of D/T_O is shown in figure 37. The suction pressures on the bottom of the fuselage would, of course, have a negligible effect on the drag. However, either the difference in the power-off drag, due to the fact that the engine was not simulated on the model, or the difference in mass flow into the inlet, due to the fact that the model was driven by compressed air so that all of the exiting mass flow did not come in through the inlet, could account for the difference between the model and the full-scale drag parameters.

With regard to pitching moments in terms of $M/T_O\bar{c}$, there are four differences between the model and the full-scale data that must be accounted for. These are shown at the bottom of figure 38. Correcting the power-off data of the model to agree with the full-scale data would add a nose-up increment in pitching moment. Correcting the model data for the fact that the ram inlet drag of the externally mounted engine was not present on the model would contribute a diving-moment increment. Likewise, correcting the lower surface pressures, which account for a large part of the difference between the model and full-scale lift, would contribute a diving-moment increment. The fourth term is the additional nose-up moment that would be experienced due to the additional mass flow at the main inlet. As shown in figure 11, the main inlet of the model took in 80 to 85 percent of the total mass flow (the fan drive air was 15 to 20 percent of the total), whereas the full-scale inlet took in 90 percent of the total mass flow (the externally mounted engine mass flow was about 10 percent of the total). Thus, the main inlet on the full-scale configuration was taking in 10 percent more air in hovering and 5 percent more air at the velocity ratio of 0.49. The additional nose-up moment created by this additional mass flow has been estimated by the method of reference 8 to be a relatively small factor, as shown at the bottom of figure 38. These four corrections to pitching moment tend to compensate for each other, and their summation results in a relatively small increment which, as shown at the top of figure 38, tends to improve the agreement between the model and full-scale data.

Factors affecting jet-exit induced pressures.- The preceding discussion has shown that the difference between the suction pressures measured on the model and on the full-scale configuration on the lower surface can account for most of the differences in the lift characteristics after accounting for wall effects; however, the question remains as to whether the cause of these differences in suction pressures is a scale effect of the type normally attributed to Reynolds number effects or is due to some physical differences between the model and the full-scale configuration.

The flow around a jet issuing from the lower surface of a fuselage or wing has been described by analogy to the flow around a circular cylinder. That is, the free-stream flow must accelerate in flowing around the cylinder or jet of air, and in doing so creates regions of suction pressure on the cylinder and on the surface surrounding the cylinder or jet of air. (The flow around a cylinder is a poor analogy to use because the jet does not stay circular but is flattened and bent back by the action of the free stream (ref. 9). Nevertheless, the cylinder analogy is discussed here because it has been so frequently used in discussing jet-induced effects.) In the case of the jet, the additional factor of

the entrainment action of the jet also contributes to the creation of suction pressures and, in particular, to the increase of suction pressures behind the jet (ref. 4).

Figure 39 shows that the cross-flow Reynolds number based on the free-stream velocity and the jet diameter for the full-scale investigation is much greater than the critical Reynolds number for the flow around a circular cylinder, whereas the Reynolds number for the model investigations is lower than the critical Reynolds number. For the case of the circular cylinder (ref. 10), as the Reynolds number is decreased from the supercritical to the subcritical condition, the pressures induced on the sides of the cylinder are decreased; whereas, the pressures in the wake, that is, the downstream side of the cylinders, are increased (fig. 40). The opposite characteristic was found for the fan-in-fuselage configuration. The plot at the bottom of figure 40 shows that the pressures on the bottom of the full-scale fuselage at $r/R = 1.4$ are lower than those on the model at an exit-vane deflection angle of 0°. At a vane-deflection angle of 20°, as was shown in figures 32 to 34, model and full-scale results are in good agreement.

Although it is not expected that the critical Reynolds number for the flow around an exiting jet would be the same as the Reynolds number for a circular cylinder, the results presented herein do suggest that the differences between the model and full-scale pressures may be due to physical differences of the models rather than to Reynolds number effects. The model differed from the full-scale configuration physically in two significant respects. The external engine mounting and the attachment and accessory items were not simulated on the model, and the approximately 150° quadrant of the exit from the drive turbine of the fan in the full-scale configuration was not simulated. These items were on the opposite side of the exit from that on which the pressures were measured. Reference 11 indicates that deep lower surface fences forward of the jet efflux significantly alter the lift characteristics. There is considerable difference between the fuselage-mounted fences of reference 11 and the externally mounted engine and appendages of reference 5; nevertheless, the data of reference 11 indicate that obstructions in these areas can have significant effects. In addition, the velocity distribution from the model fan was grossly different than that from the full-scale fan, and may be a significant contributor in the present case. Also, the gap between the fan exit and the fuselage was not sealed. There is currently no information on the effects of a flow induced by the jet through this gap on the induced pressure distribution. In any event, the need for additional investigations of the effects of Reynolds number, jet-velocity distribution, and obstructions on the pressures induced on a surface surrounding an exit jet is clearly indicated.

Thrust measurements.- Although the preceding sections have discussed factors that explain most of the differences between the model and full-scale results, the importance of accurate measurement of the fan or jet thrust under all test conditions cannot be minimized. The determination of the thrust by the survey of the exiting stream requires the integration of a large number of pressure readings but remains the only sure way of determining the exit momentum provided a sufficient number of readings are taken. The strain-gage mounting of the fan inlet and exit assembly, as used in the present investigation,

12

appears to have been successful; however, for any particular installation there always remains the problem of how much of the inlet to include on the strain-gage mounting. Careful check-out and calibration of the system employed are required, including detailed surveys of the exiting momentum during at least some of the tests over the range of conditions investigated.

CONCLUSIONS

The results of an investigation of wind-tunnel-wall effects and scale effects on a VTOL configuration with a fan mounted in the fuselage indicate the following conclusions:

1. Significant wall effects were encountered with the model in the 4.4- by 7.0-foot test section of the Langley 300-MPH 7- by 10-foot tunnel; corrections for these wall effects can be made by Heyson's wall-correction theory (NASA TR R-124).

2. After correcting both model and full-scale data for wall effects and after considering differences in vane characteristics, the data with exit vanes deflected were in good agreement. However, with the vanes undeflected, significant differences between the model and full-scale data remain. These differences were found to be largely due to differences in the suction pressures induced on the bottom of the fuselage behind and beside the jet; and, to a smaller extent, to differences in the model and full-scale power-off characteristics; and to differences in the inlet mass flow for the model and full-scale configuration.

3. Differences between the model and full-scale suction pressures, induced on the lower surface of the fuselage by the exiting jet, were opposite to those expected on the basis of the effects of Reynolds number on the pressures induced on a cylinder. The present results indicate the need for additional investigation of the effects of Reynolds number, exit velocity distribution, and various obstructions in the vicinity of the jet, on the suction pressures induced on a surface by an exiting jet.

4. The wing lift induced on both the model and the full-scale configuration was mostly due to the wall-induced upwash field in which the wing was operating.

Langley Research Center,
National Aeronautics and Space Administration,
Langley Station, Hampton, Va., September 15, 1964.

APPENDIX

APPLICATION OF WALL CORRECTIONS

This appendix illustrates, by means of a sample calculation, the procedures and assumptions used in applying the wall corrections of reference 7 to the data obtained in the 4.4- by 7.0-foot test section of the Langley 300-MPH 7- by 10-foot tunnel. The symbols used in this appendix are defined as follows:

A_m momentum area of lifting system, sq ft

A_T cross-sectional area of wind-tunnel test section, sq ft

$\bar{c}$ mean aerodynamic chord, ft

D total drag, lb

D_c corrected value of total drag, lb

D_i induced drag, positive rearward (note that a forward-directed longitudinal thrust is considered in this context as a negative induced drag), lb

L lift, lb

L_c corrected value of lift, lb

M pitching moment, ft-lb

M_T mass flow through wind tunnel, $\rho A_T V$, slugs/sec

M_u longitudinal mass flow due to induced drag, $\rho A_m u_0$, slugs/sec

M_w vertical mass flow due to lift, $\rho A_m w_0$, slugs/sec

n ratio of final induced velocities in far wake to initial induced velocities at model

q dynamic pressure, $\frac{1}{2}\rho V^2$, lb/sq ft

T_0 fan thrust, normal force reading on fan beams at $\alpha = 0^{\circ}$ and $\delta_v = 0^{\circ}$, lb

u_0 mean or momentum-theory value of longitudinal induced velocity at model, positive rearward, ft/sec

Δu total longitudinal interference velocity, positive rearward, ft/sec

Δu_D longitudinal interference velocity due to induced drag, positive rearward, ft/sec

Δu_L longitudinal interference velocity due to lift, positive rearward, ft/sec

V wind-tunnel velocity, ft/sec

V_j jet-exit velocity, ft/sec

V_∞ free-stream velocity, ft/sec

w_h reference velocity, positive upward, $-\sqrt{\dfrac{L}{n\rho A_m}}$, ft/sec

w_L vertical induced velocity due to lift, positive upward, ft/sec

w_O mean or momentum-theory value of vertical induced velocity, positive upward, ft/sec

Δw total vertical interference velocity, positive upward, ft/sec

Δw_D vertical interference velocity due to induced drag, positive upward, ft/sec

Δw_L vertical interference velocity due to lift, positive upward, ft/sec

α angle of attack, deg

α_c corrected angle of attack, deg

$\Delta \alpha$ change in angle of attack due to interference, deg

γ ratio of tunnel semiwidth to tunnel semiheight, $\dfrac{3.50}{2.22}$

$\delta_{u,D}$ interference factor for longitudinal interference velocity due to drag

$\delta_{u,L}$ interference factor for longitudinal interference velocity due to lift

δ_v exit-vane deflection angle measured from fan rotational axis, positive deflection rearward, deg

$\delta_{w,D}$ interference factor for vertical interference velocity due to drag

$\delta_{w,L}$ interference factor for vertical interference velocity due to lift

ζ ratio of tunnel semiheight to height of model above tunnel floor, $\dfrac{2.22}{2.22}$

η ratio of lateral distance between model center and right-hand side of wall (viewed from behind) to semiwidth of tunnel, $\dfrac{3.5}{3.5}$

ρ mass density of air, slugs/cu ft

X wake skew angle, angle between vertical axis (negative direction) and wake center line, positive rearward, deg

In applying the wall corrections of reference 7, it is necessary to determine the momentum area appropriate to the model. The momentum area is the cross-sectional area of the wake from the lifting element of the model. For a buried-fan or jet configuration in the near-hovering and transition condition, most of the lift is produced by the fan or jet; therefore, the fan exit area represents the appropriate momentum area. The wall-correction calculations for the present model were made by using the fan-exit area and the single-point calculation method from reference 7.

The following characteristics of the wind tunnel are assumed:

$A_m = 0.268$ sq ft

$n = 1.00$

$A_T = 30.80$ sq ft

$\gamma = 1.58$ (used 1.5)

$\zeta = 1.00$

$\eta = 1.00$

The sample point (represented by the solid symbols in fig. 18(c)) was computed for the following conditions:

$V_\infty / V_j = 0.40$

$q = 10.62$ lb/sq ft   or $V_\infty = 96.60$ ft/sec

$\alpha = -0.16^\circ$

$L = 33.50$ lb

$D = 14.80$ lb   and D_i is assumed to be 14.80 lb

$T_0 = 31.10$ lb

16

The following steps are then followed in the sample calculation:

$$\frac{D_1}{L} = 0.4418$$

From equation (35) of reference 7,

$$w_h = -\sqrt{\frac{L}{n\rho A_m}} = -\sqrt{\frac{33.50 \text{ lb}}{(1.0)(0.00238 \text{ slug/cu ft})(0.268 \text{ sq ft})}} = 229.50 \text{ ft/sec}$$

$$\frac{V}{w_h} = \frac{94.60 \text{ ft/sec}}{-229.50 \text{ ft/sec}} = -0.4122$$

From figure 6 of reference 7,

$$\frac{w_o}{w_h} = 1.00 \quad \text{and} \quad \frac{V}{w_o} = -0.41$$

From figure 7 of reference 7,

$$X = 0°$$

From the wing-span load distribution obtained from wing pressure data, it was determined that the lateral center of lift was located spanwise at $\frac{y}{B} = 0.30$, where y is a point on the lateral axis, measured positive to right when viewed from behind, and B is the semiwidth of the tunnel.

From figure 49(b) of reference 7 and by considering $\frac{y}{B} = 0.30$,

$$\delta_{w,L} = -1.32$$

From figure 50(b) of reference 7,

$$\delta_{u,L} = 0$$

From figure 51(b) of reference 7,

$$\delta_{w,D} = -1.35$$

From figure 52(b) of reference 7,

$$\delta_{u,D} = -0.29$$

From equation (44) of reference 7,

$$\frac{M_W}{M_T} = \frac{A_m/A_T}{V/w_0} = -0.02114$$

From equation (45) of reference 7,

$$\frac{M_u}{M_T} = \frac{M_W}{M_T}\frac{D_i}{L} = (-0.02114)(0.4418) = -0.0093$$

$$\frac{\Delta w_L}{V} = \delta_{w,L}\frac{M_W}{M_T} = (-1.32)(-0.02114) = 0.0279$$

$$\frac{\Delta u_L}{V} = \delta_{u,L}\frac{M_W}{M_T} = (0)(-0.02114) = 0$$

$$\frac{\Delta w_D}{V} = \delta_{w,D}\frac{M_u}{M_T} = (-1.35)(-0.0093) = 0.0126$$

$$\frac{\Delta u_D}{V} = \delta_{u,D}\frac{M_u}{M_T} = (-0.29)(-0.0093) = 0.0027$$

From equation (46) of reference 7,

$$\frac{\Delta w}{V} = \frac{\Delta w_L}{V} + \frac{\Delta w_D}{V} = 0.0279 + 0.0126 = 0.0405$$

From equation (47) of reference 7,

$$\frac{\Delta u}{V} = \frac{\Delta u_L}{V} + \frac{\Delta u_D}{V} = 0 + 0.0027 = 0.0027$$

From equation (48b) of reference 7,

$$\Delta\alpha = \tan^{-1}\frac{\Delta w/V}{1 + \frac{\Delta u}{V}} = \tan^{-1}\frac{0.0405}{1.0027} = 2.31°$$

$$\alpha_c = -0.16 + 2.31 = 2.15°$$

$$\cos \Delta\alpha = 0.99919$$

$$L \cos \Delta\alpha = 33.4729; \quad D \cos \Delta\alpha = 14.7880$$

$$\sin \Delta\alpha = 0.04031$$

L sin $\Delta\alpha$ = 1.3504; D sin $\Delta\alpha$ = 0.5966

L_c = L cos $\Delta\alpha$ - D sin $\Delta\alpha$ = 32.8763

D_c = L sin $\Delta\alpha$ + D cos $\Delta\alpha$ = 14.7880

$$\frac{L_c}{T_o} = \frac{32.8763}{31.10} = 1.0571$$

$$\frac{D_c}{T_o} = \frac{16.1384}{31.10} = 0.5189$$

The pitching-moment parameter $\frac{M}{T_o \bar{c}}$ is not corrected for wall effects; however, it is plotted in this report against the corrected angle of attack α_c.

REFERENCES

1. Hickey, David H.; and Hall, Leo P.: Aerodynamic Characteristics of a Large-Scale Model With Two High Disk-Loading Fans Mounted in the Wing. NASA TN D-1650, 1963.

2. Goldsmith, Robert H.; and Hickey, David H.: Characteristics of Lifting-Fan V/STOL Aircraft. Astronaut. Aerospace Eng., vol. 1, no. 9, Oct. 1963, pp. 70-77.

3. Spreemann, Kenneth P.: Induced Interference Effects on Jet and Buried-Fan VTOL Configurations in Transition. NASA TN D-731, 1961.

4. Vogler, Raymond D.: Surface Pressure Distributions Induced on a Flat Plate by a Cold Air Jet Issuing Perpendicularly From the Plate and Normal to a Low-Speed Free-Stream Flow. NASA TN D-1629, 1963.

5. Aoyagi, Kiyoshi; Hickey, David H.; and deSavigny, Richard A.: Aerodynamic Characteristics of a Large-Scale Model With a High Disk-Loading Lifting Fan Mounted in the Fuselage. NASA TN D-775, 1961.

6. Staff of Powered-Lift Aerodynamics Section, NASA Langley Research Center: Wall Effects and Scale Effects in V/STOL Model Testing. AIAA Aerodynamic Testing Conference (Washington, D.C.), Mar. 1964.

7. Heyson, Harry H.: Linearized Theory of Wind-Tunnel Jet-Boundary Corrections and Ground Effect for VTOL-STOL Aircraft. NASA TR R-124, 1962.

8. Theodorsen, Th.: Theoretical Investigation of Ducted Propeller Aerodynamics - Vol. I. Contract No. DA 44-177-TC-606, Rep. Aviation Corp., Aug. 10, 1960.

9. Jordinson, R.: Flow in a Jet Directed Normal to the Wind. R. & M. No. 3074, British A.R.C., 1958.

10. Hoerner, Sighard F.: Fluid-Dynamic Drag. Publ. by the author (148 Busteed Drive, Midland Park, N.J.), 1958.

11. Trebble, W. J. G.; and Hackett, J. E.: Low-Speed Wind-Tunnel Tests on a Streamlined Body Containing a Ducted Lifting Fan. Tech. Note No. Aero 2893, British R.A.E., May 1963.
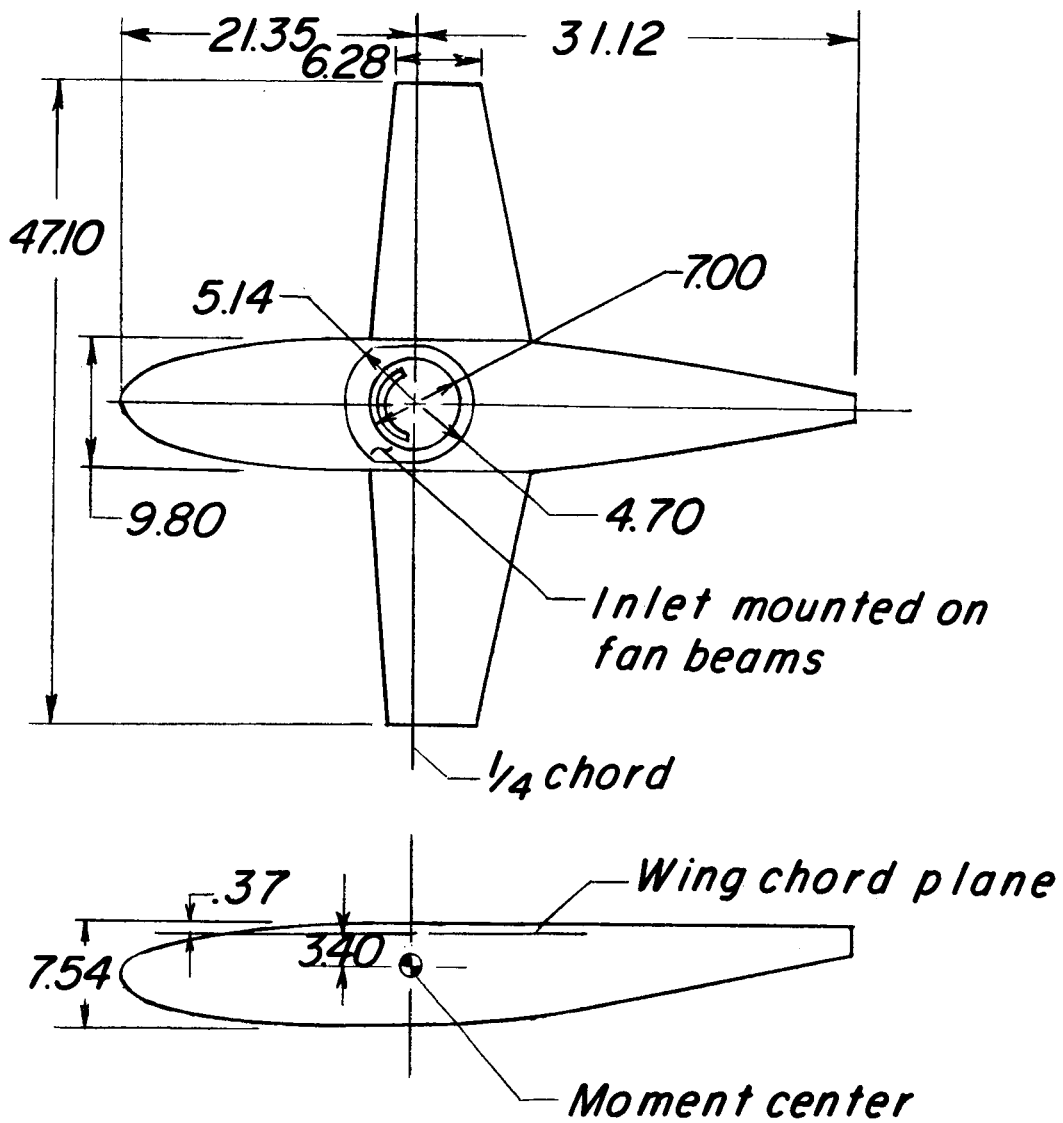
Figure 1.- Drawing of model. All dimensions are in inches.
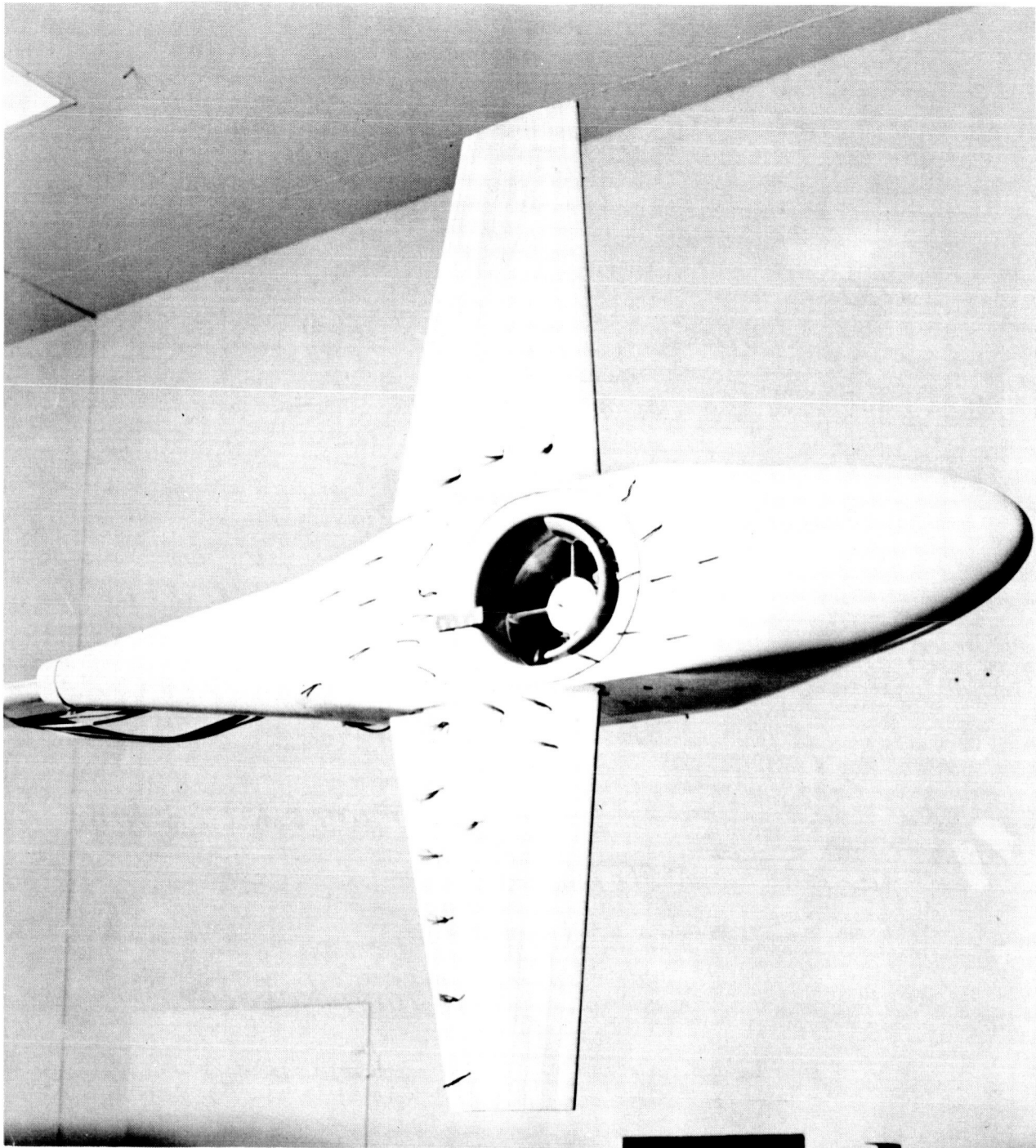
Figure 2.- Photograph of model mounted in 17-foot test section.   L-62-2997

Forward

.164 radius

Sponge seal

Inlet vane

Sponge seal

.42 radius

Air jet

3/8

3/4

3/32

Detail A

Fuselage lower surface
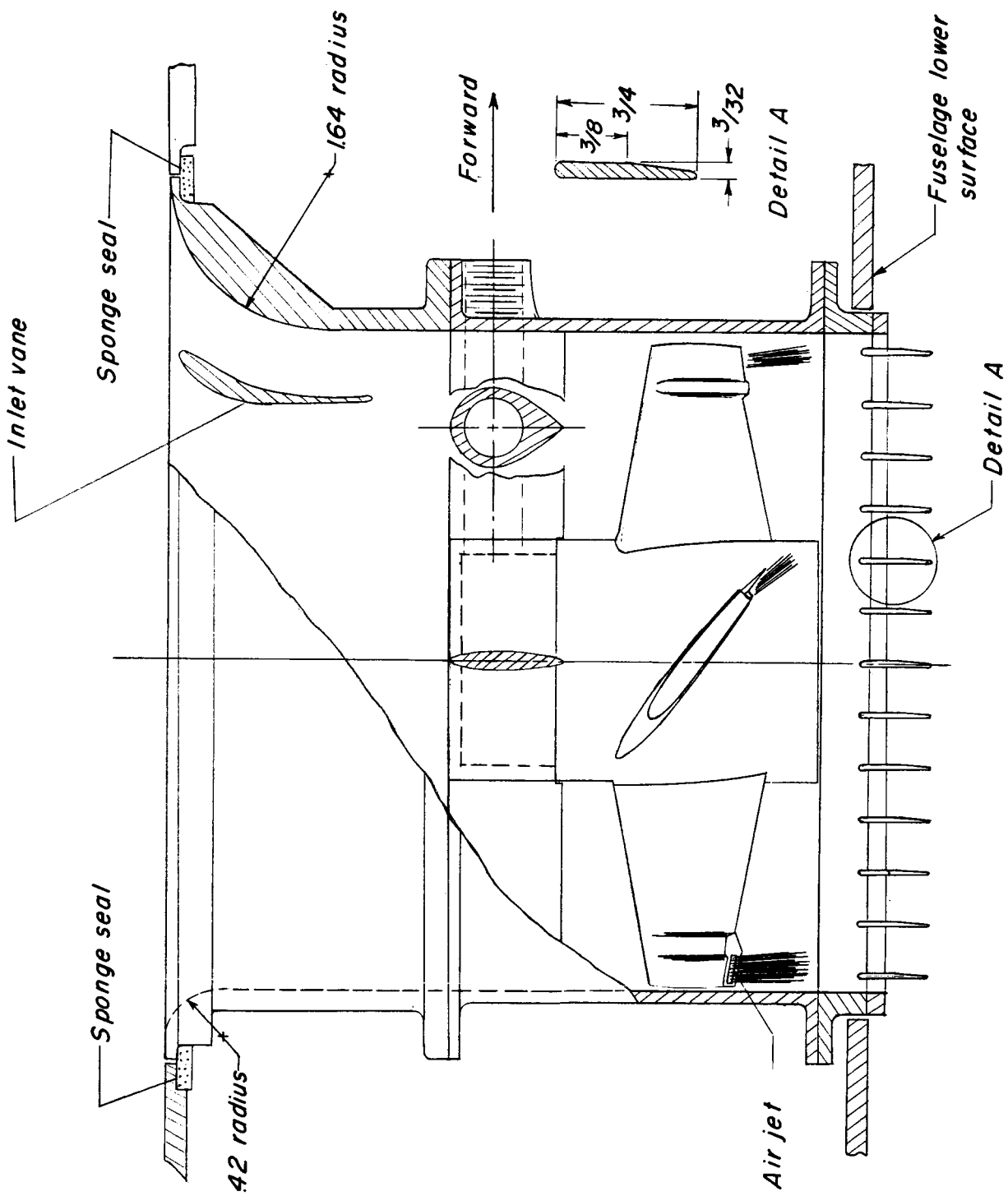
Detail A

Figure 3.- Fan details. All dimensions are in inches.
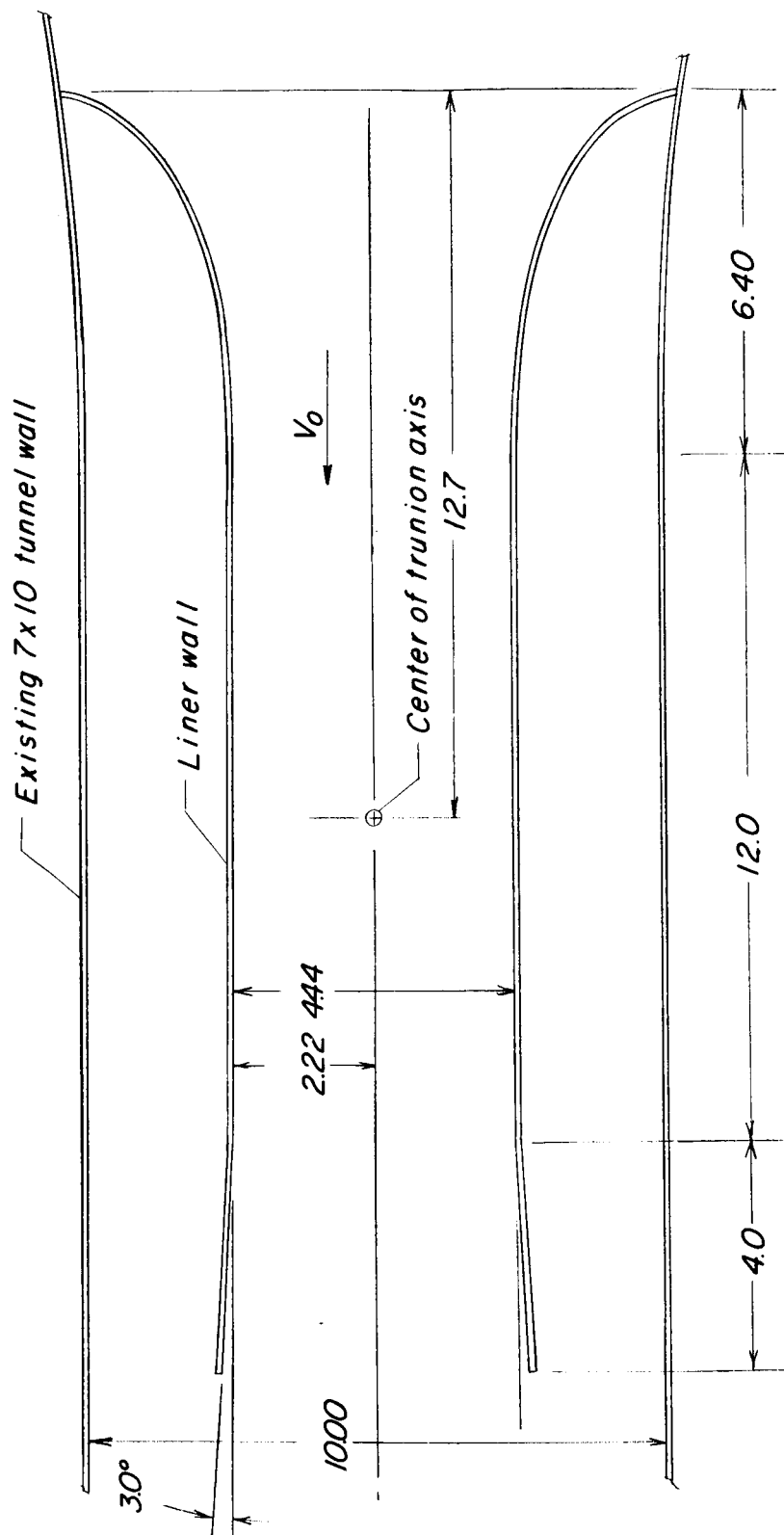
Figure 4.- Simulated Ames 40- by 80-foot tunnel in Langley 300-MPH 7- by 10-foot tunnel (referred to as 4.4- by 7.0-foot test section). (All dimensions are in feet.)
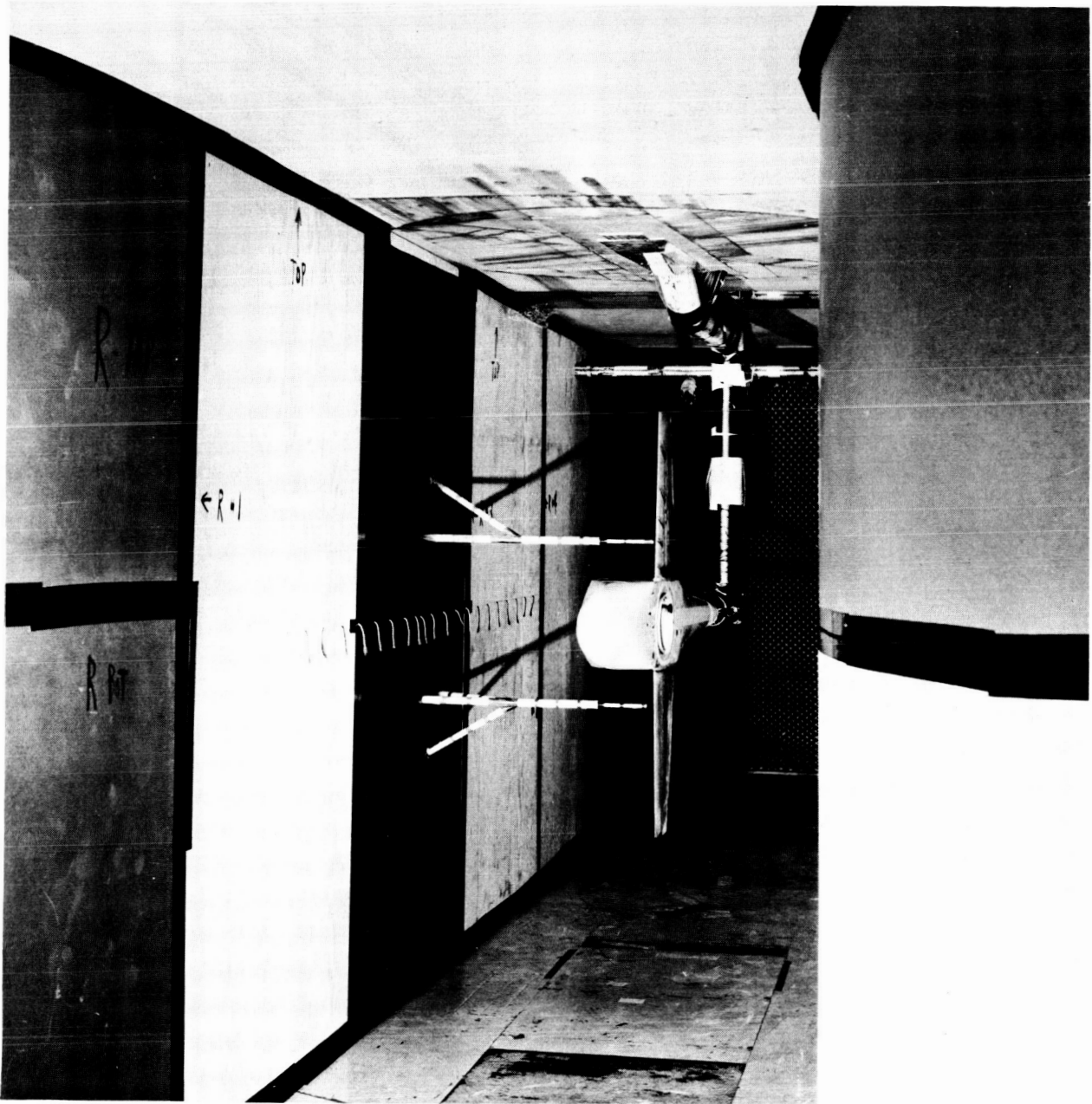
Figure 5.- Model installed in the 4.4- by 7.0-foot test section.   L-63-9103
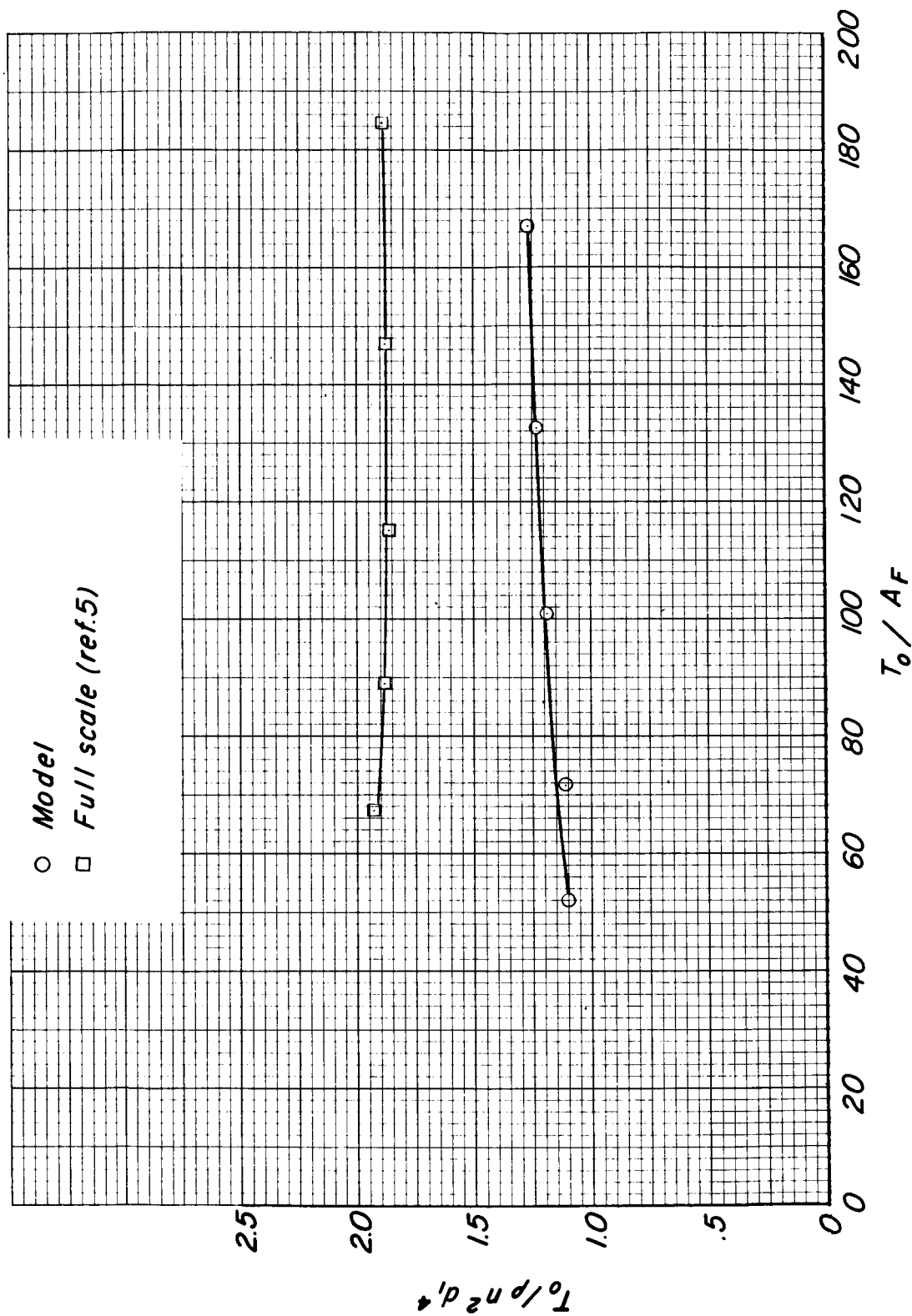
Figure 6.- Comparison of model and full-scale thrust coefficients for disk loadings investigated.

26
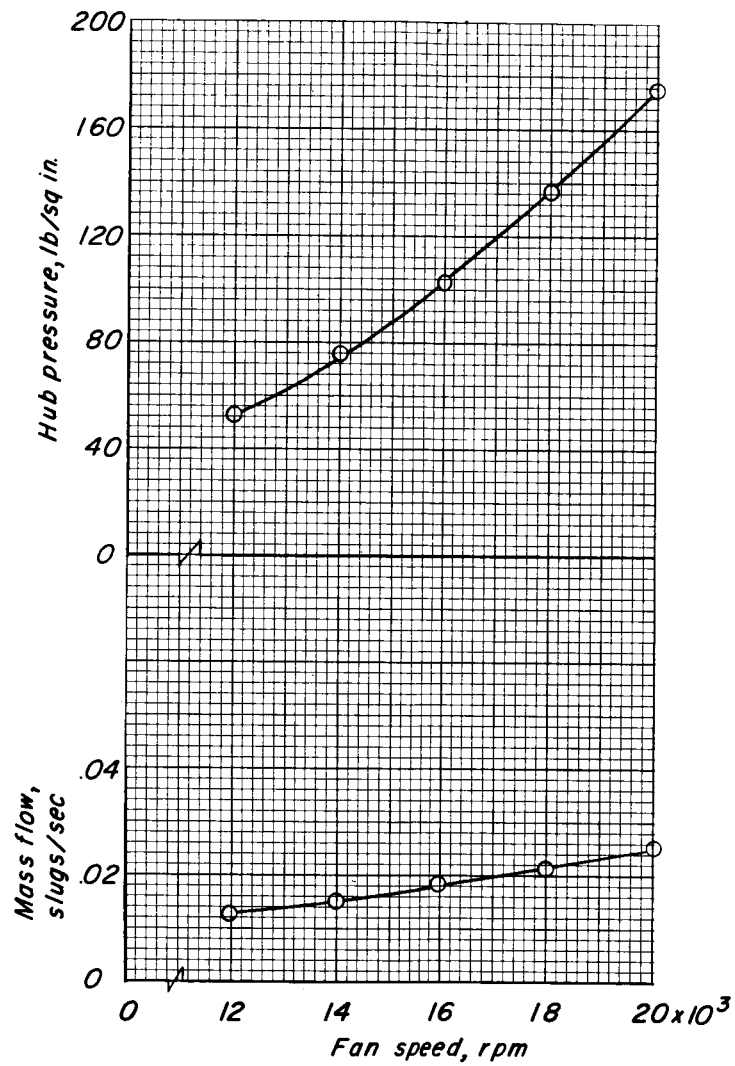
(a) Effect of fan speed at $V_\infty = 0$.

Figure 7.- Mass flow and hub pressure required to drive the model fan.
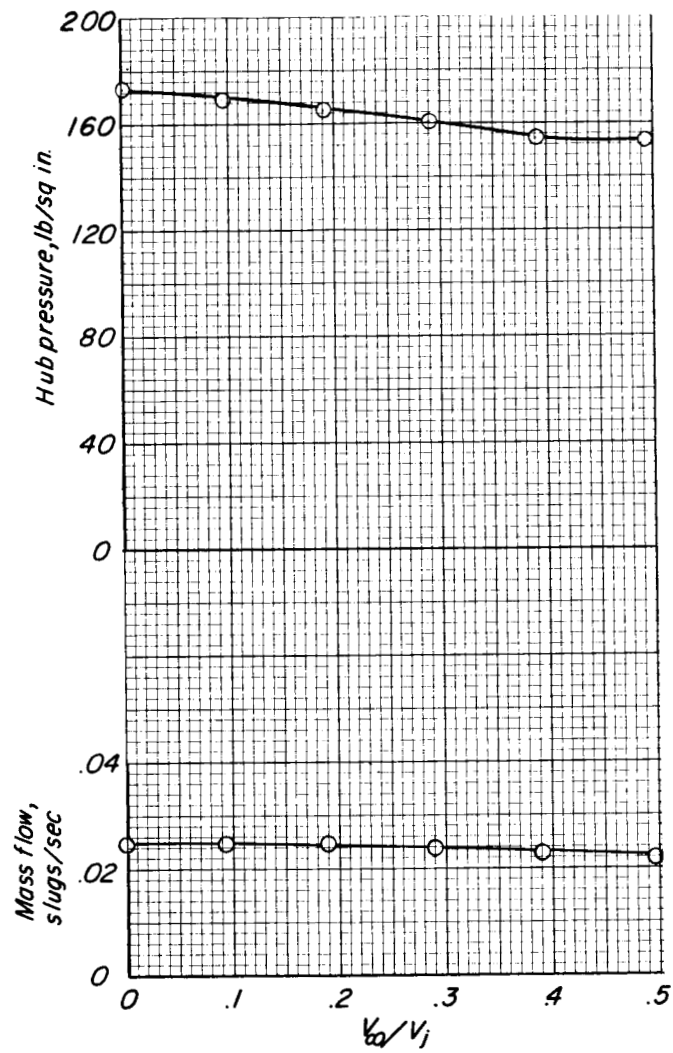
(b) Effect of forward speed; N = 20,000 rpm.

Figure 7.- Concluded.
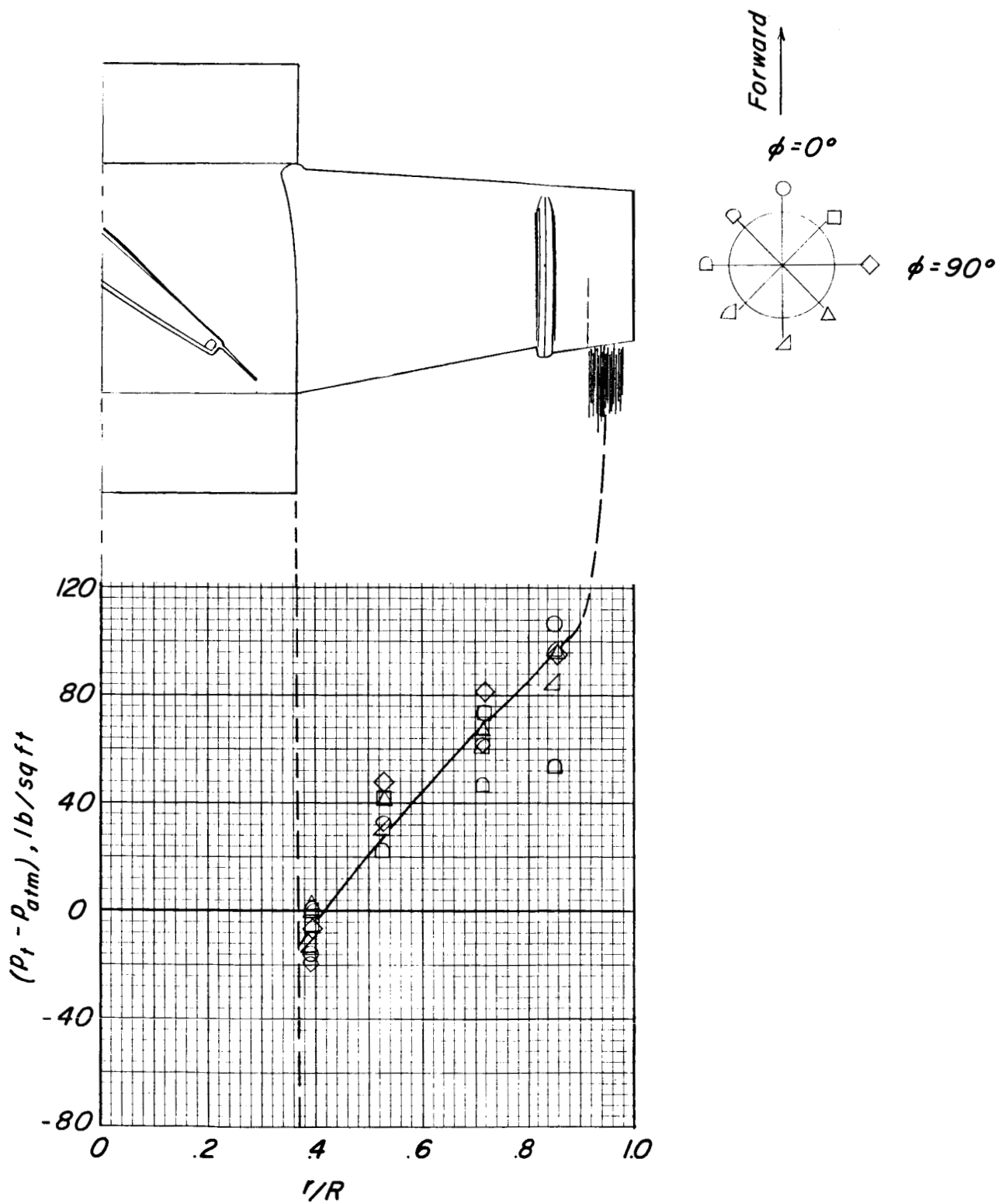
Figure 8.- Distribution of pressure at model fan exit. $V_\infty/V_j = 0$; $\alpha = 0^\circ$; $N = 20,000$ rpm.
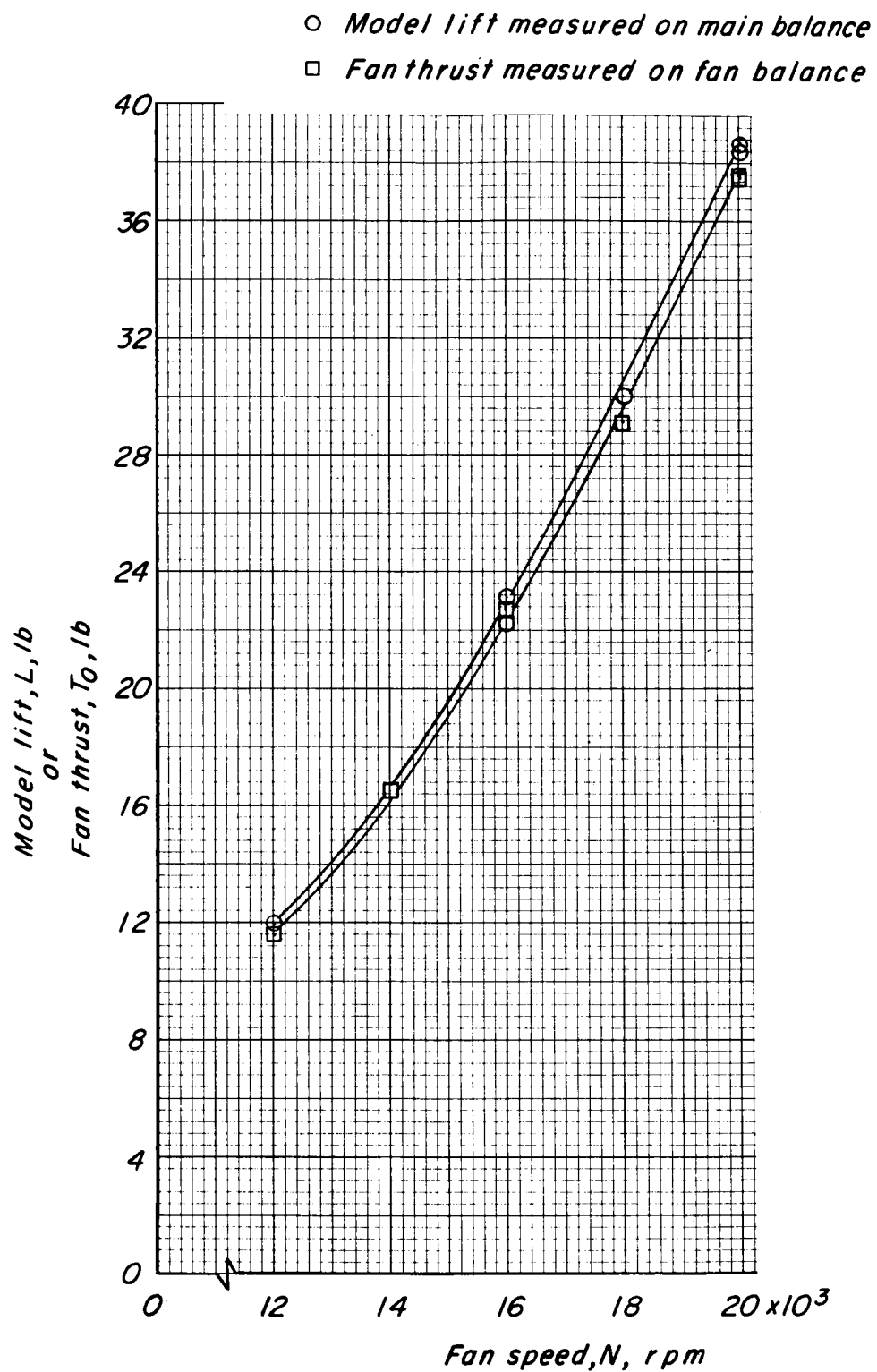
Figure 9.- Comparison of model lift and model fan static thrust; $\alpha = 0°$.

○   *T₀ measured on fan balance*

□   *Fan-exit momentum from exit rake survey
(Does not include tip-jet momentum)*

◇   *Total fan exit momentum from pressure
surveys including tip-jet momentum*
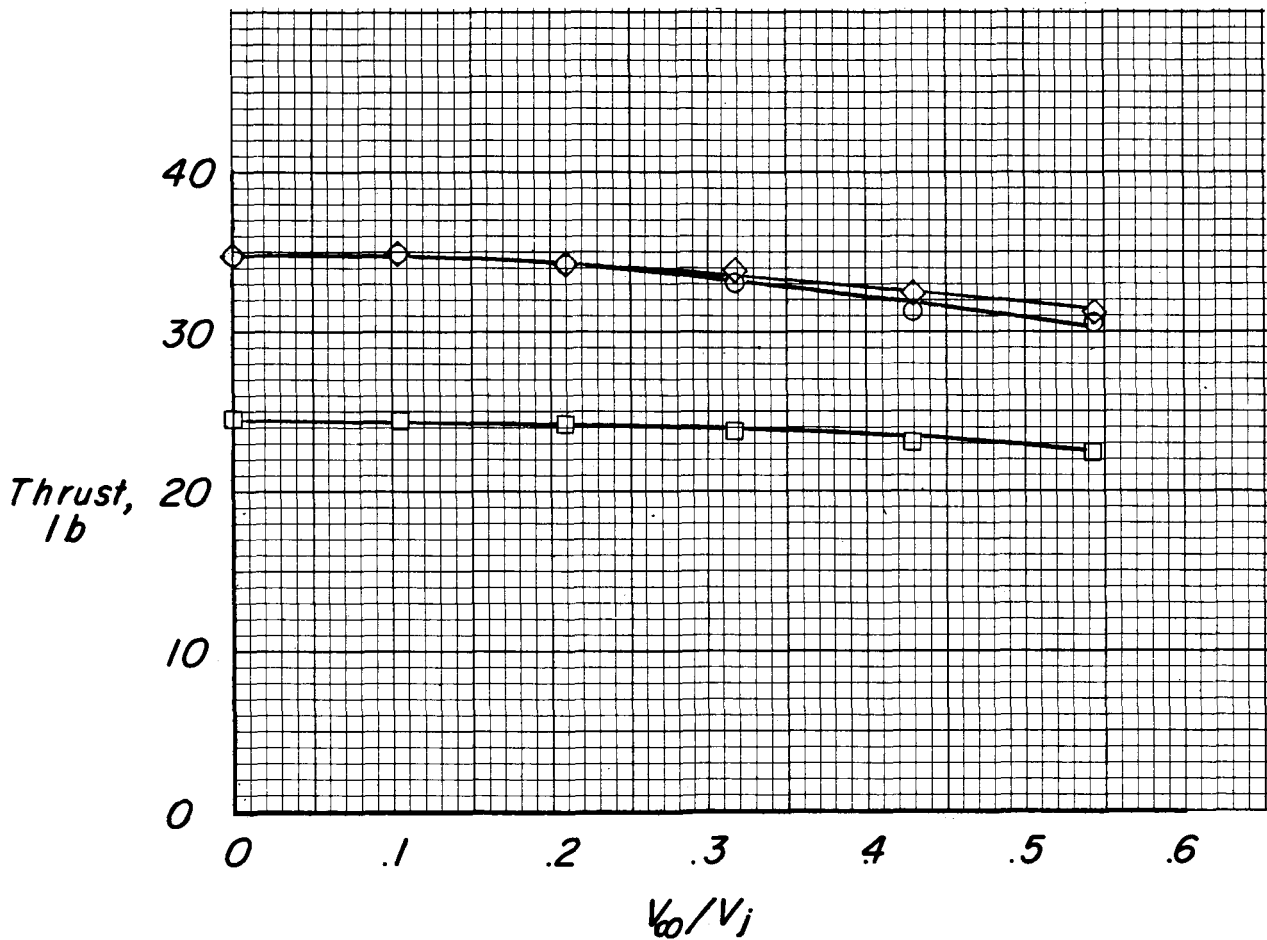
Figure 10.- Variation of fan thrust with forward speed determined by two methods.
$N = 20,000$ rpm; $\alpha = 0°$.
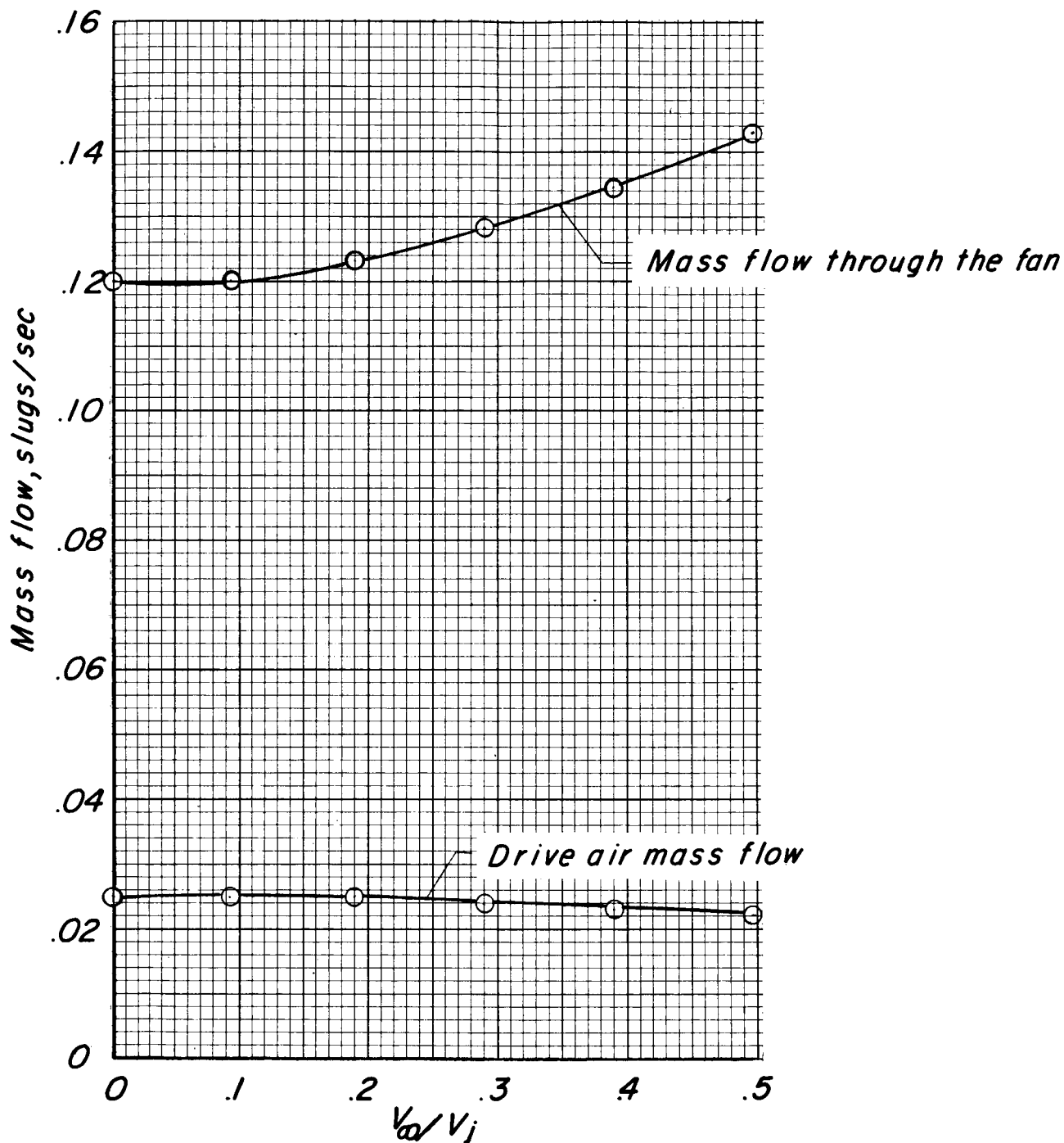
Figure 11.- Comparison of mass flow required to drive the model fan with the inlet mass flow.   N = 20,000 rpm; $\alpha = 0^{\circ}$.

$\frac{M}{T_0 \bar{c}}$

$\frac{D}{T_0}$

$\frac{L}{T_0}$

1.5
1.0
.5
0

1.5
1.0
.5
0
-.5
-1.0

2.5
2.0
1.5
1.0
.5
0

	V_∞ / V_j	T_0, lb
○	.05	11.9
□	.09	11.9
◇	.18	11.4
△	.28	11.4
◁	.38	11.0
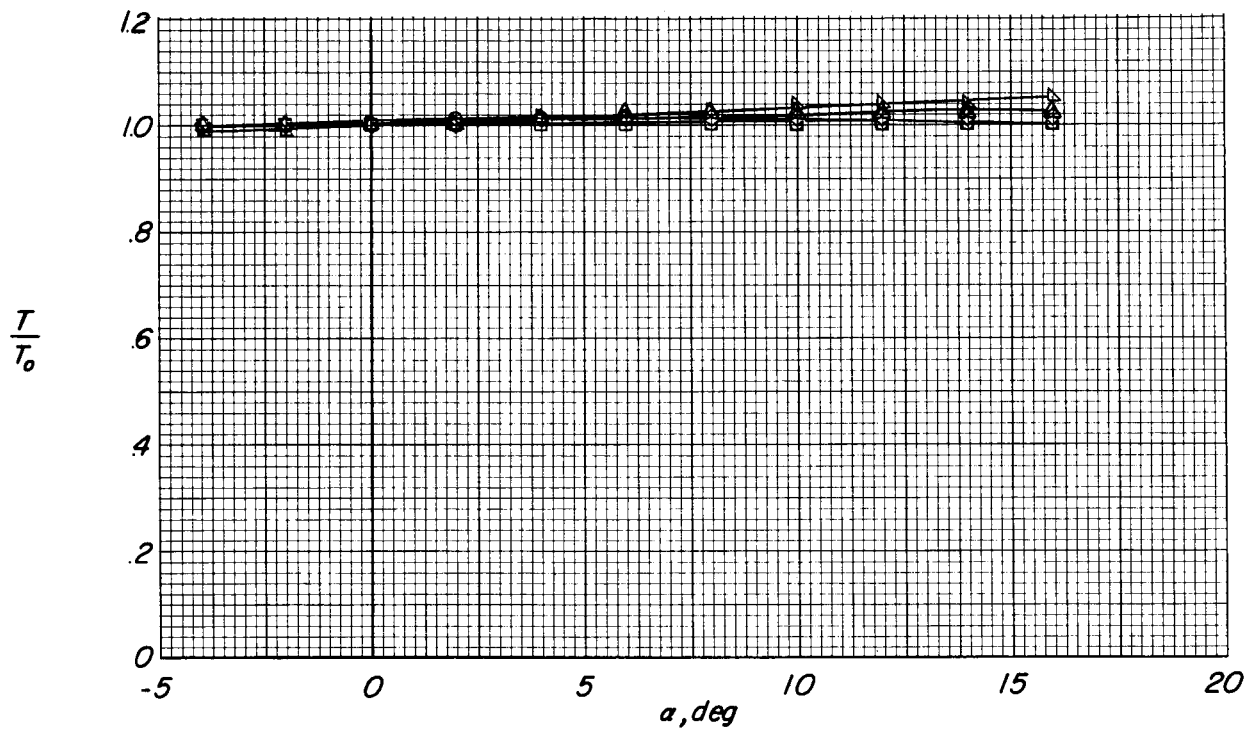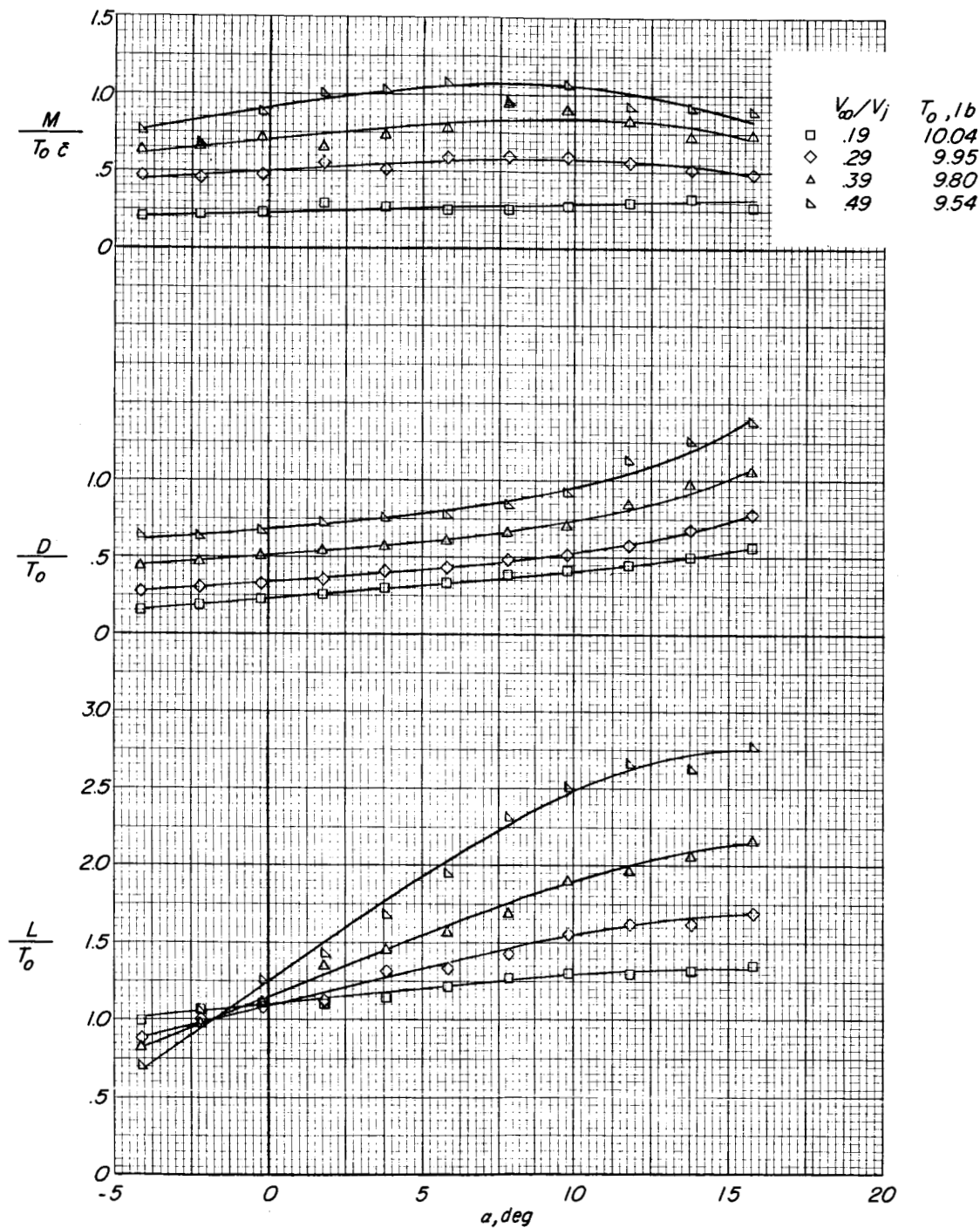
α, deg

-5   0   5   10   15   20

(a) Complete model forces and moment; 17-foot test section.

Figure 12.- Effect of angle of attack and forward speed on the aerodynamic characteristics of the model. N = 12,000 rpm; $\delta_v = 0^\circ$.

(b) Fan thrust; 17-foot test section.

Figure 12.- Continued.

$\dfrac{M}{T_0 \bar{c}}$

	V_∞/V_j	T_0 , lb
□	.19	10.04
◇	.29	9.95
△	.39	9.80
◿	.49	9.54

$\dfrac{D}{T_0}$

$\dfrac{L}{T_0}$

a, deg

(c) Complete model forces and moment; 4.4- by 7.0-foot test section.

Figure 12.- Continued.
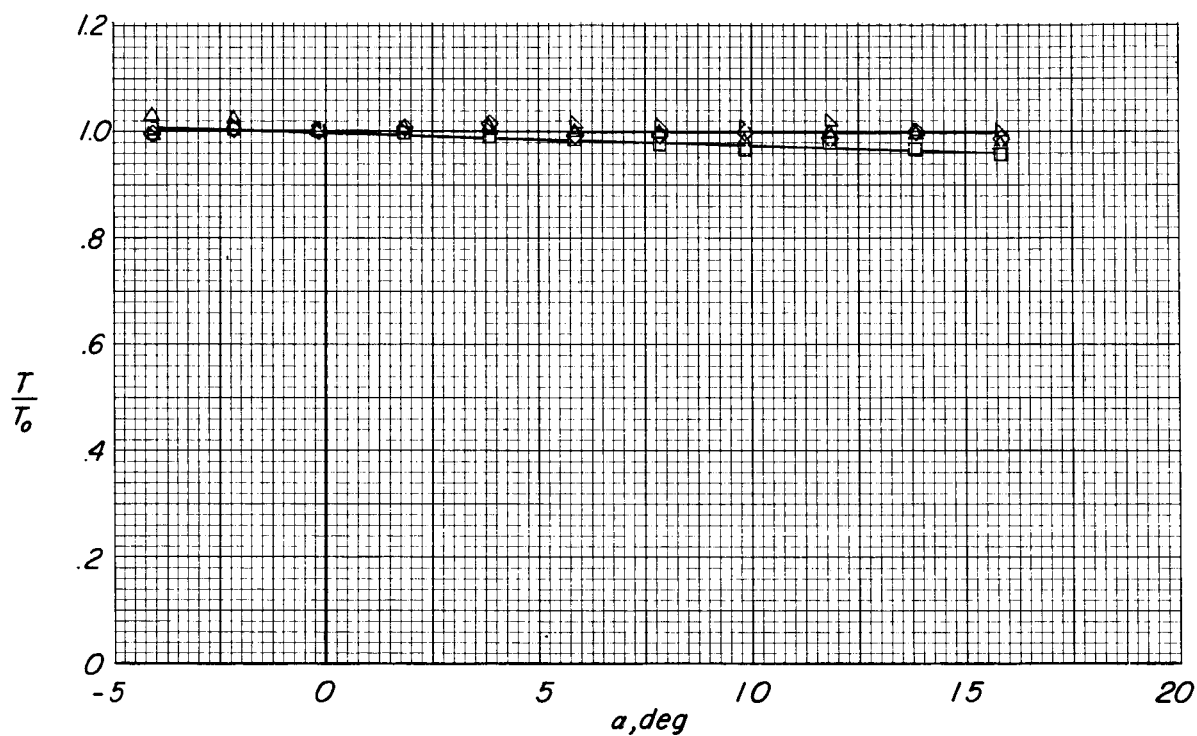
(d) Fan thrust; 4.4- by 7.0-foot test section.

Figure 12.- Concluded.

	V_∞/V_j	T_0, lb
○	.05	22.2
□	.09	22.2
◇	.19	21.5
△	.28	20.9
◮	.38	20.3
◰	.48	19.9
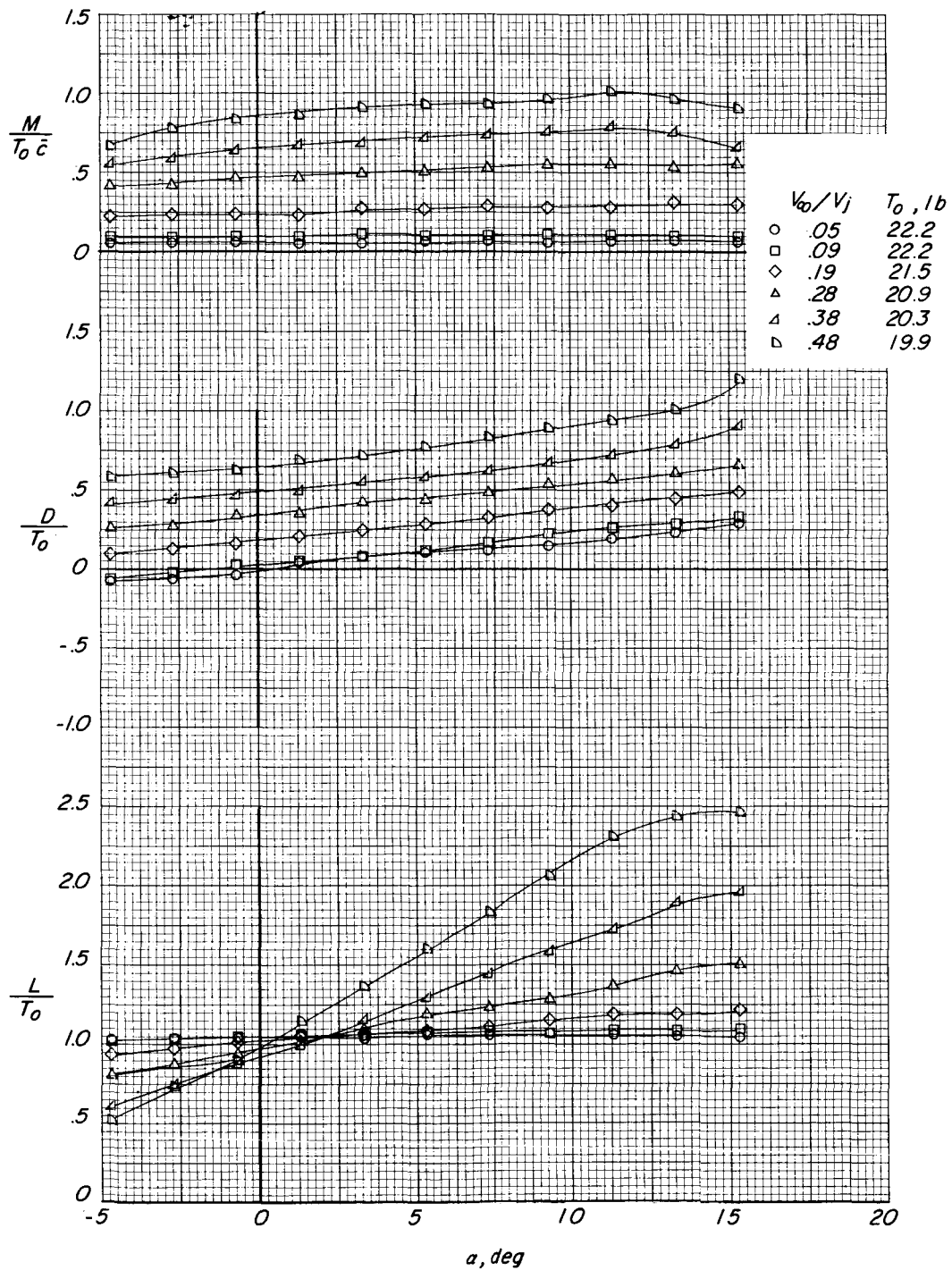
(a) Complete model forces and moment; 17-foot test section.

Figure 13.- Effect of angle of attack and forward speed on the aerodynamic characteristics of the model. N = 16,000 rpm; $\delta_v = 0°$.

	V_∞/V_j	T_0 , lb
○	.05	22.2
□	.09	22.2
◇	.19	21.5
△	.28	20.9
◁	.38	20.3
▷	.48	19.9
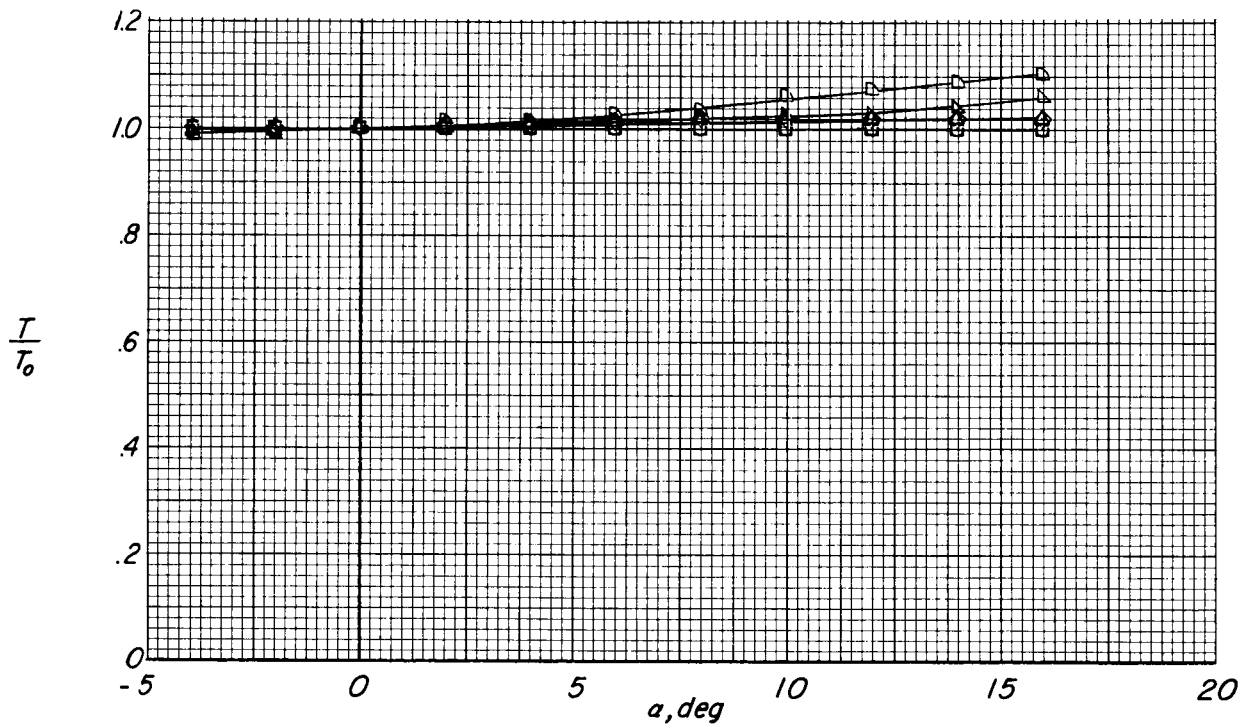
(b) Fan thrust; 17-foot test section.

Figure 13.- Continued.
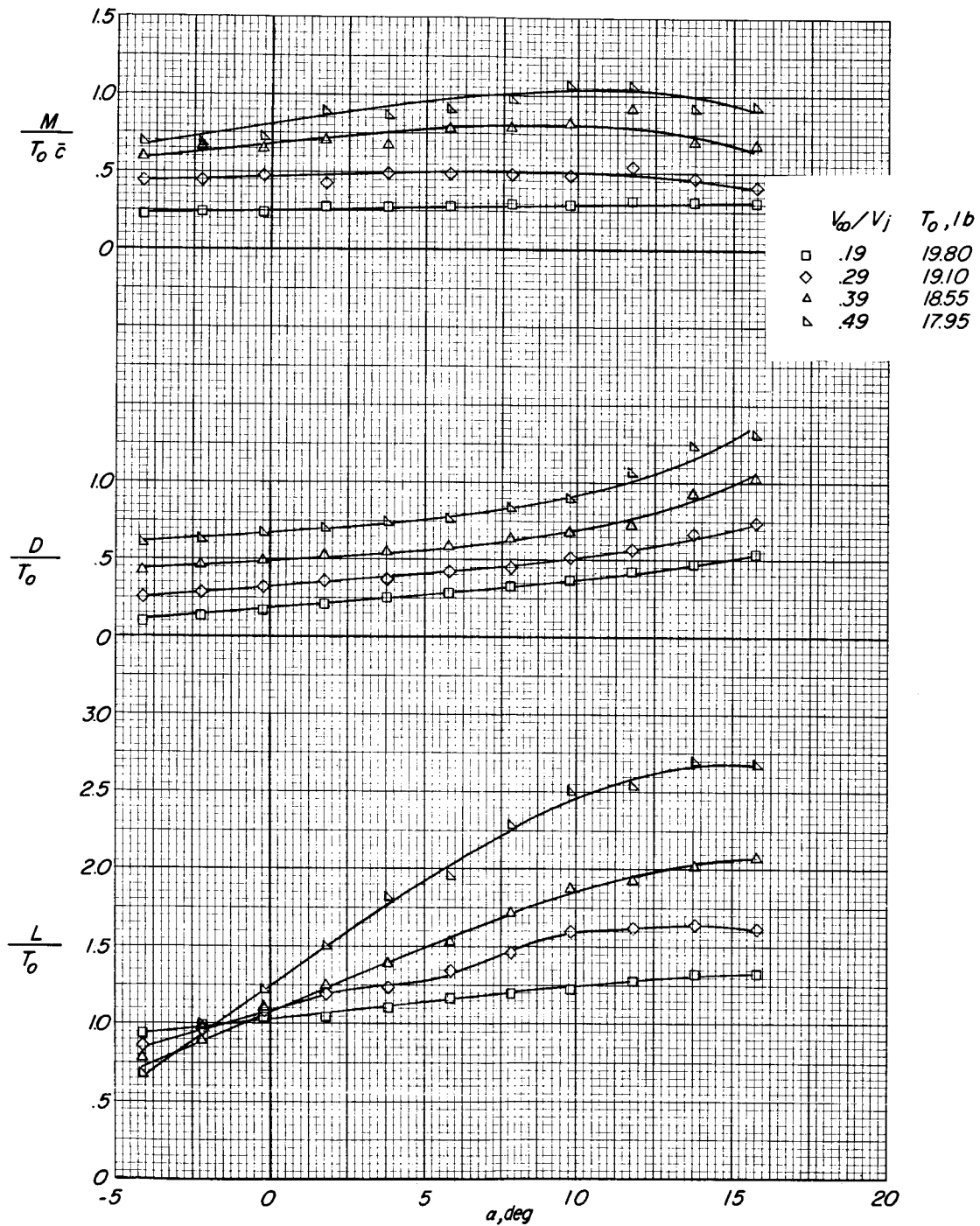
(c) Complete model forces and moment; 4.4- by 7.0-foot test section.

Figure 13.- Continued.

	V_∞ / V_j	T_0, lb
○	.19	19.80
◇	.29	19.10
△	.39	18.55
◁	.49	17.95
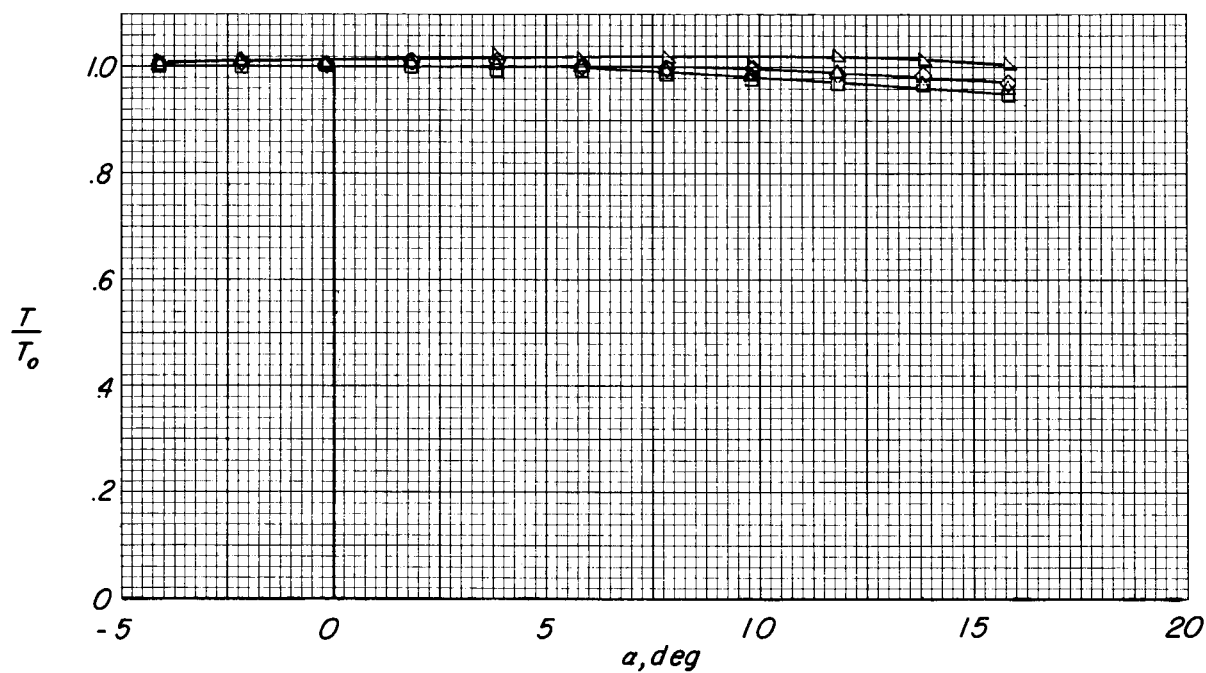
(d) Fan thrust; 4.4- by 7.0-foot test section.

Figure 13.- Concluded.
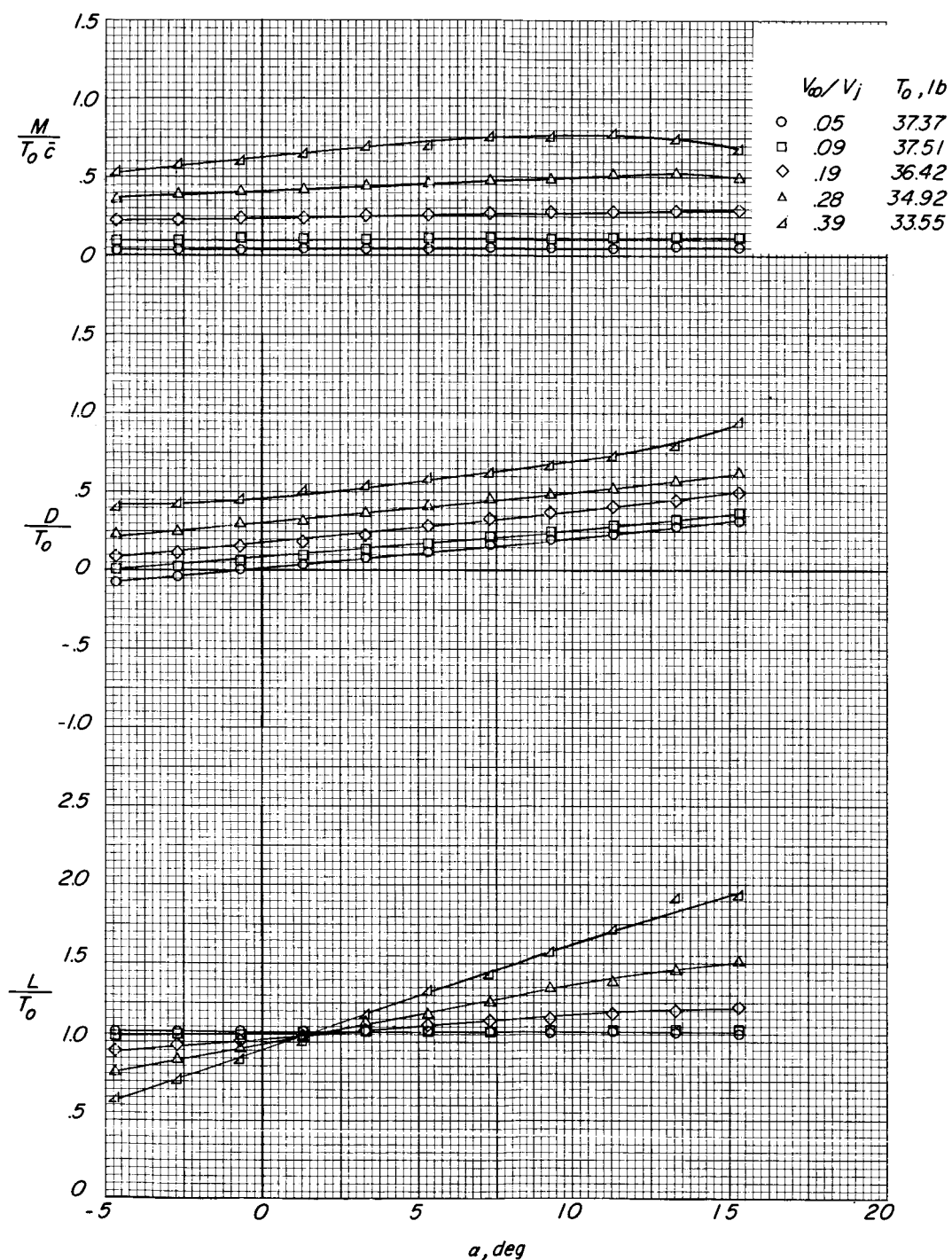
(a) Complete model forces and moment; 17-foot test section.

Figure 14.- Effect of angle of attack and forward speed on the aerodynamic characteristics of the model. $N = 20,000$ rpm; $\delta_V = 0°$.

	V_∞ / V_j	T_0, lb
○	.05	37.37
□	.09	37.51
◇	.19	36.42
△	.28	34.92
◿	.39	33.55
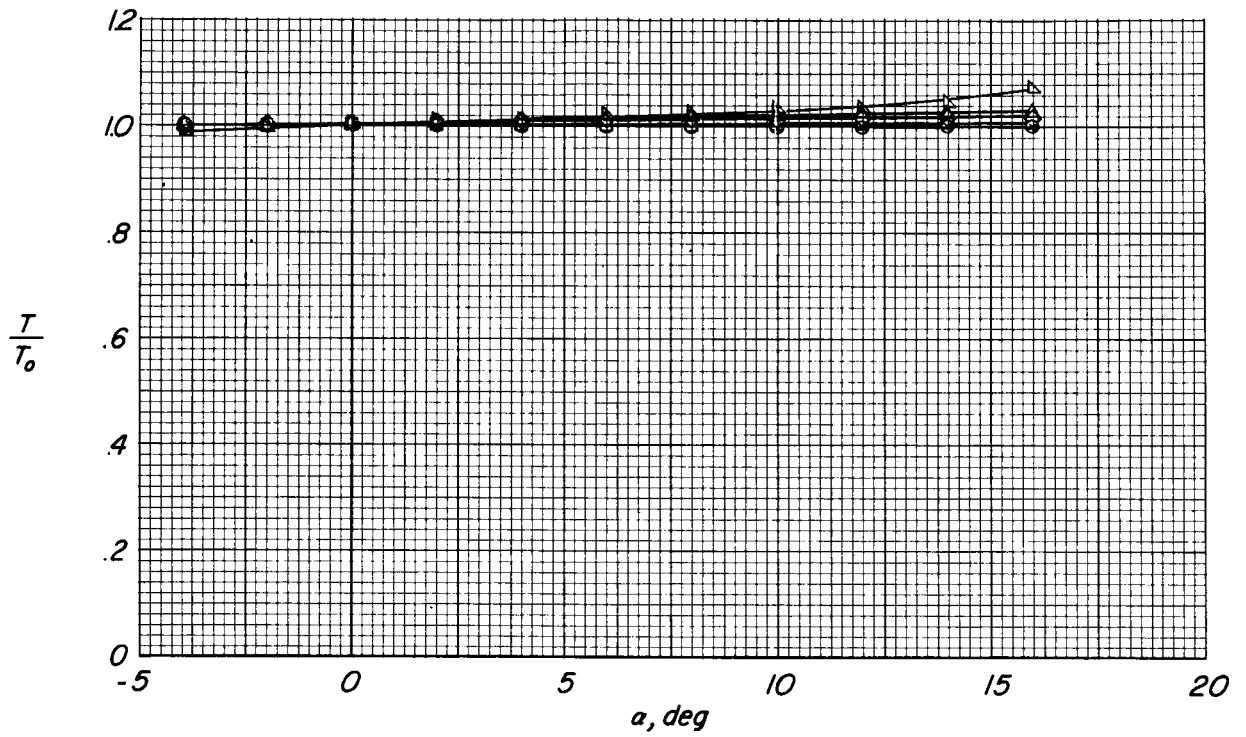
(b) Fan thrust; 17-foot test section.

Figure 14.- Continued.
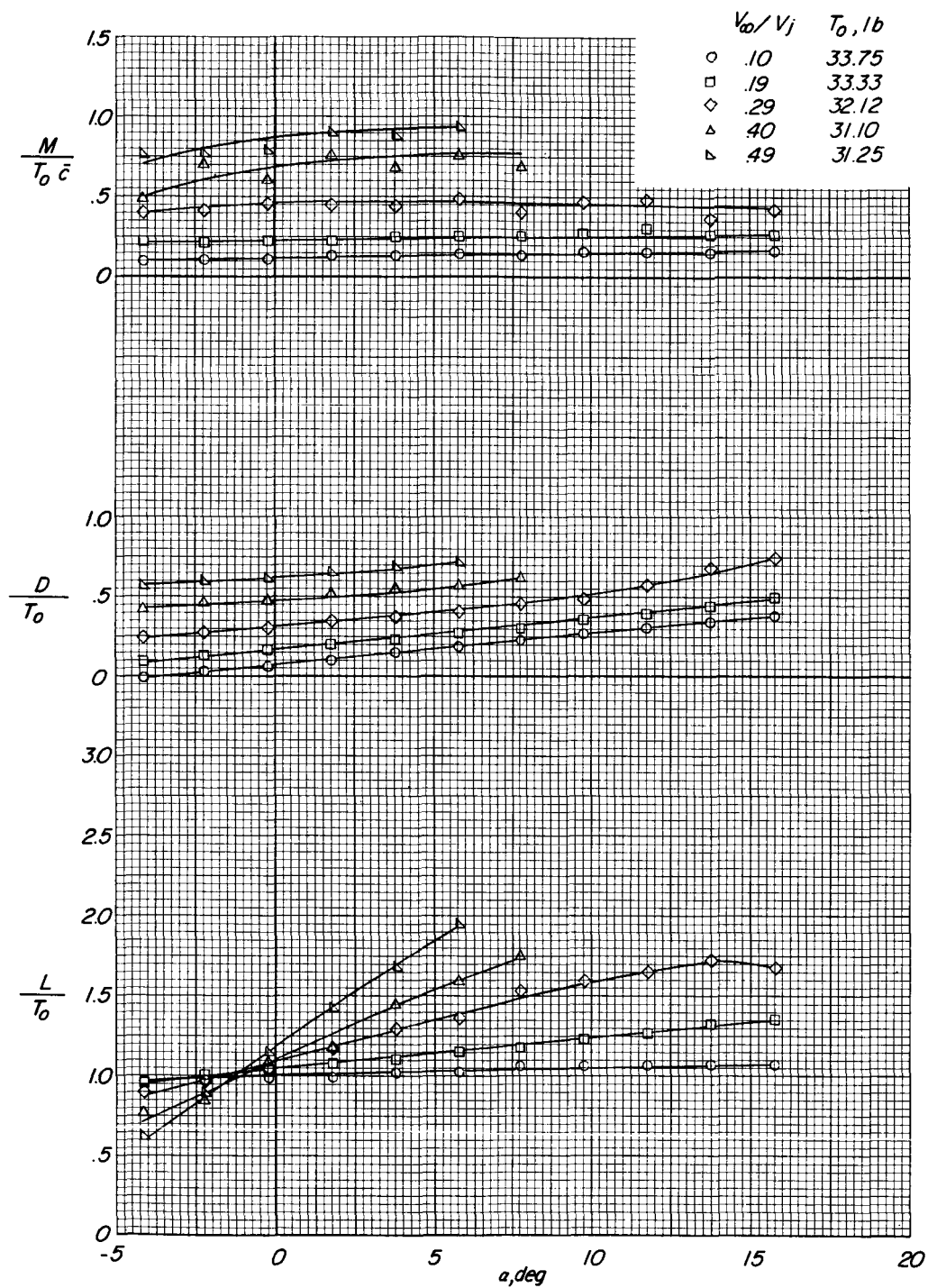
(c) Complete model forces and moment; 4.4- by 7.0-foot test section.

Figure 14.- Continued.

	V_∞/V_j	T_o , lb
○	.10	33.75
□	.19	33.33
◇	.29	32.12
△	.40	31.10
◭	.49	31.25
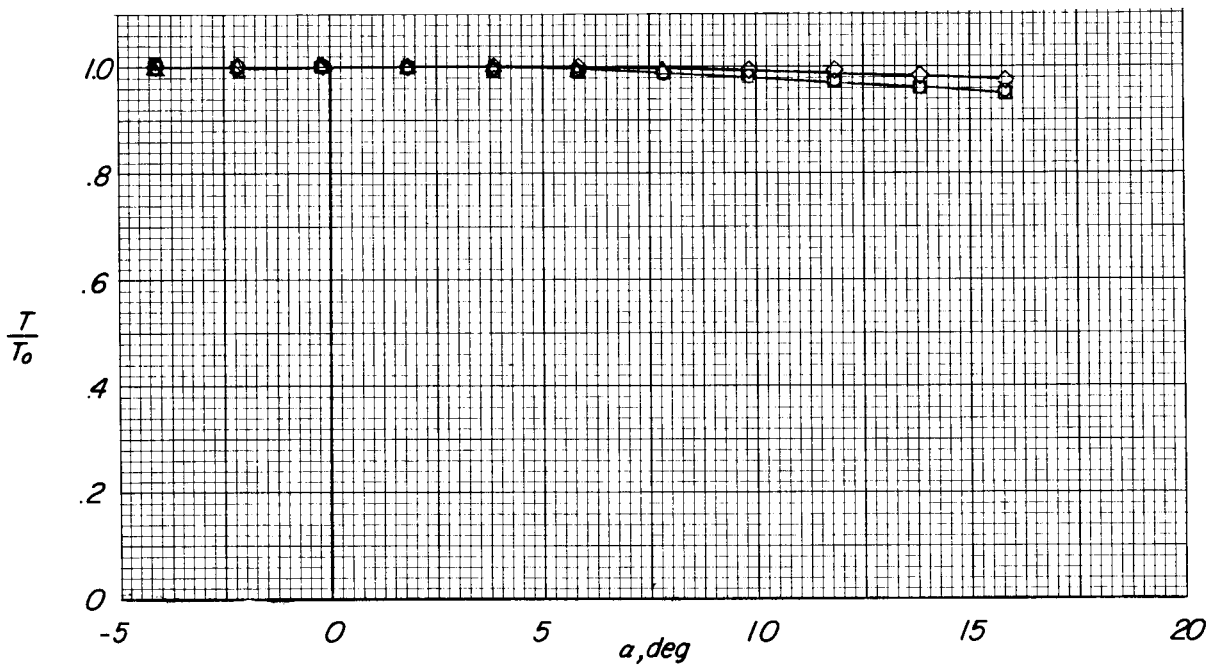
(d) Fan thrust; 4.4- by 7.0-foot test section.

Figure 14.- Concluded.
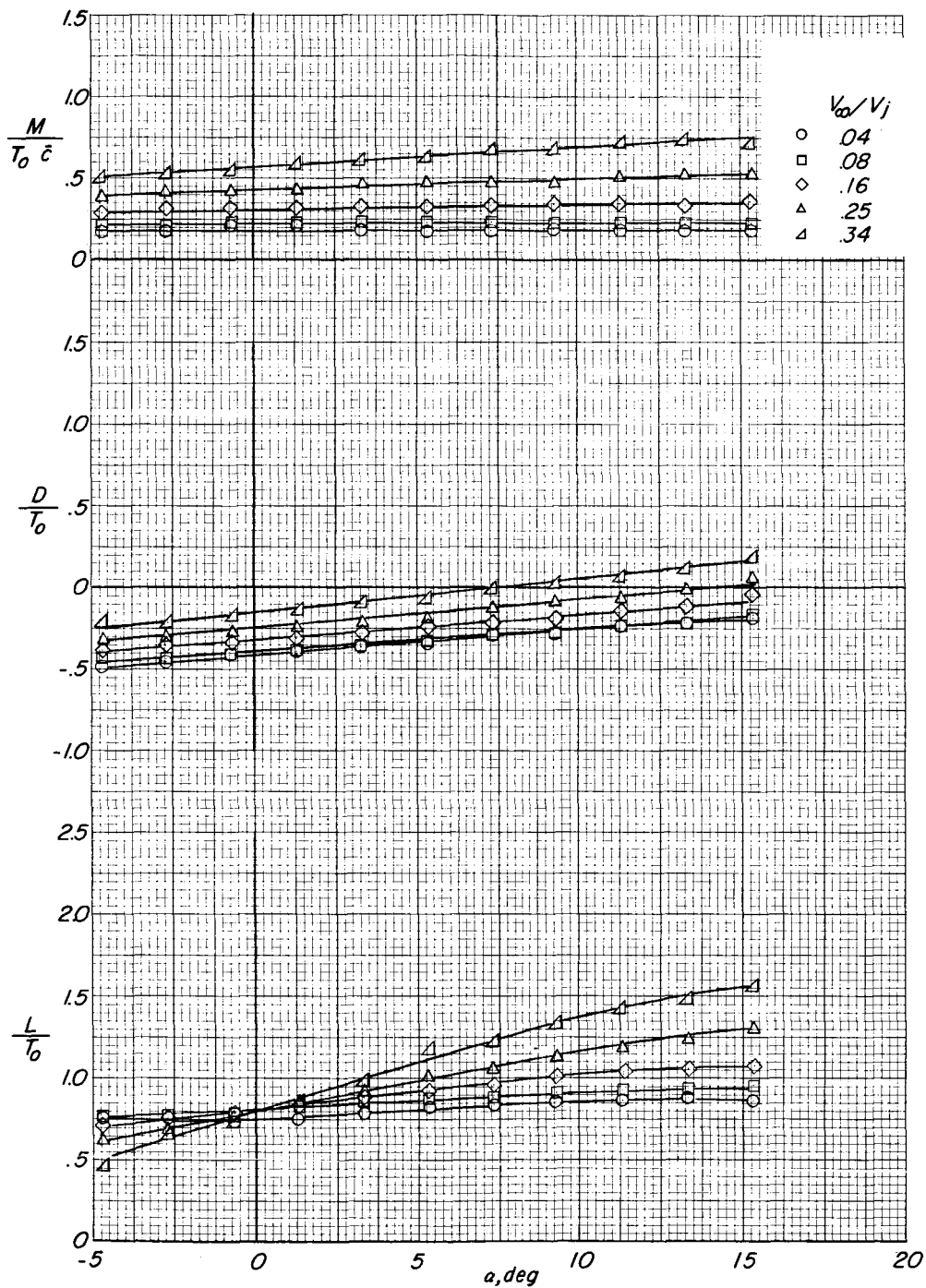
(a) Complete model forces and moment.

Figure 15.- Effect of forward speed and angle of attack on the aerodynamic characteristics of the model. $\delta_v = 30°$; N = 20,000 rpm; 17-foot test section.

	V_∞/V_j	T_o , lb
○	.04	37.37
□	.08	37.51
◇	.16	36.42
△	.25	34.92
◁	.34	33.55
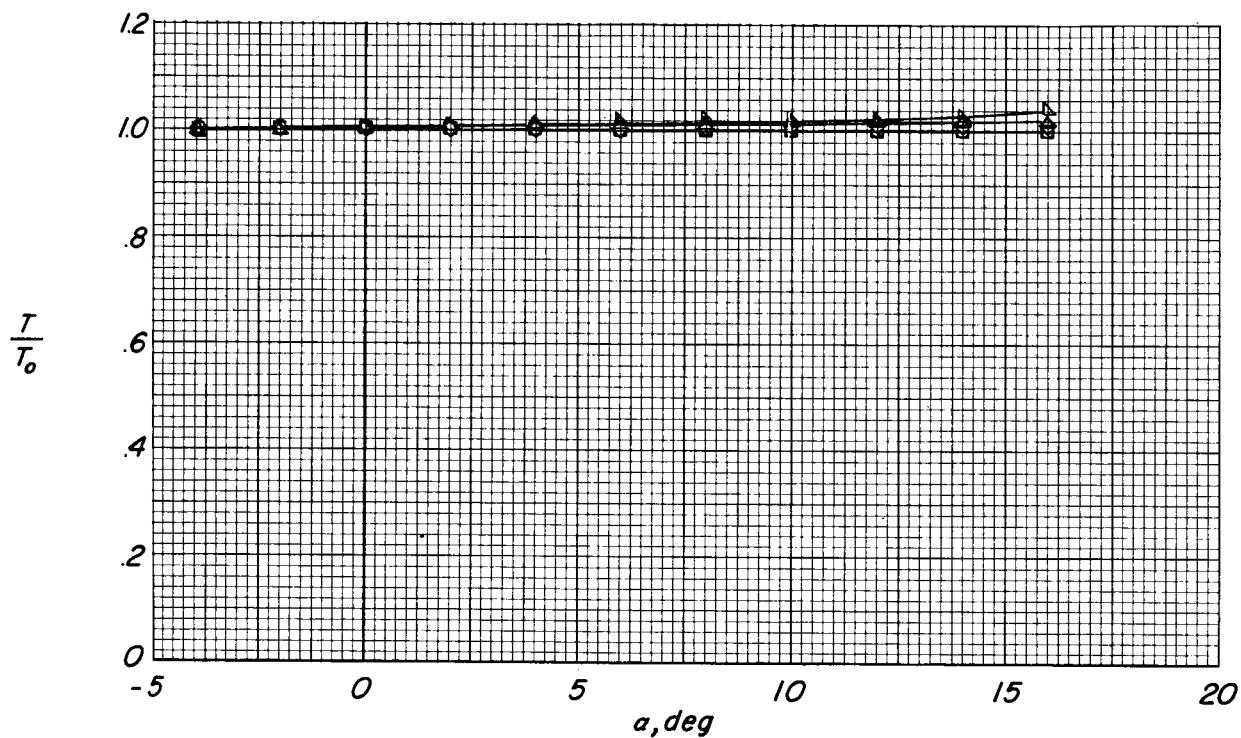
(b) Fan thrust.

Figure 15.- Concluded.
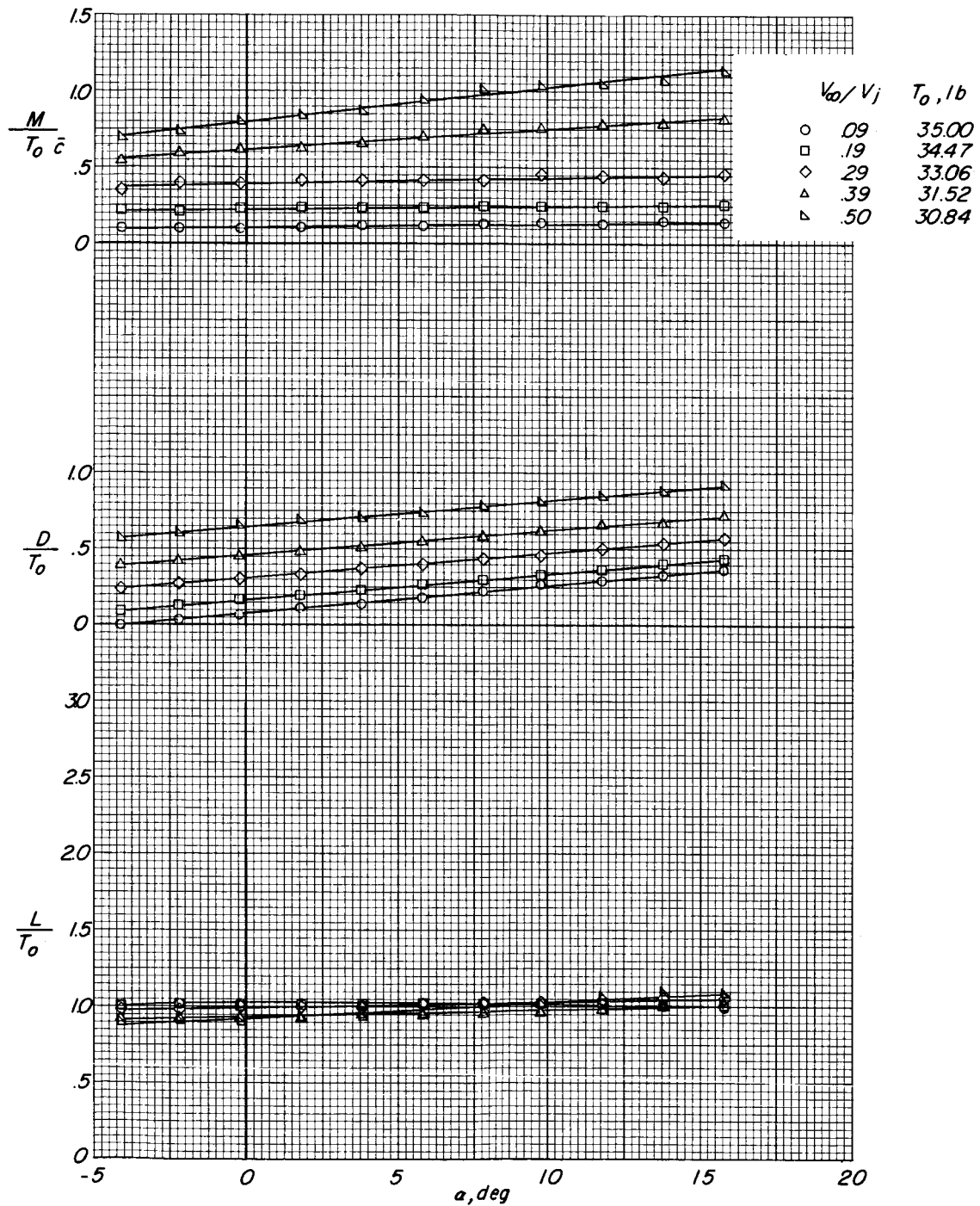
(a) Complete model forces and moment.

Figure 16.- Wing-off data. N = 20,000 rpm; δ_v = 0°; 4.4- by 7.0-foot test section.
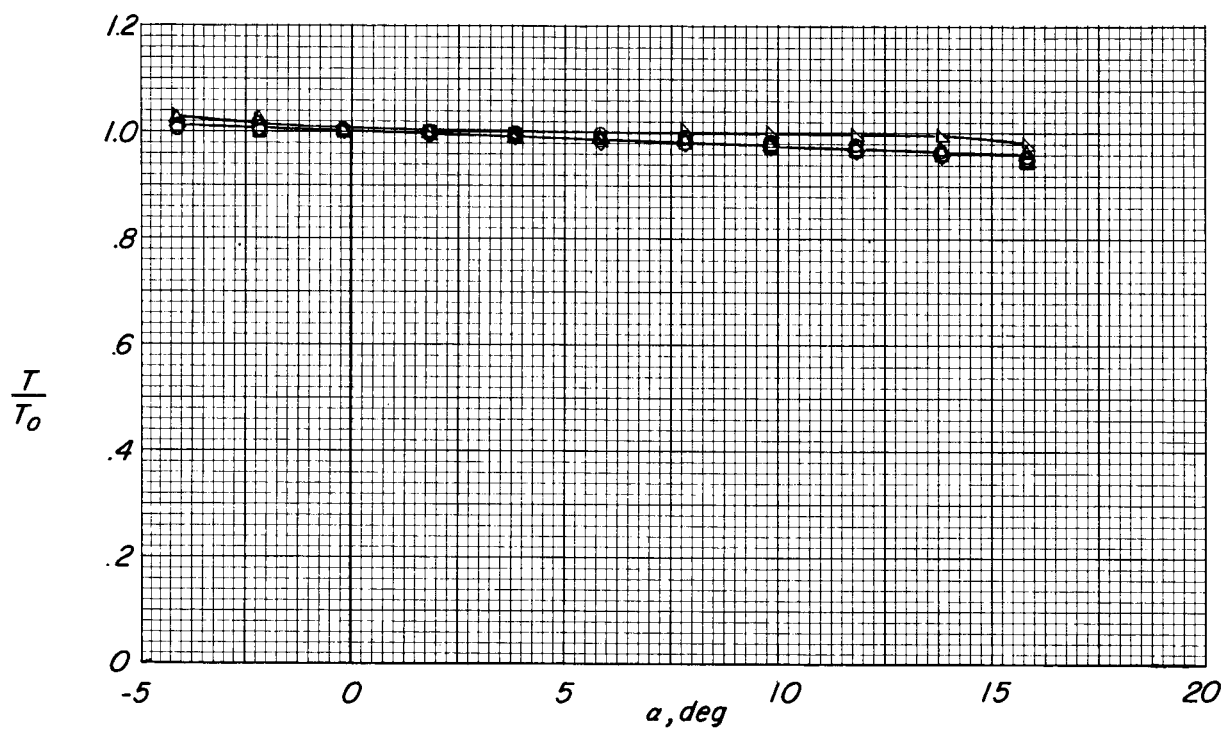
(b) Fan thrust.

Figure 16.- Concluded.

$\dfrac{M}{T_o \bar{c}}$

$\dfrac{D}{T_o}$

$\dfrac{L}{T_o}$

V_∞ / V_j
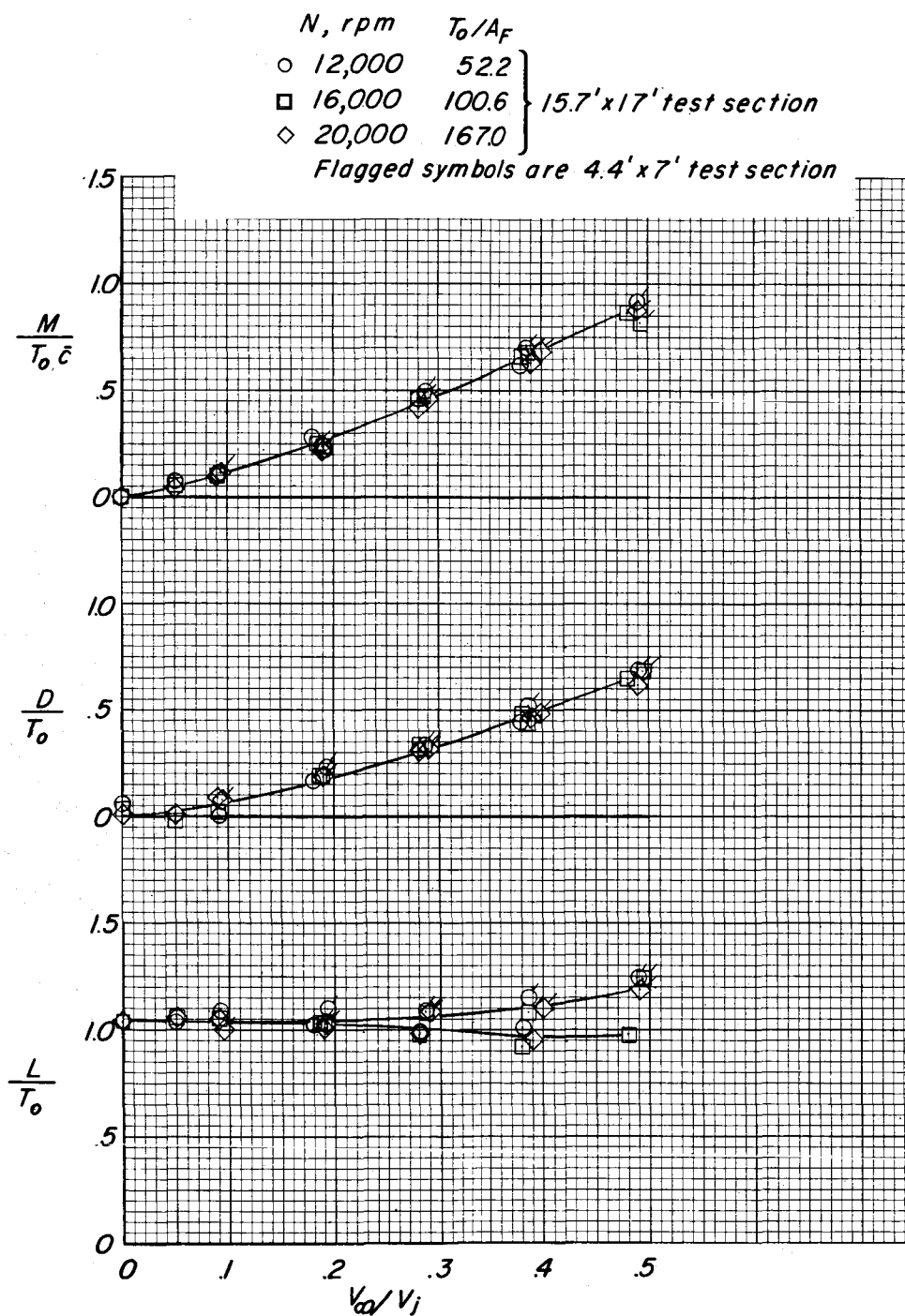
Figure 17.- Effect of disk loading on aerodynamic characteristics. $\alpha = 0^o$; $\delta_v = 0^o$.

O Uncorrected   Model in 15.7' x 17.0' tunnel
□ Uncorrected   Model in 4.4' x 7.0' tunnel
◰ Corrected   Model in 4.4' x 7.0' tunnel
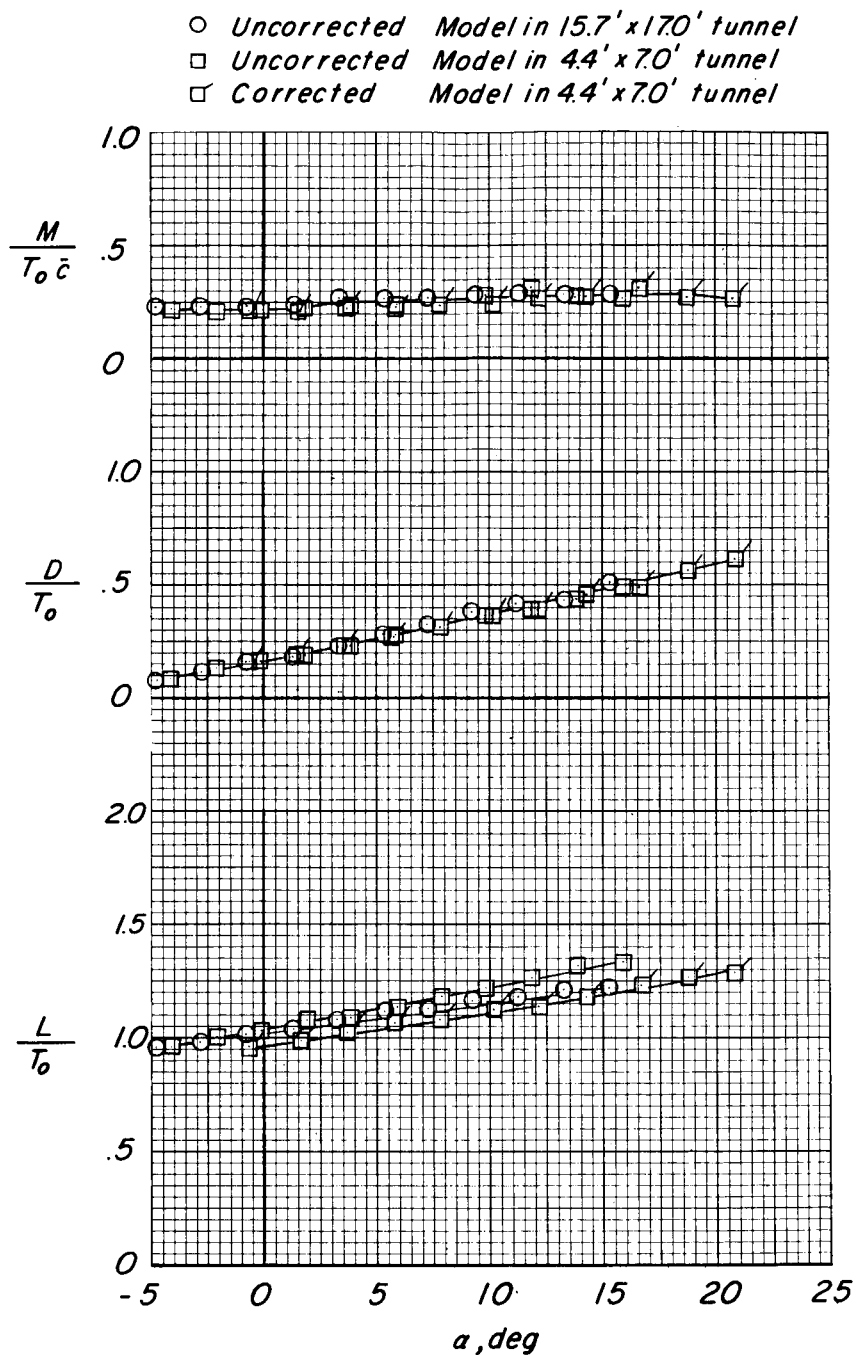
(a) V_∞/V_j = 0.19.

Figure 18.- Aerodynamic characteristics of the model with and without wall corrections.
δ_v = 0°; N = 20,000 rpm.

V_∞/V_j

○	.28	Uncorrected	Model in 15.7' x 17.0' tunnel
□	.29	Uncorrected	Model in 4.4' x 7.0' tunnel
◫	.29	Corrected	Model in 4.4' x 7.0' tunnel
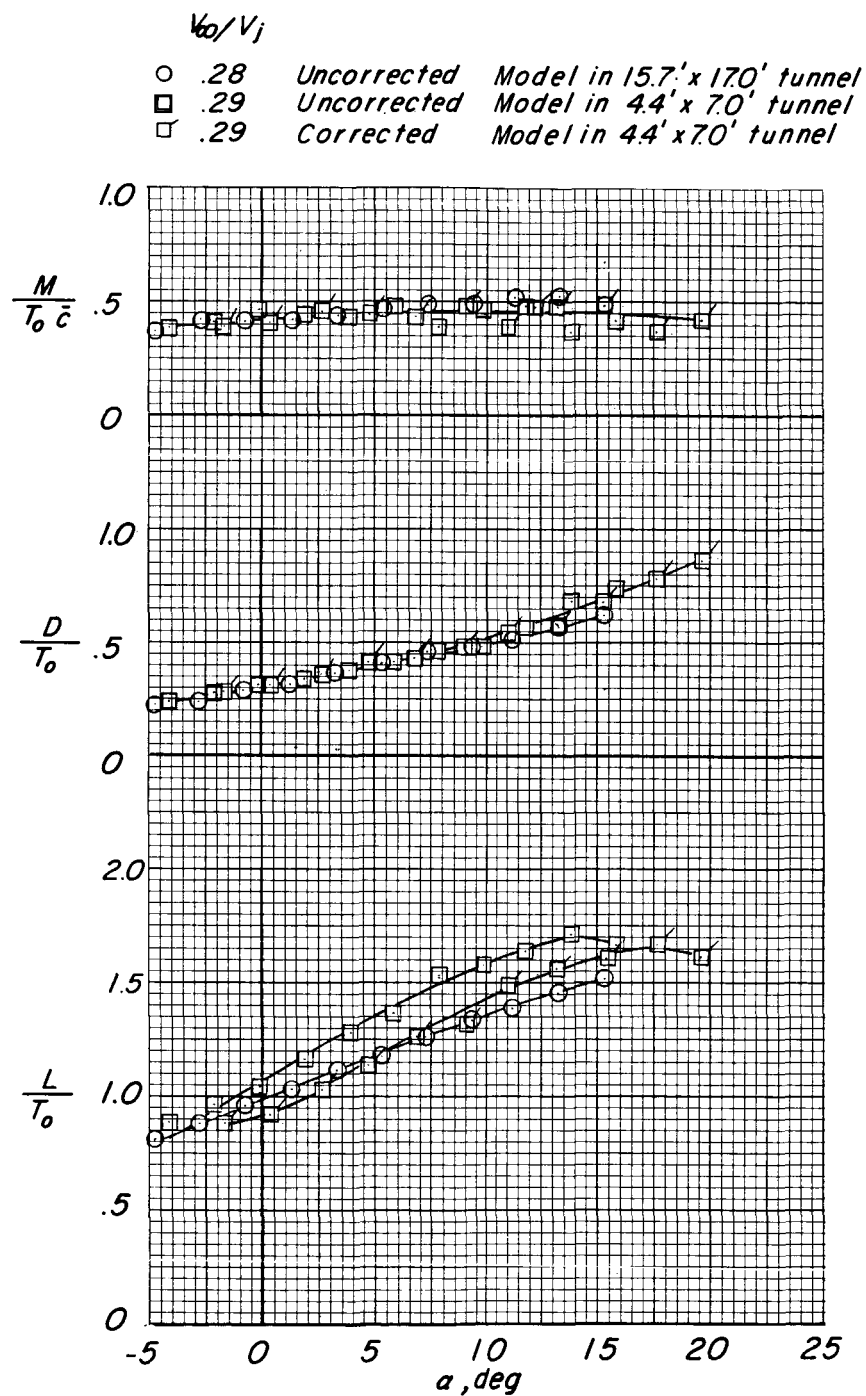
(b) $V_\infty/V_j \approx 0.30.$

Figure 18.- Continued.
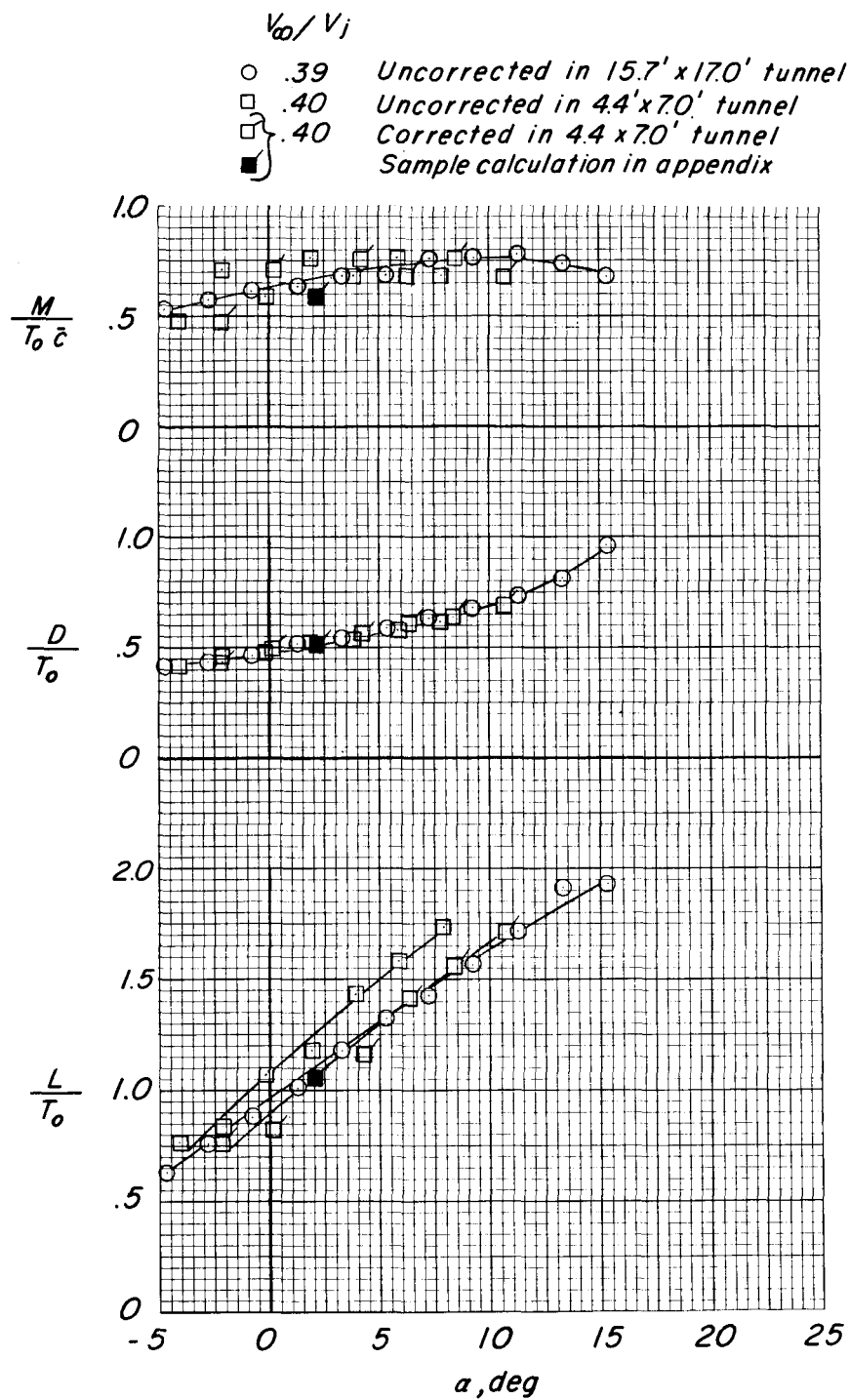
(c) $V_{\infty}/V_j \approx 0.40$.

Figure 18.- Continued.

□ *Uncorrected   Model in 4.4' x 7.0' tunnel*
◨ *Corrected   Model in 4.4' x 7.0' tunnel*
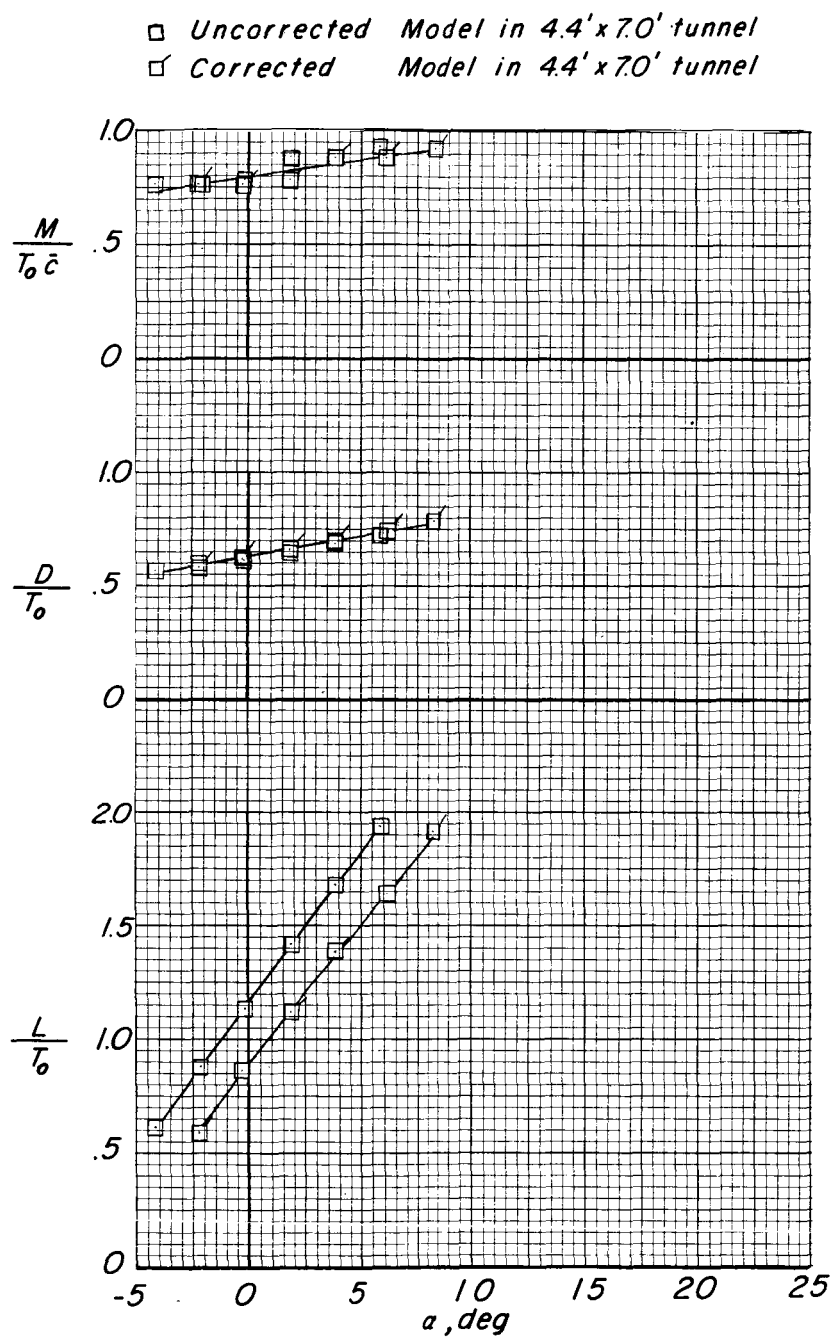
(d) $V_\infty/V_j = 0.49.$

Figure 18.- Concluded.
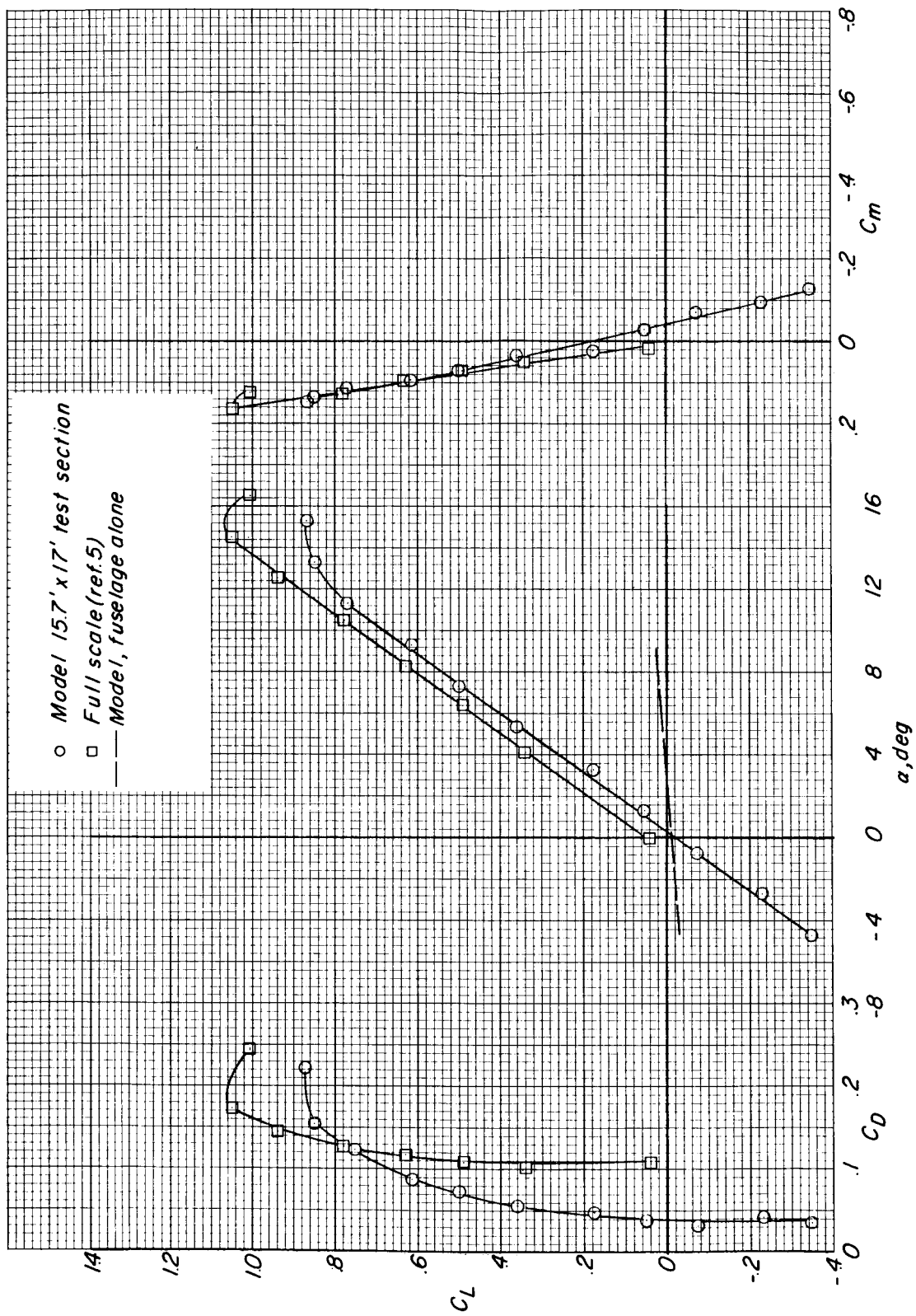
Figure 19.- Comparison of model and full-scale power-off data.

54
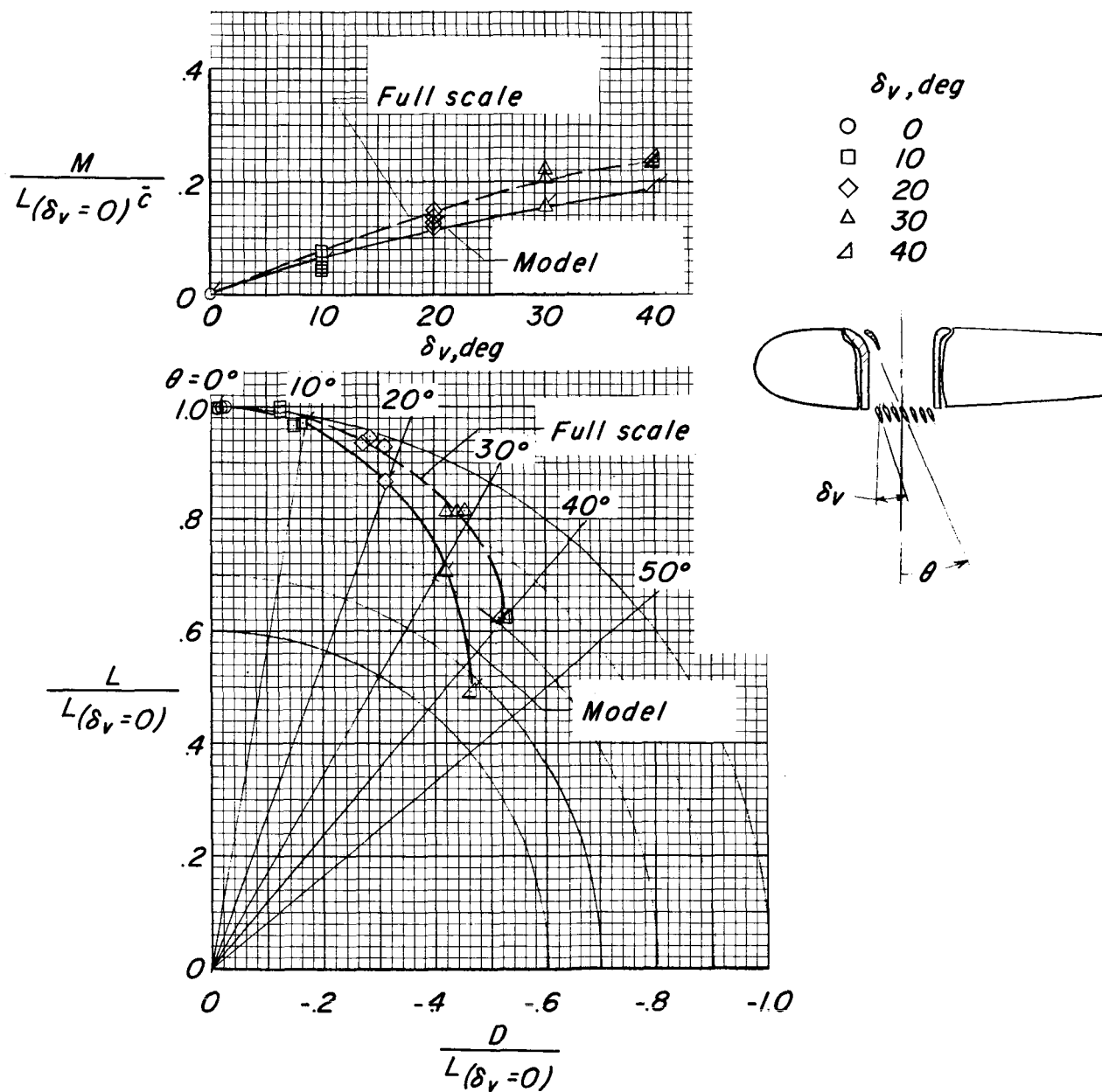
Figure 20.- Comparison of model and full-scale exit-vane effectiveness.
$\alpha = 0°$; $V_\infty/V_j = 0$.

○　.21　Uncorrected⎫
◑　.21　Corrected　　⎬　Full scale ref.5
□　.19　Uncorrected　Model in 15.7' x17.0' tunnel
◧　.19　Corrected　　Model in 4.4' x7.0' tunnel
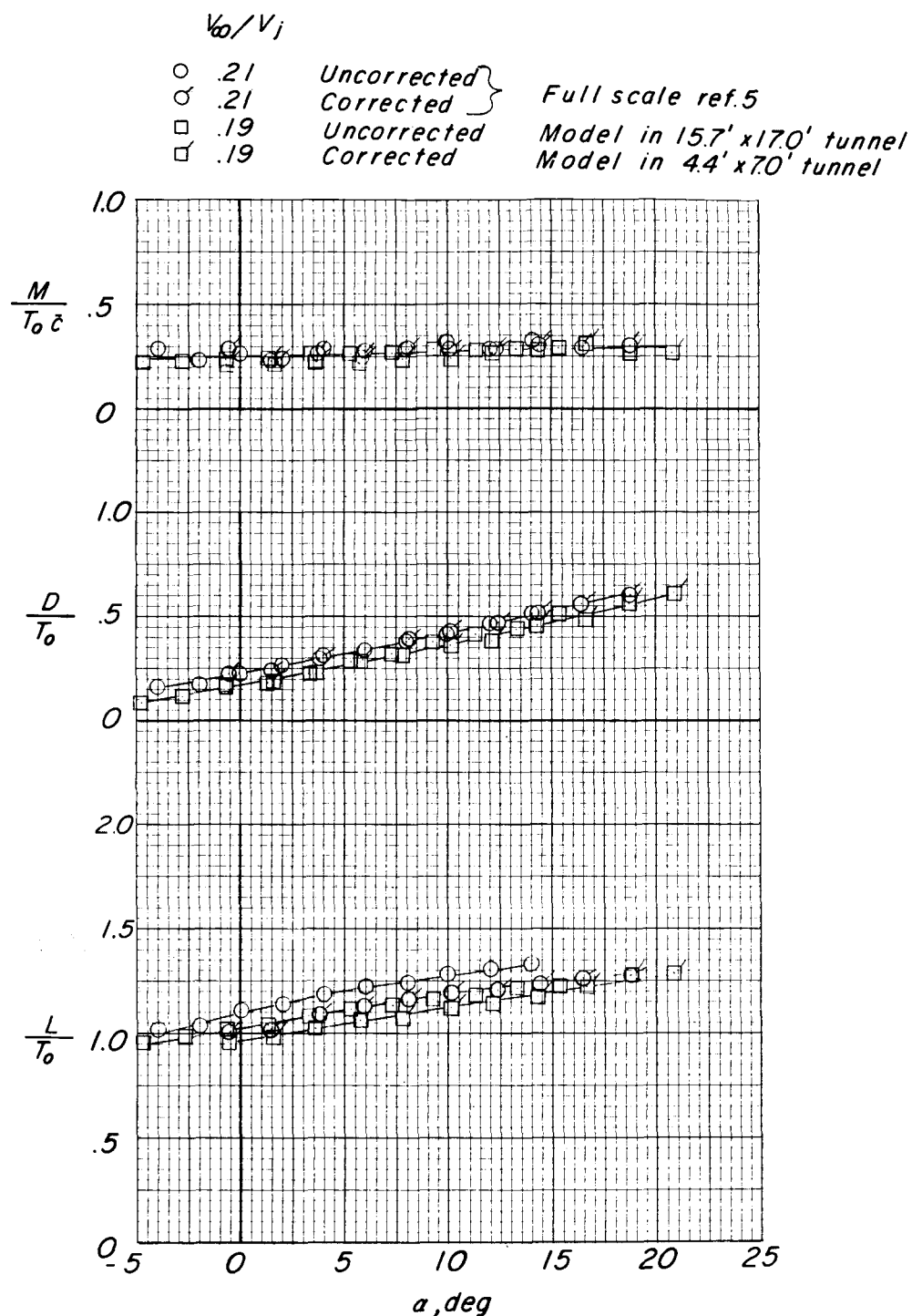
(a)　$V_\infty/V_j \approx 0.20.$

Figure 21.- Comparison of model and full-scale power-on data at forward speed.　$\delta_v = 0°.$

○   .41   Uncorrected ⎫ Full scale ref.5
◁   .41   Corrected ⎭
□   .39   Uncorrected   Model in 15.7' x 17.0' tunnel
◁   .40   Corrected   Model in 4.4' x 7.0' tunnel

$\frac{M}{T_o \bar{c}}$

$\frac{D}{T_o}$

$\frac{L}{T_o}$

a ,deg
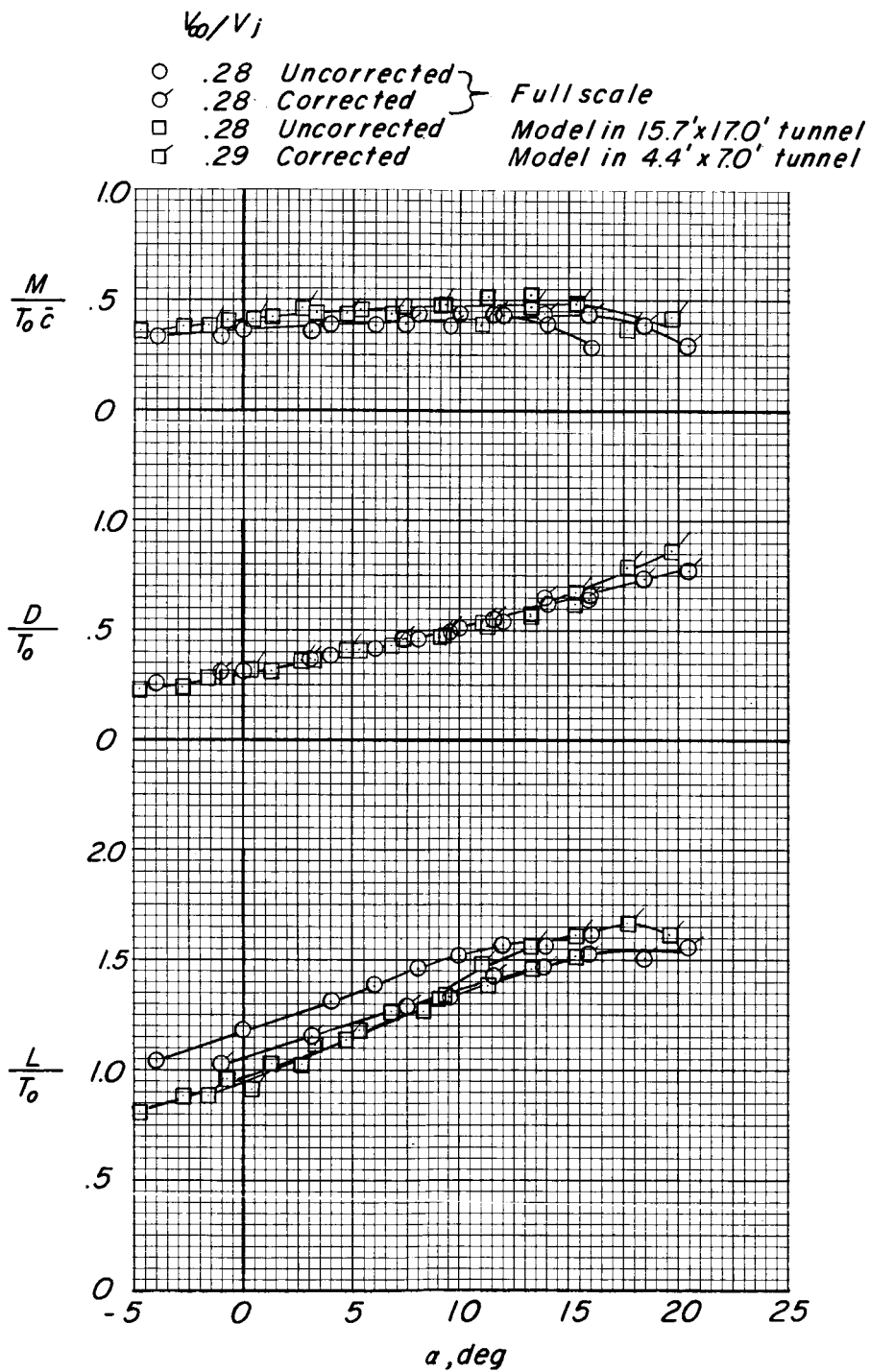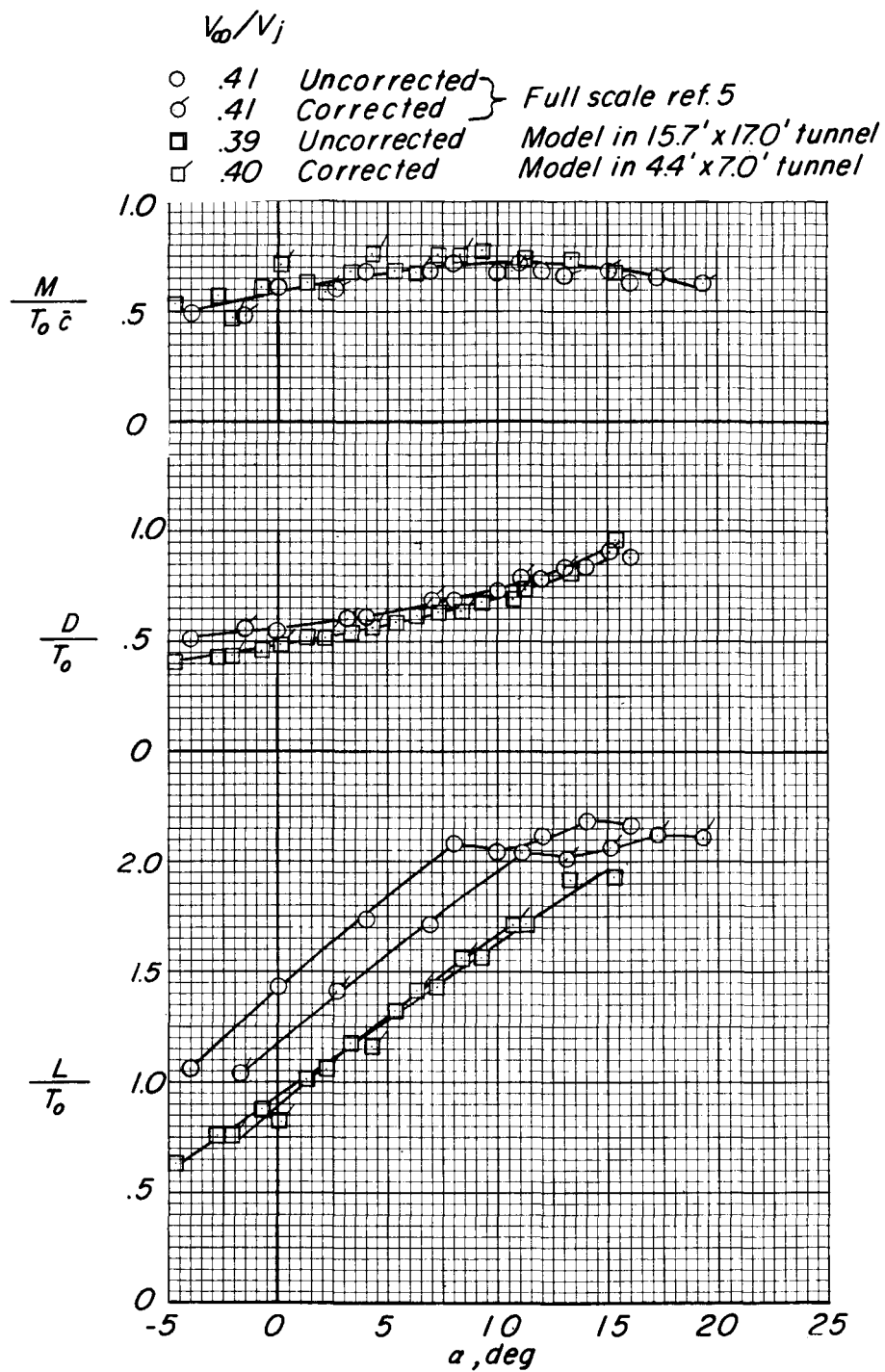
(c) $V_\infty/V_j \approx 0.40$.

Figure 21.- Concluded.
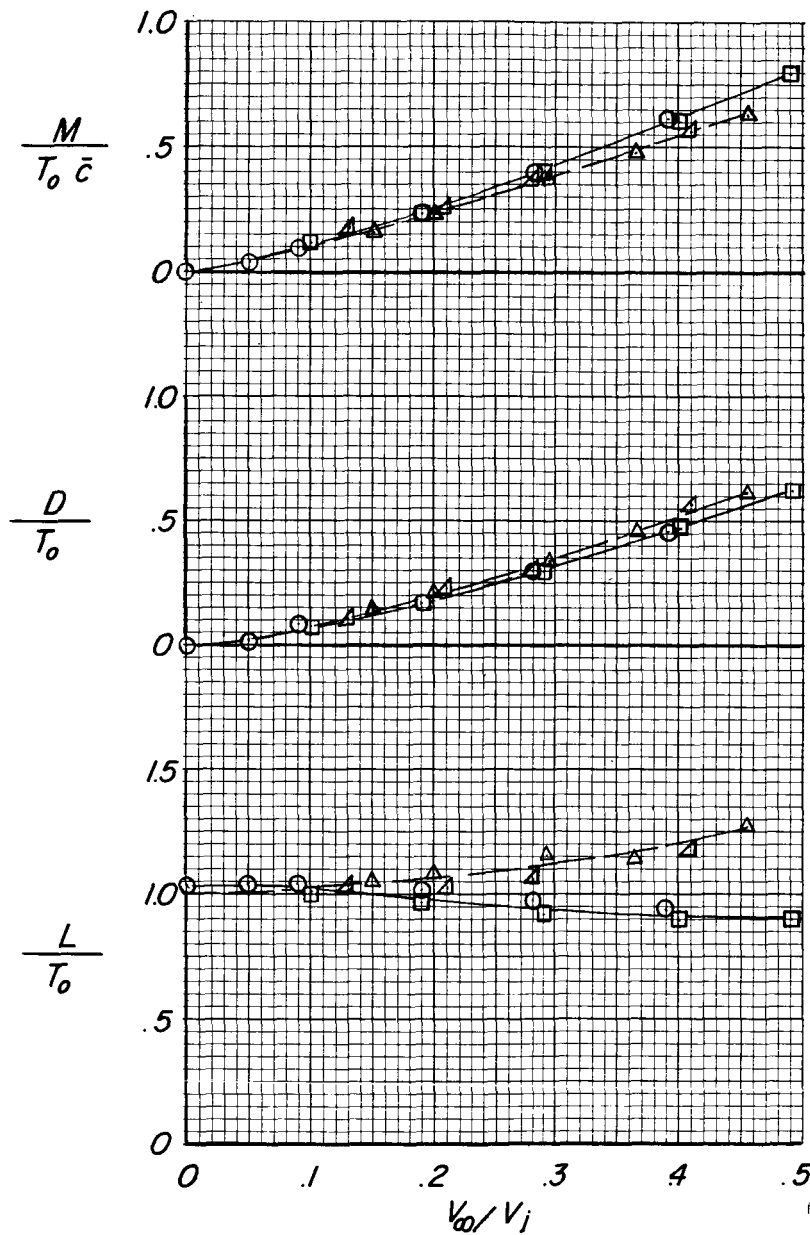
Figure 22.- Comparison of model and full-scale aerodynamic characteristics for two exit-vane settings. $\alpha = 0°$.
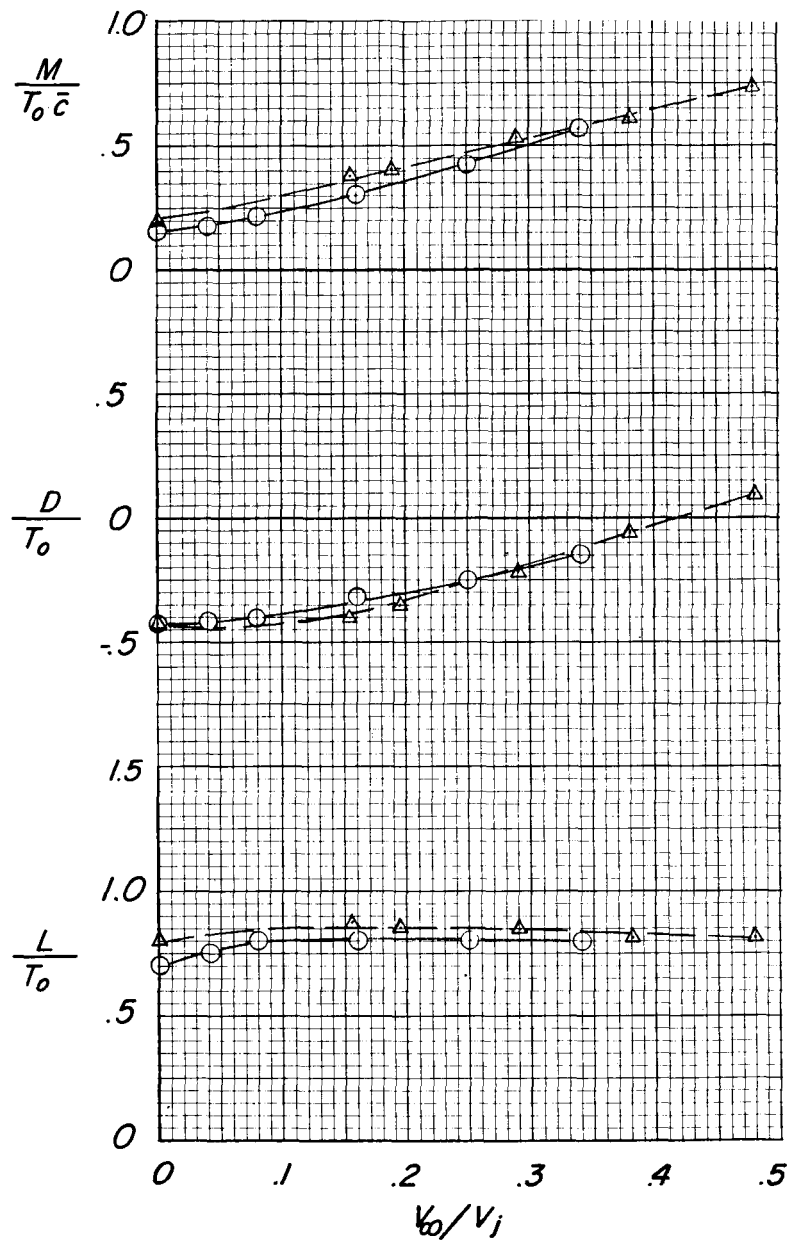
(b) $\delta_v = 30°$.

Figure 22.- Concluded.
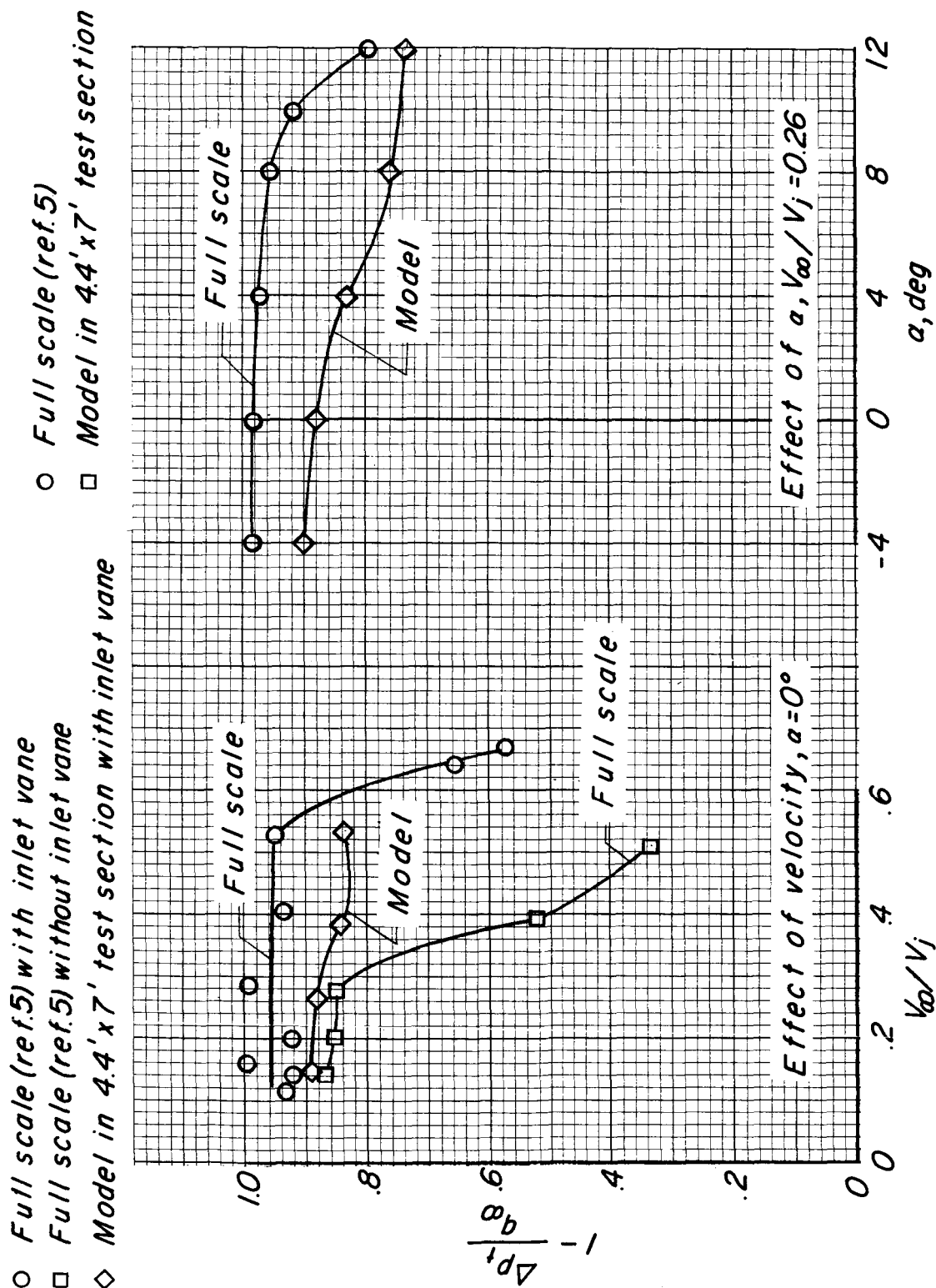
(a) Effect of velocity and angle of attack on ram recovery.

Figure 23.- Inlet characteristics.

V_O

Inlet vane

$$\frac{\Delta p_{t,\infty}}{q_\infty}$$

-1.0
-2.0
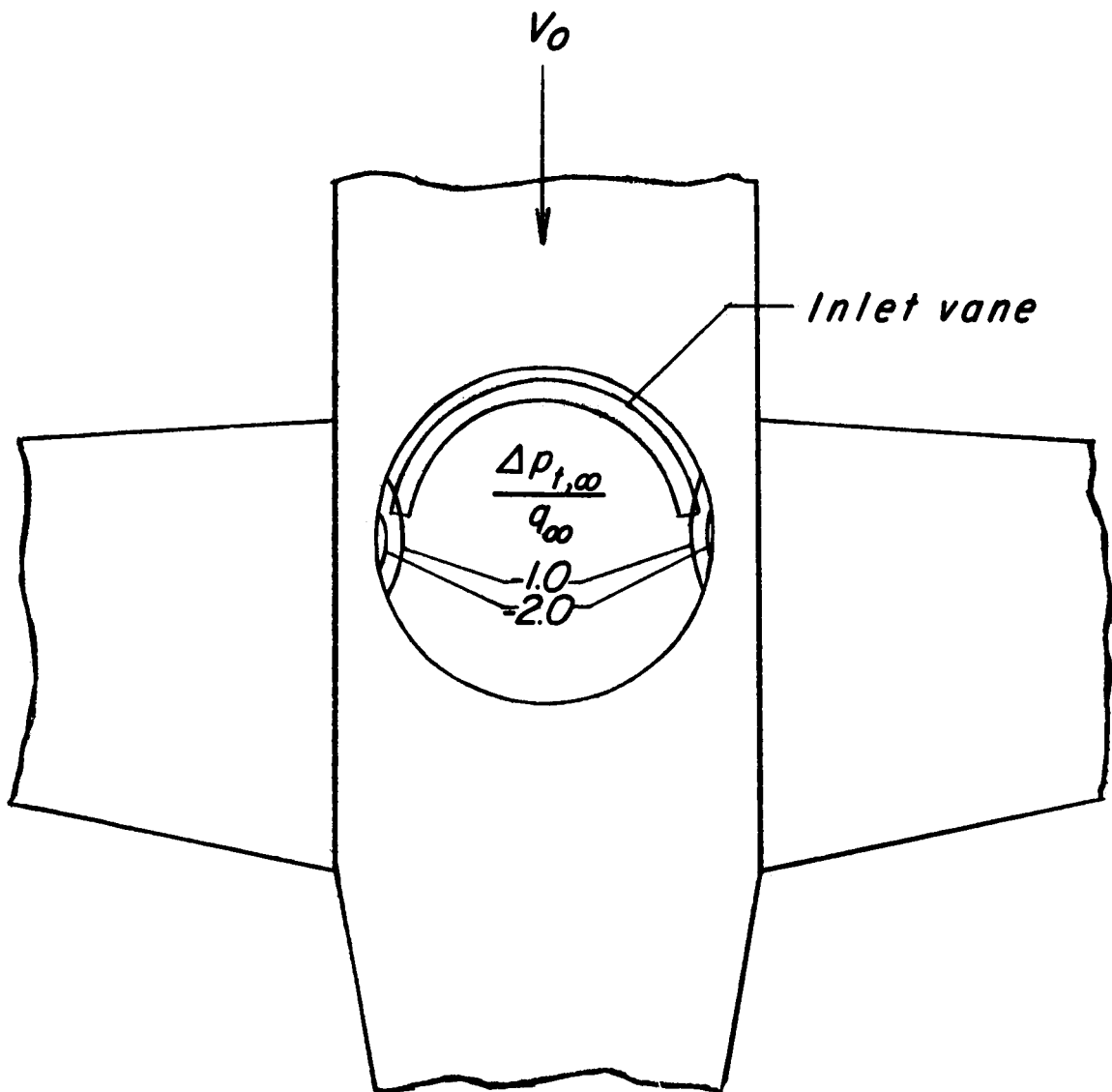
(b) Areas suffering inlet losses (summary of inlet rake data).

Figure 23.- Concluded.
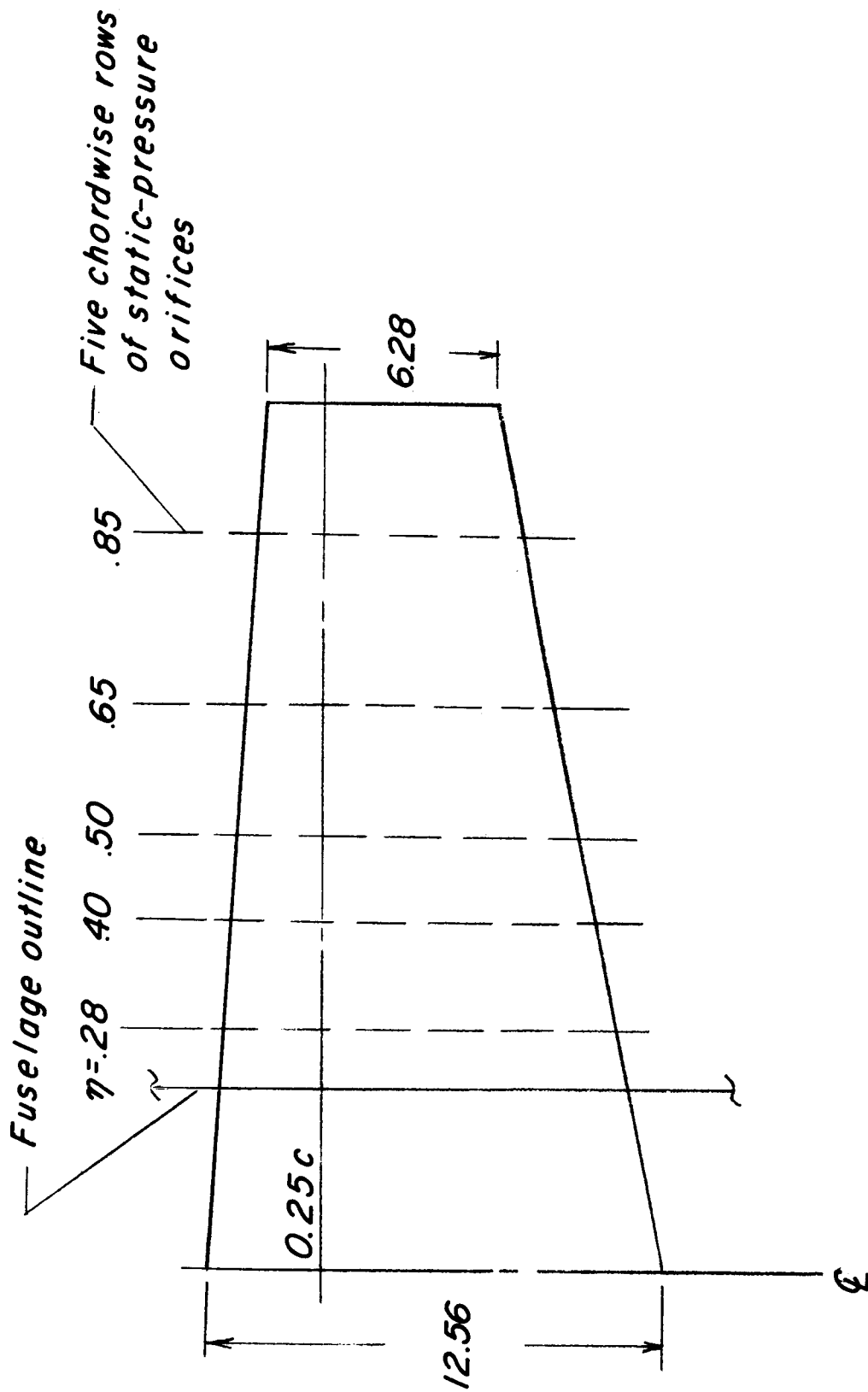
Figure 24.- Pressure-orifice stations. All dimensions are in inches.
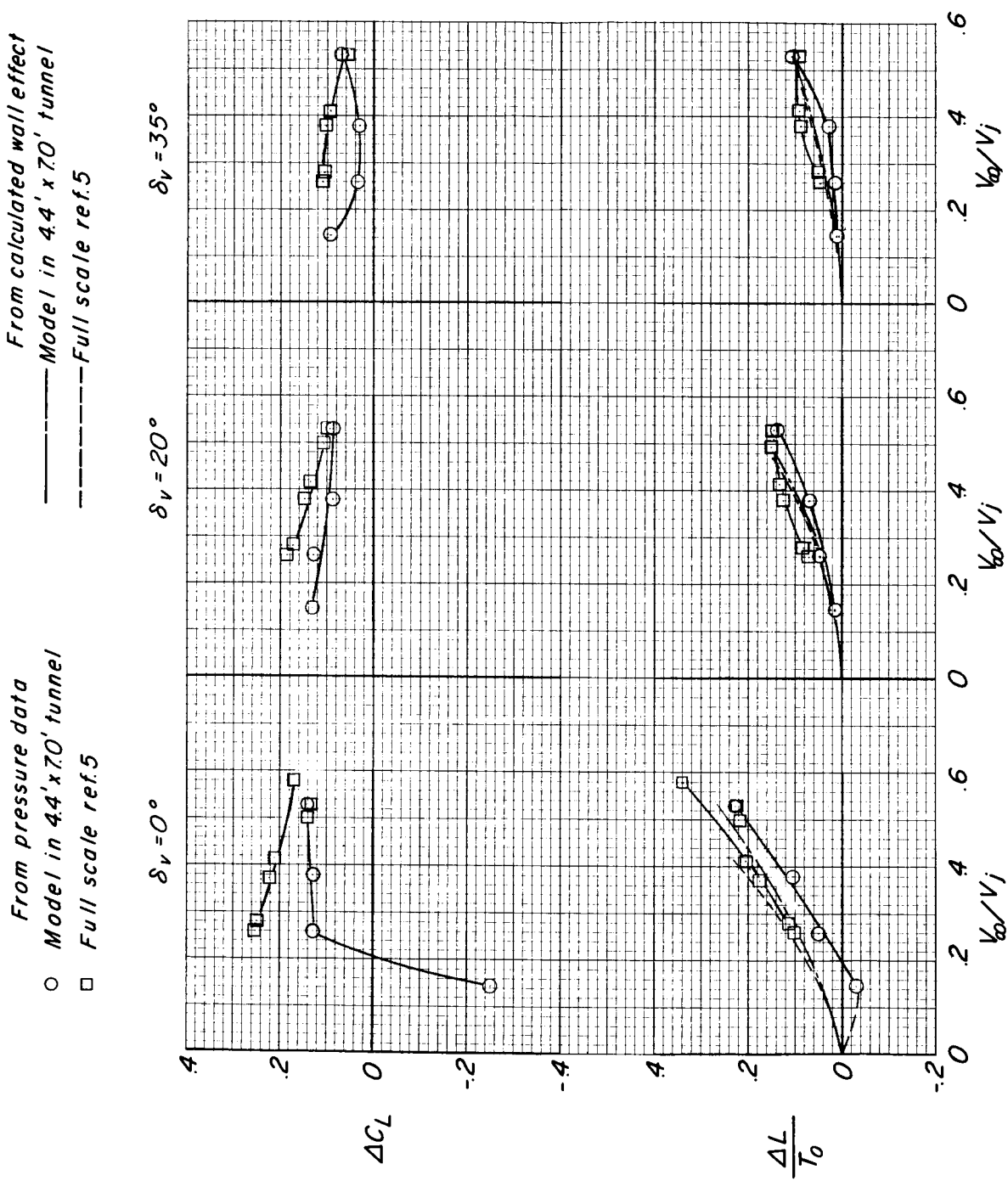
Figure 25.- Comparison of model and full-scale wing lift as obtained from pressure-distribution integration and from wall-induced upwash for three exit-vane settings. α = 0°.

64
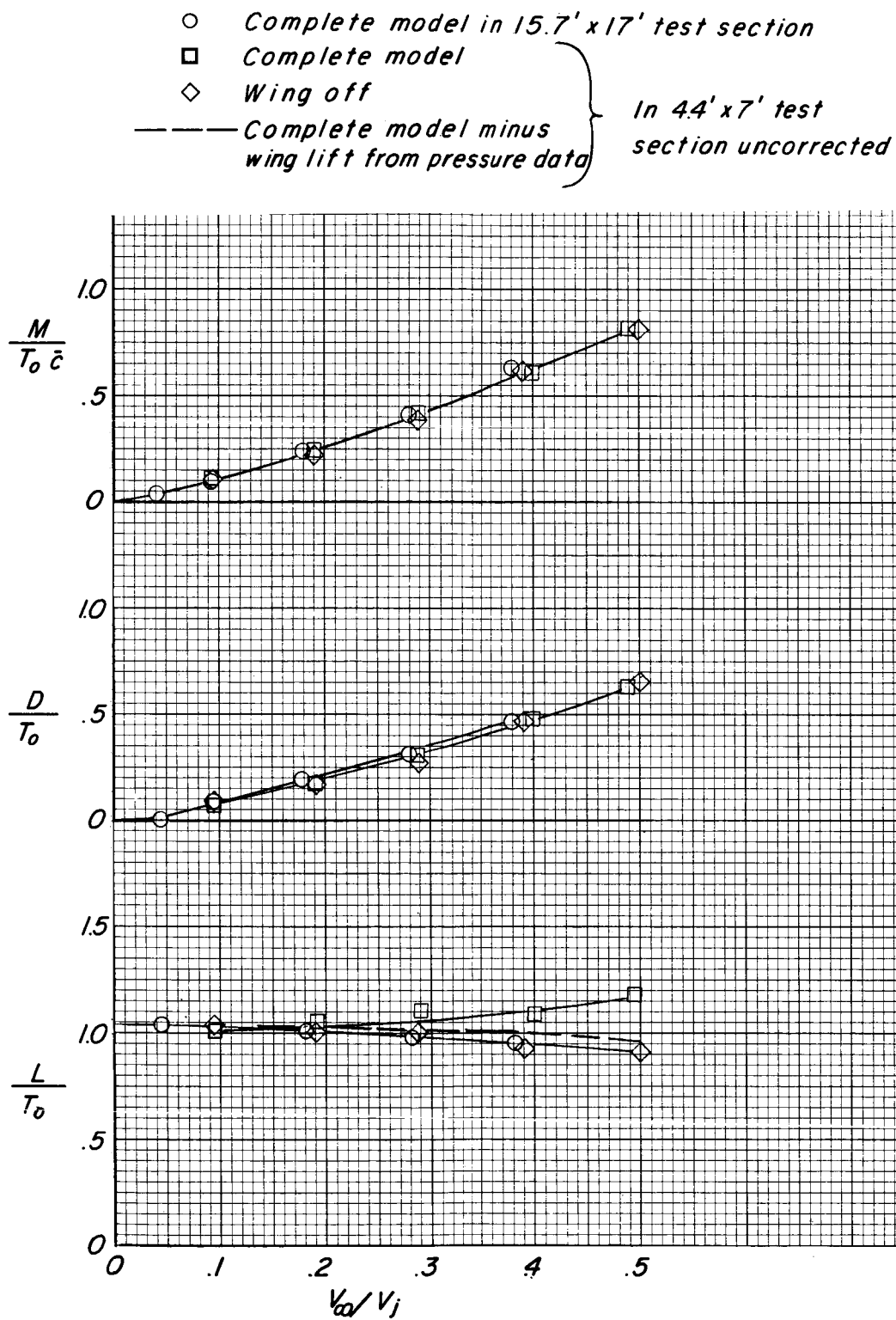
Figure 26.- Analysis of model aerodynamic characteristics with forward speed. $\alpha = 0^{\circ}$.
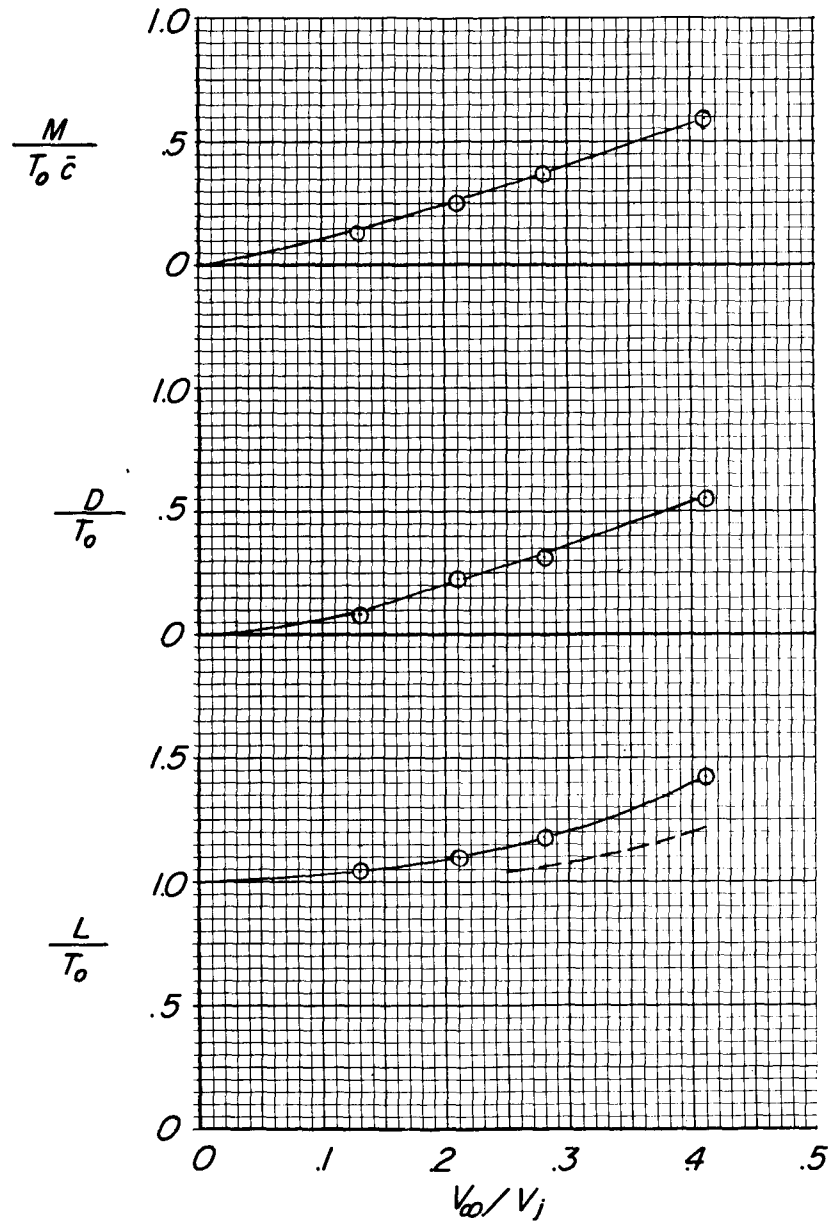
Figure 27.- Analysis of full-scale aerodynamic characteristics with forward speed (from ref. 5). $\alpha = 0°$.
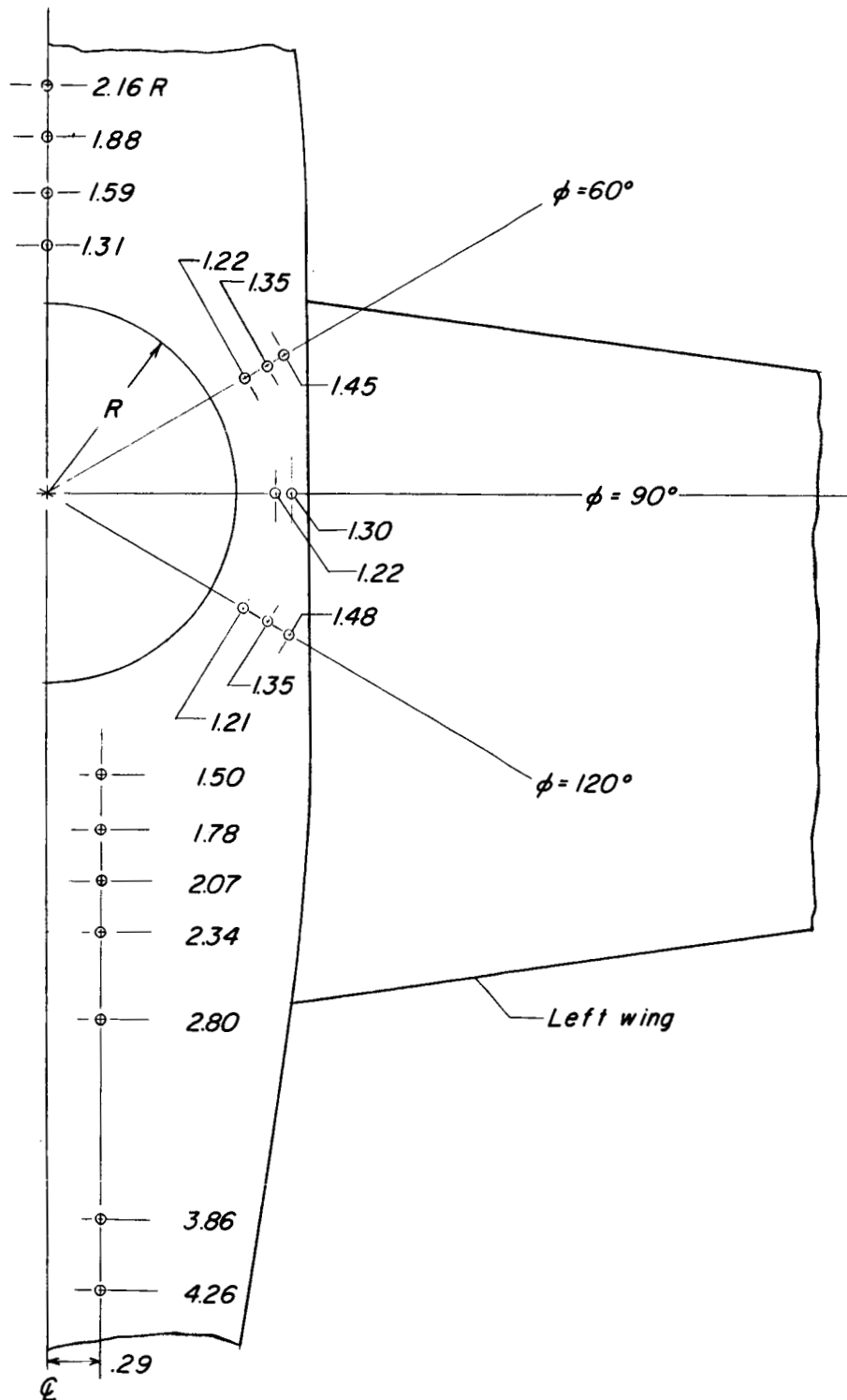
Figure 28.- Lower-surface static-pressure-orifice locations. All values are in terms of fan radius.

(a) $V_\infty/V_j = 0.15$.
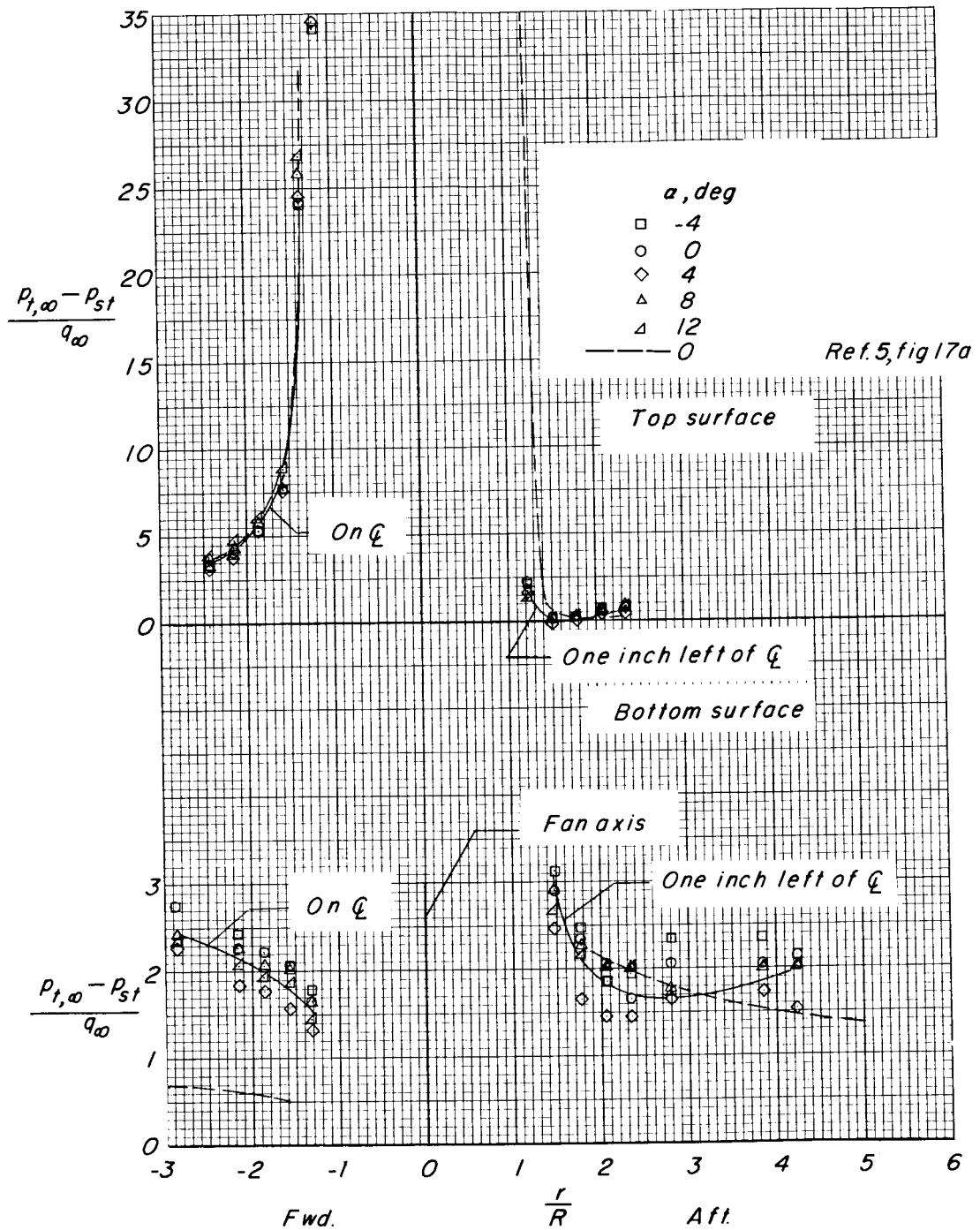
Figure 29.- Longitudinal pressure distribution on the fuselage for four values of V_∞/V_j at $\delta_v = 0°$. Data from reference 5 were obtained along fuselage center line.
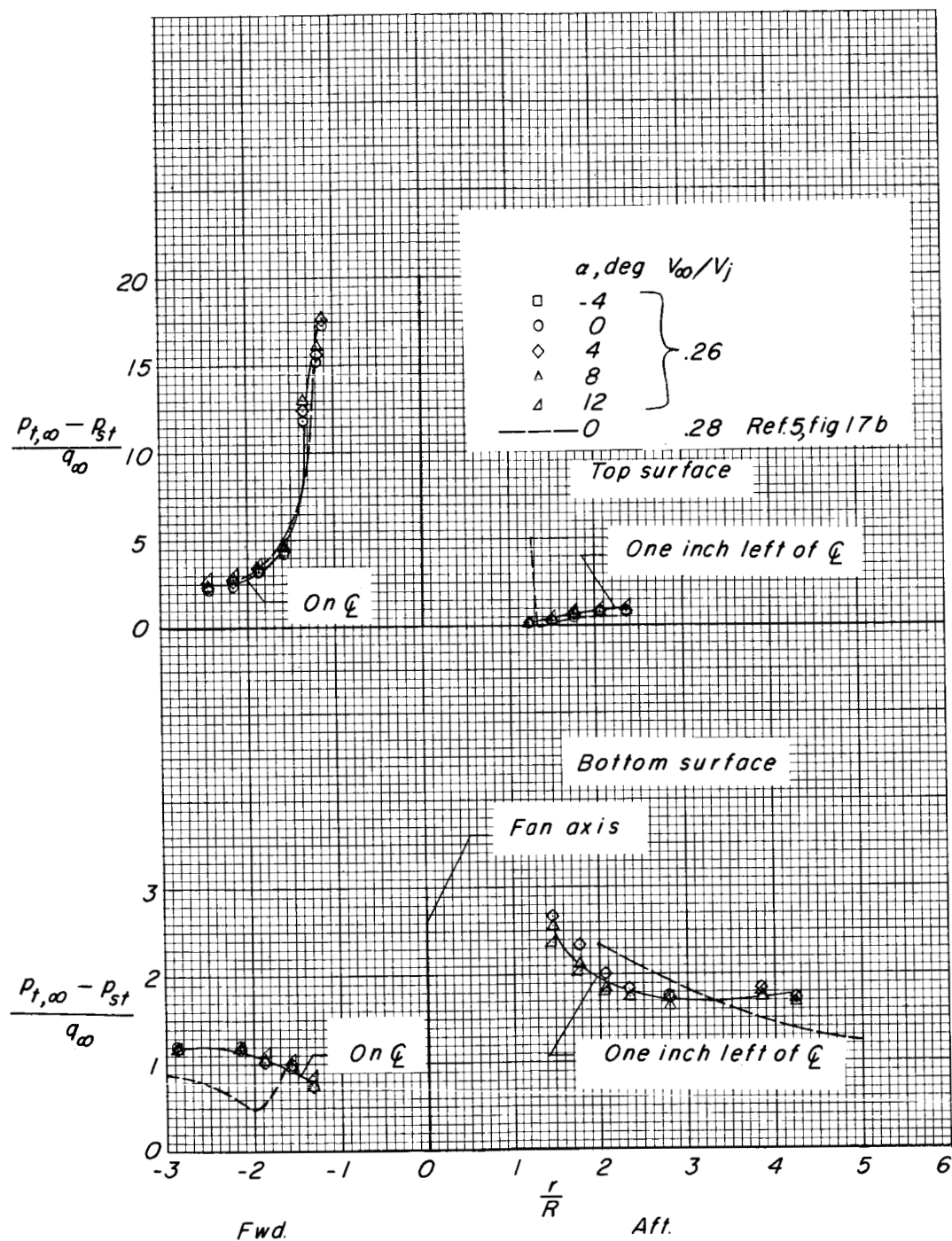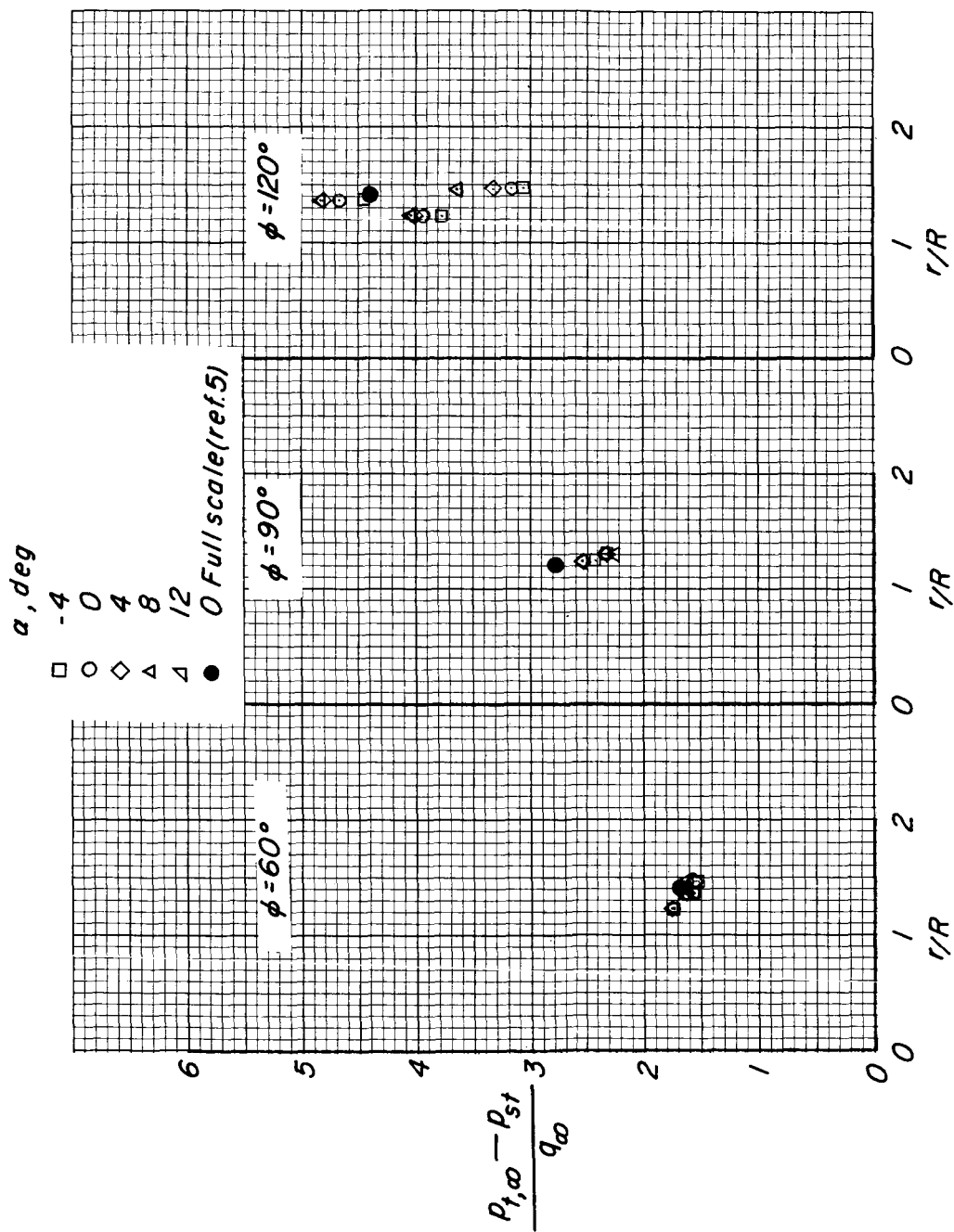
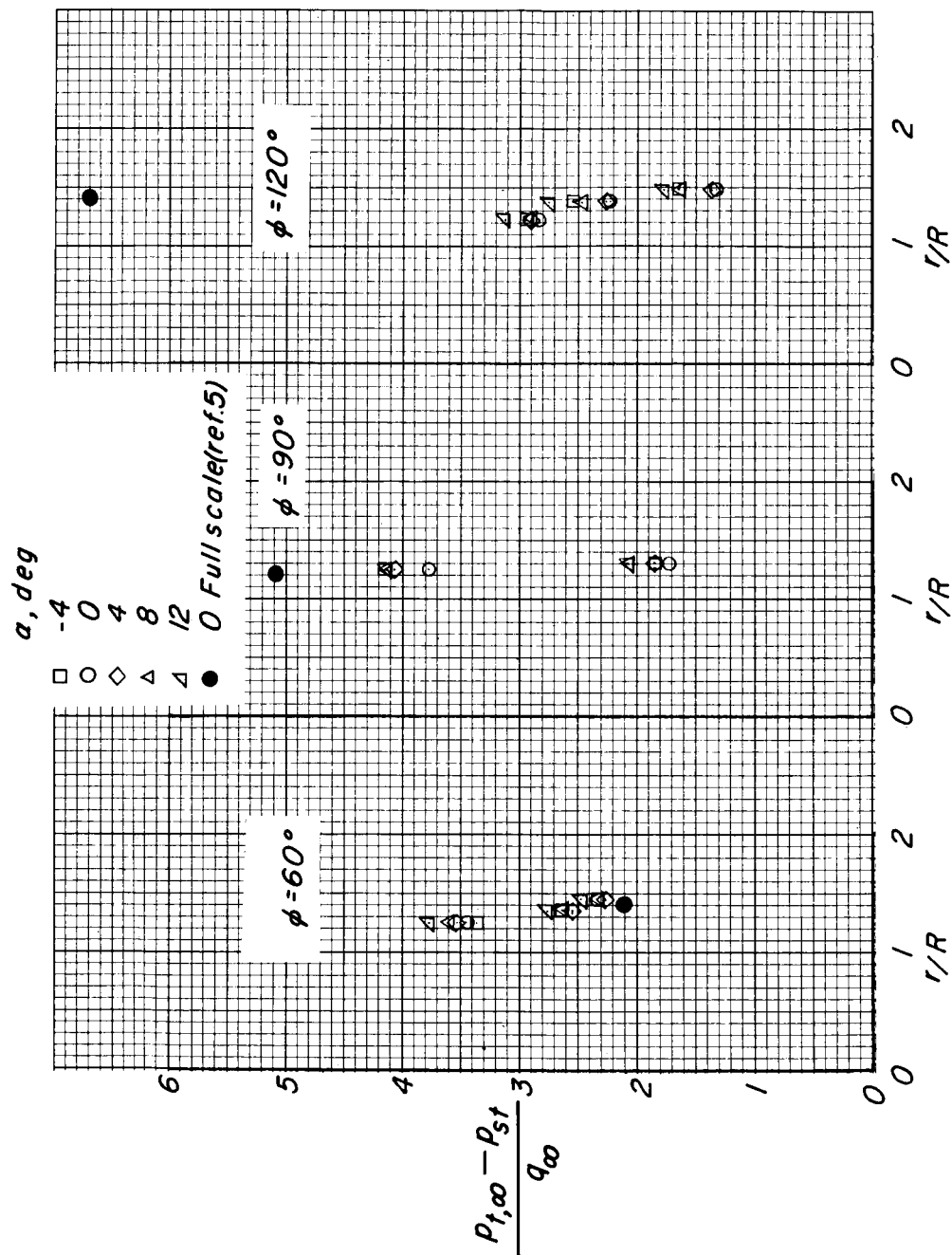(b) $V_\infty/V_j \approx 0.26$.

Figure 29.- Continued.
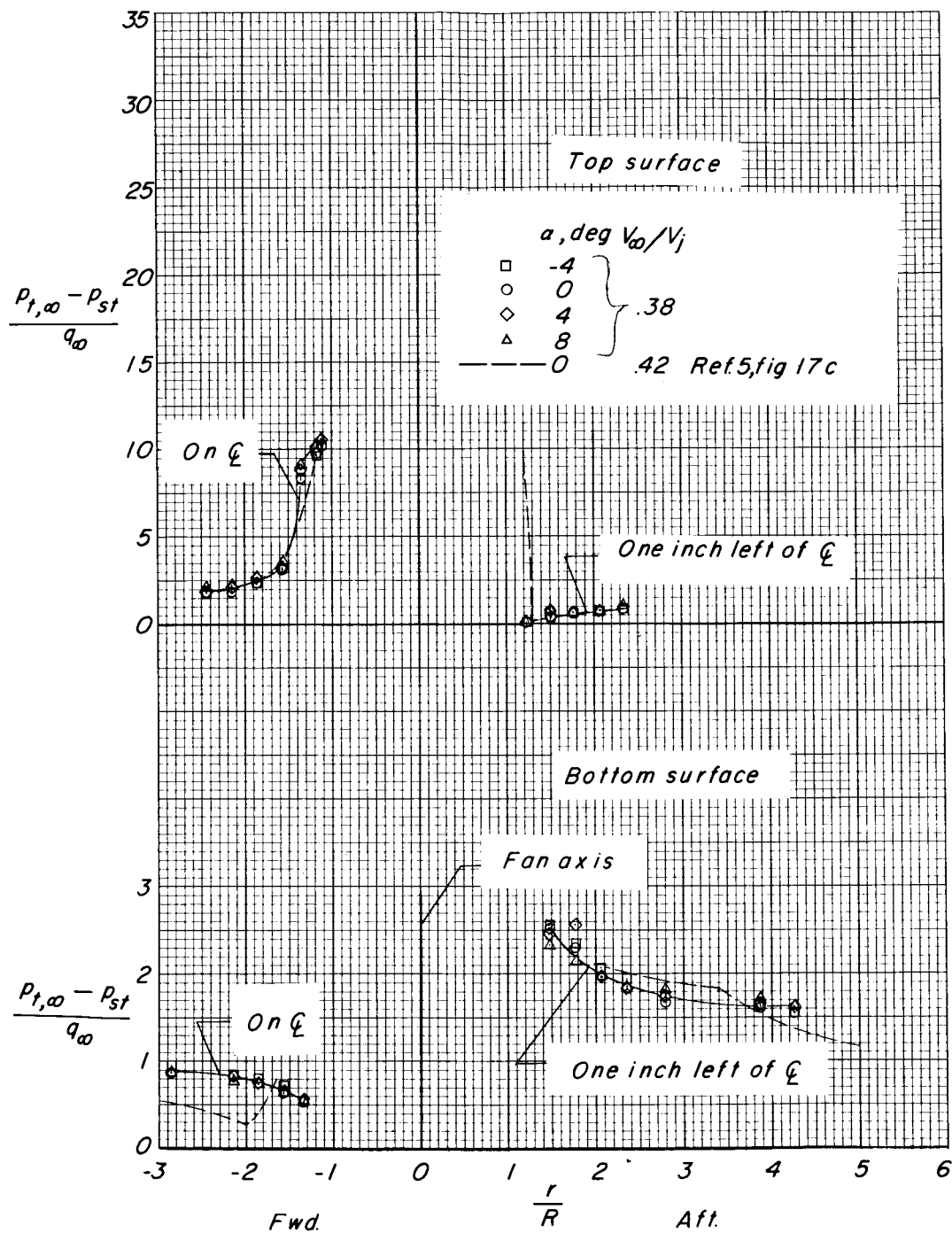
(c) $V_\infty/V_j \approx 0.38$.

Figure 29.- Continued.
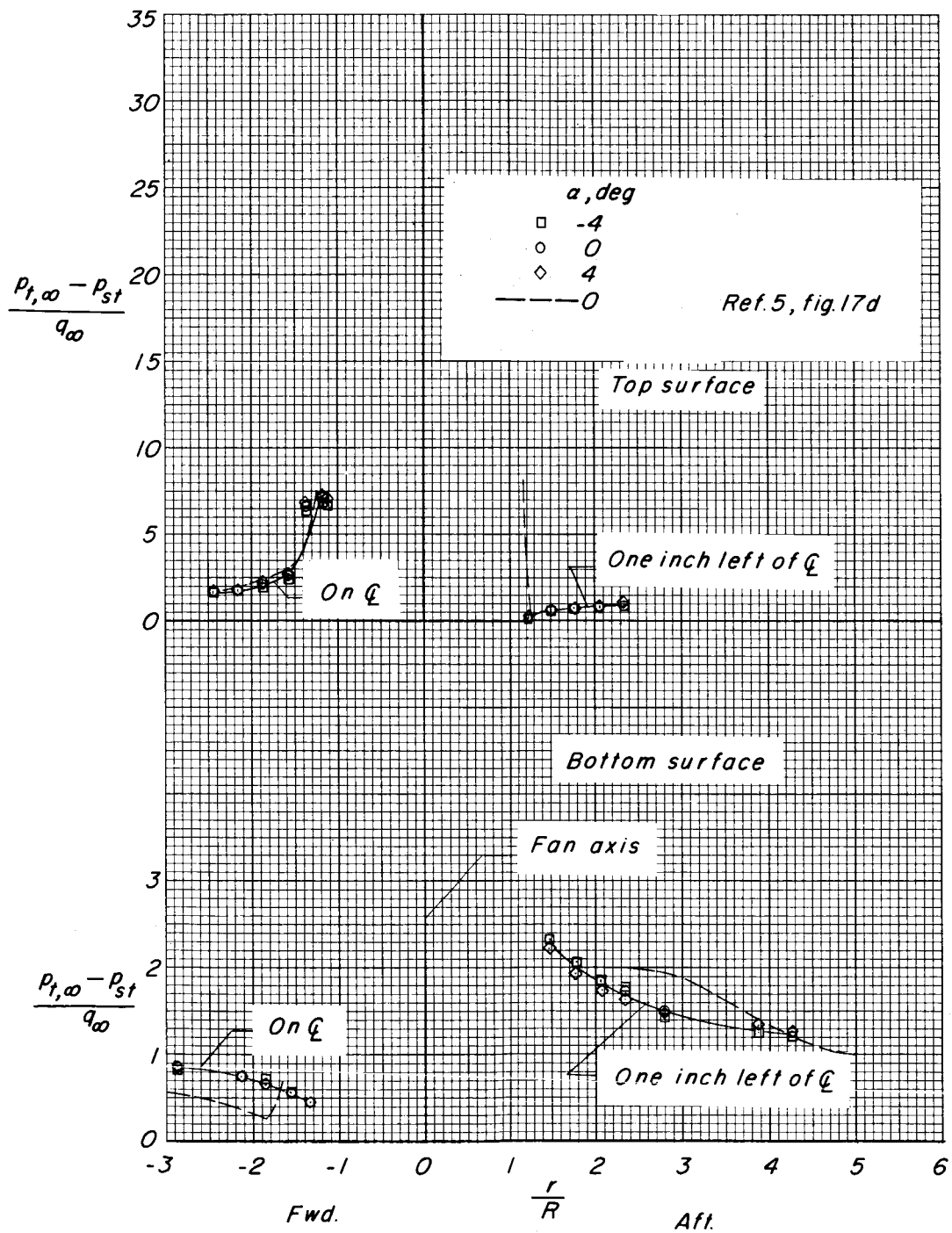
(d) $V_\infty/V_j = 0.53$.

Figure 29.- Concluded.
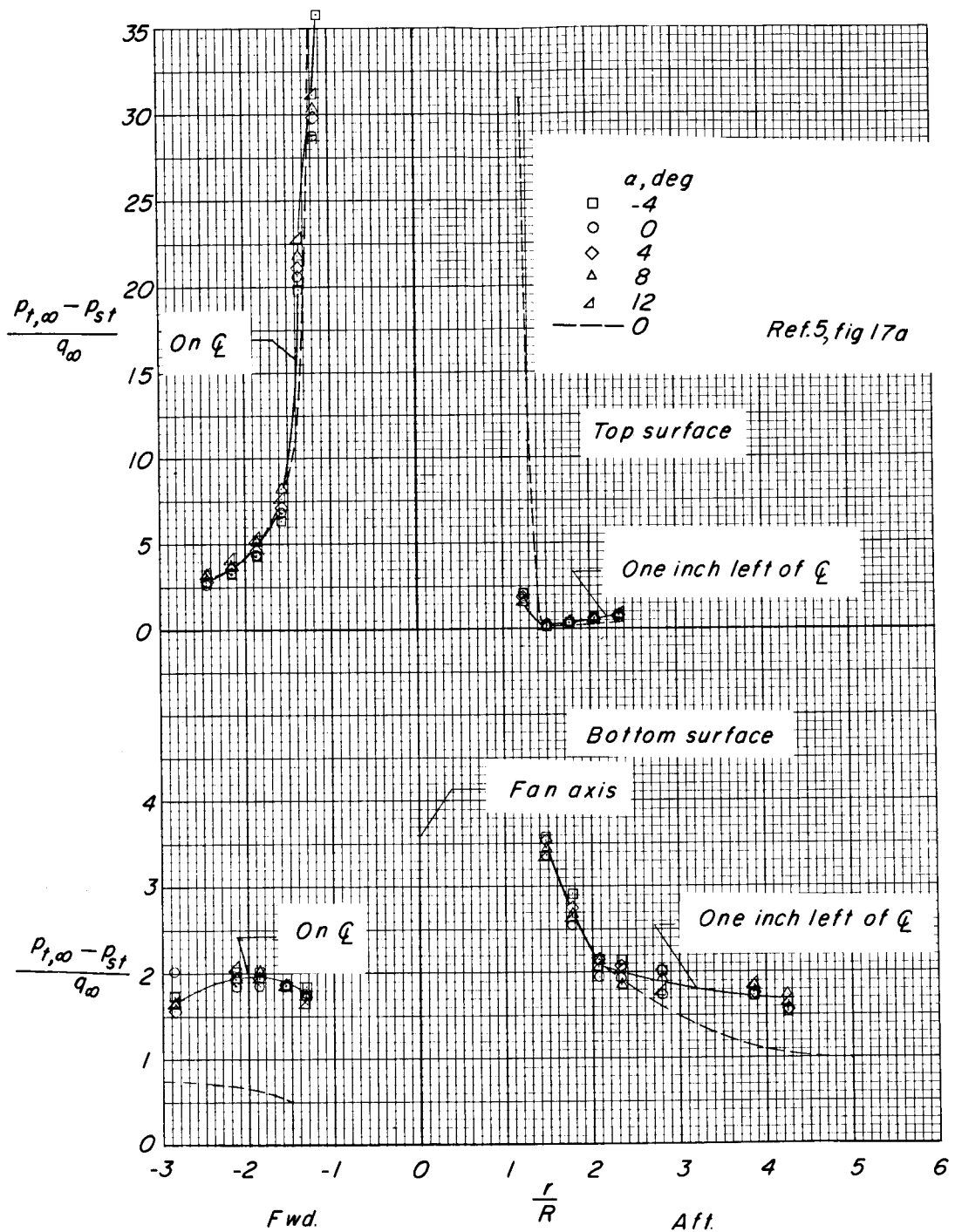
(a) $V_\infty/V_j = 0.15.$

Figure 30.- Longitudinal pressure distribution on the fuselage for four values of V_∞/V_j at $\delta_v = 20°$. Data from reference 5 were obtained along fuselage center line.
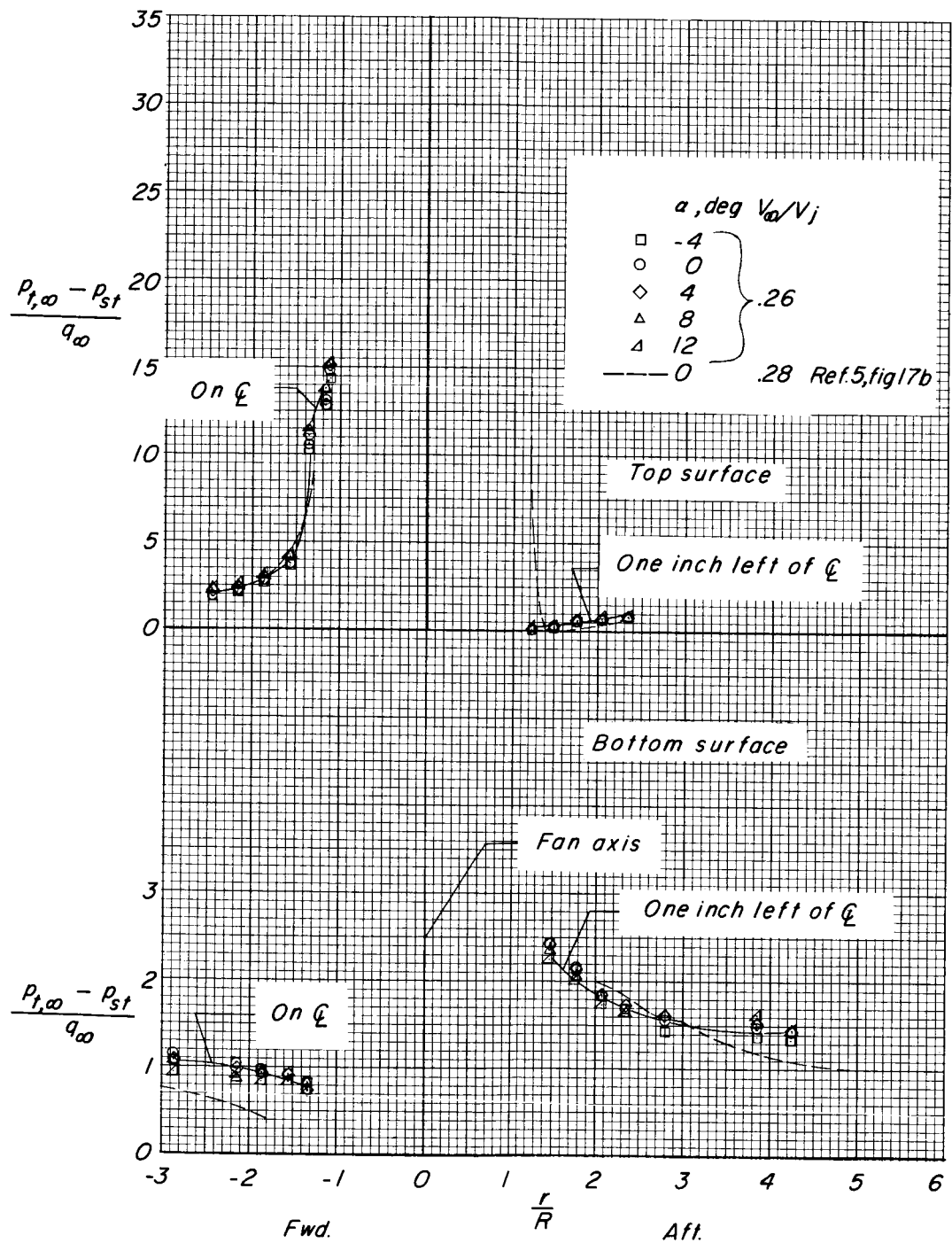
(b) $V_\infty/V_j \approx 0.30$.

Figure 30.- Continued.
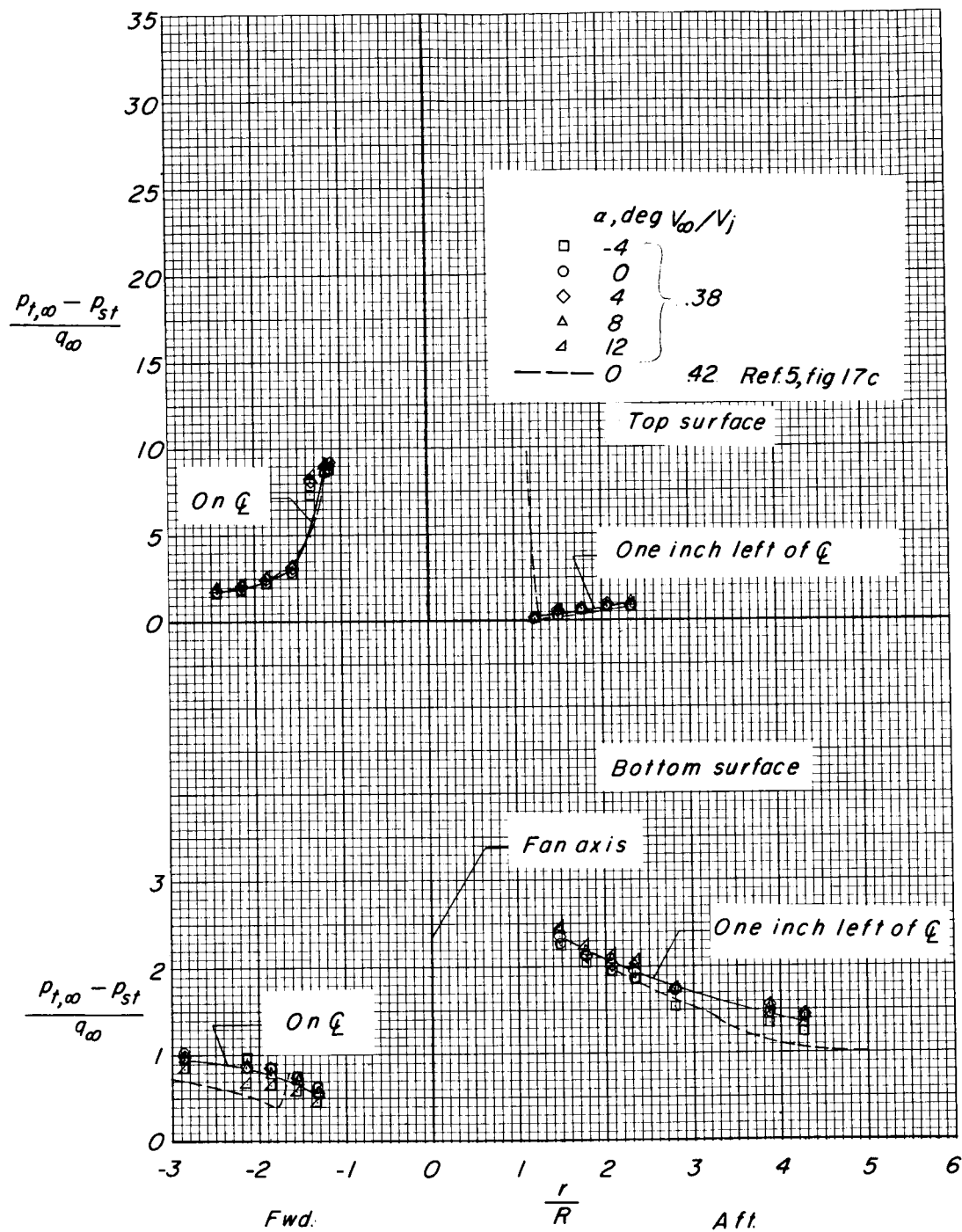
(c) $V_\infty/V_j \approx 0.40$.

Figure 30.- Continued.
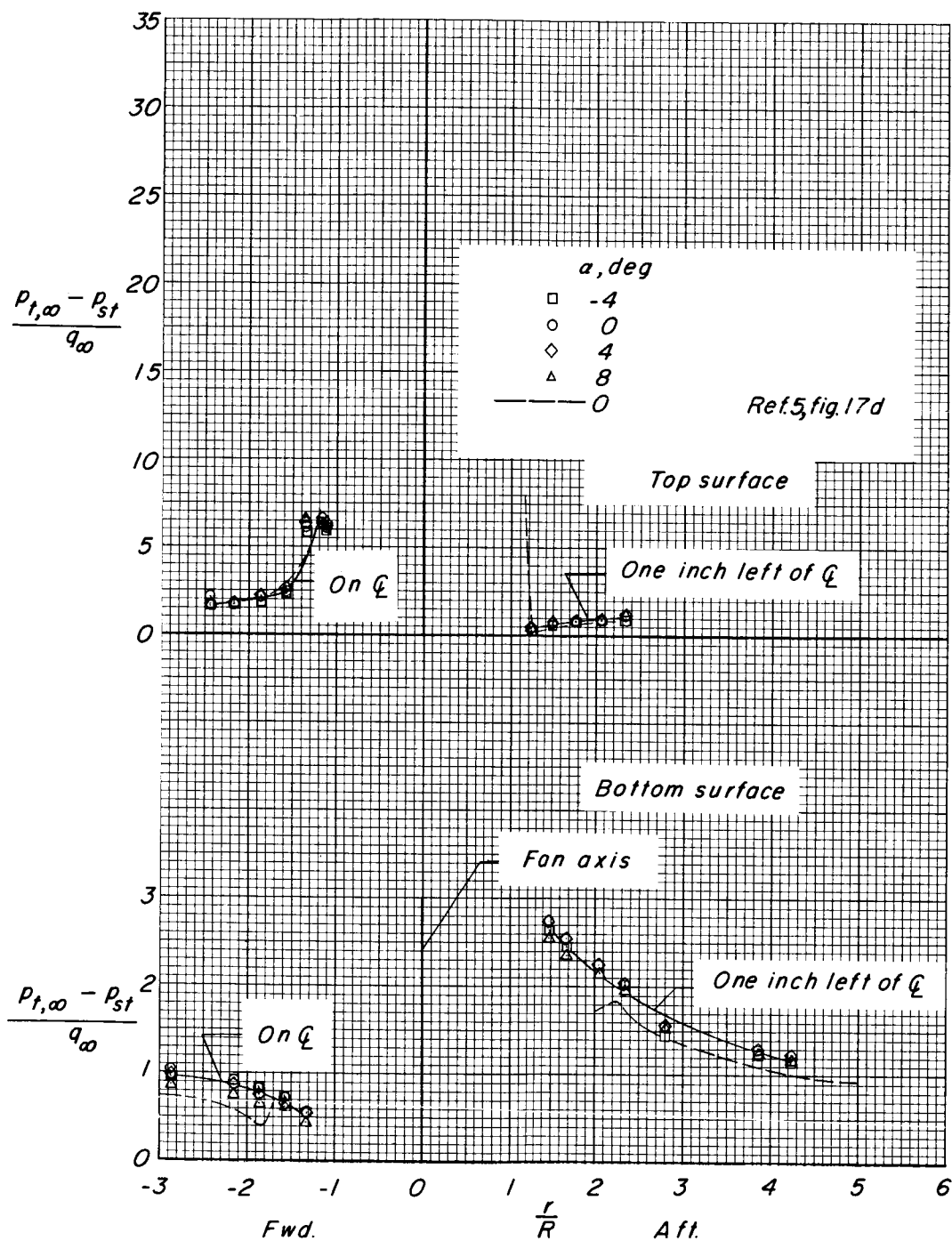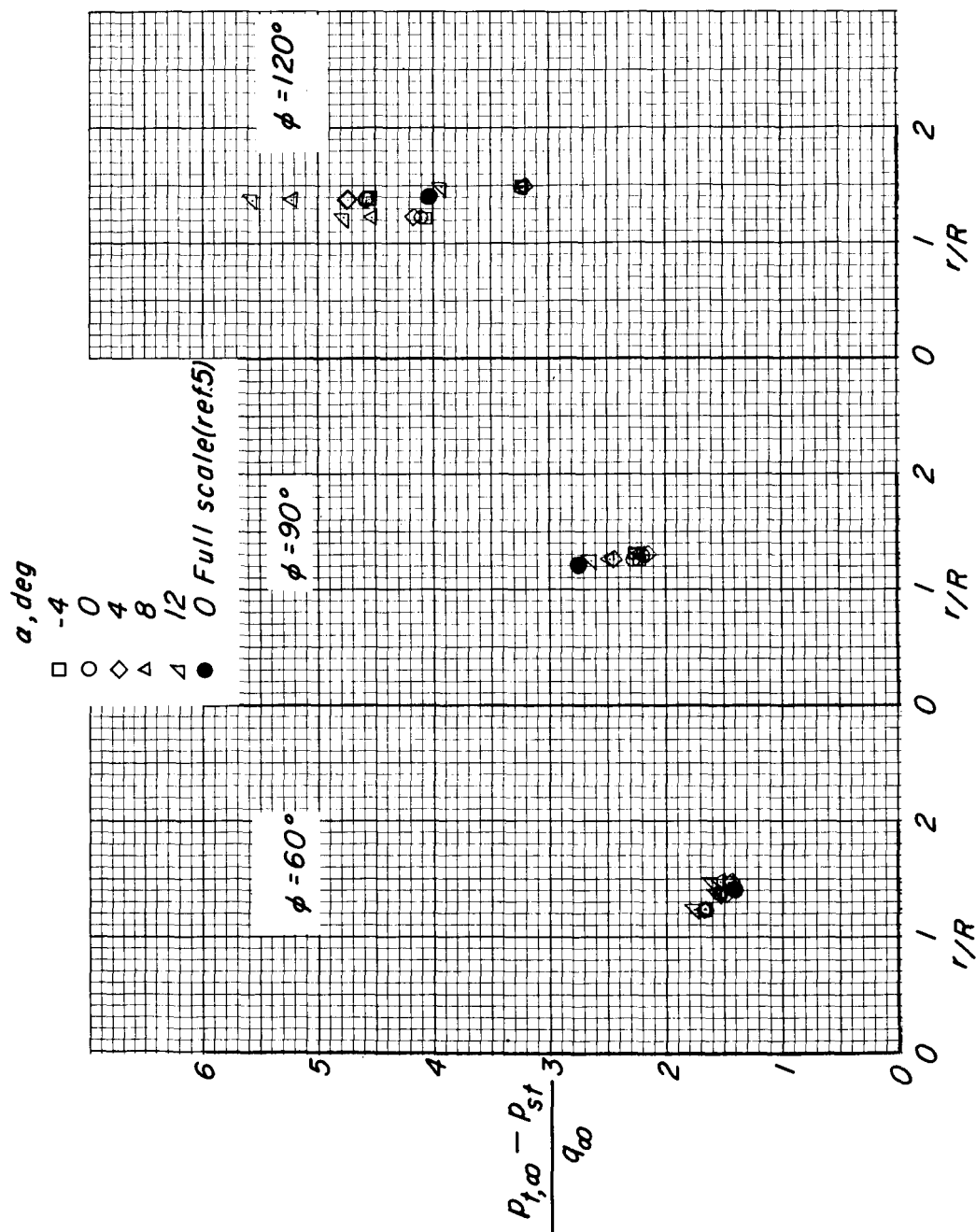
(d) $V_\infty/V_j = 0.53$.

Figure 30.- Concluded.

(a) $V_\infty/V_j = 0.15$.
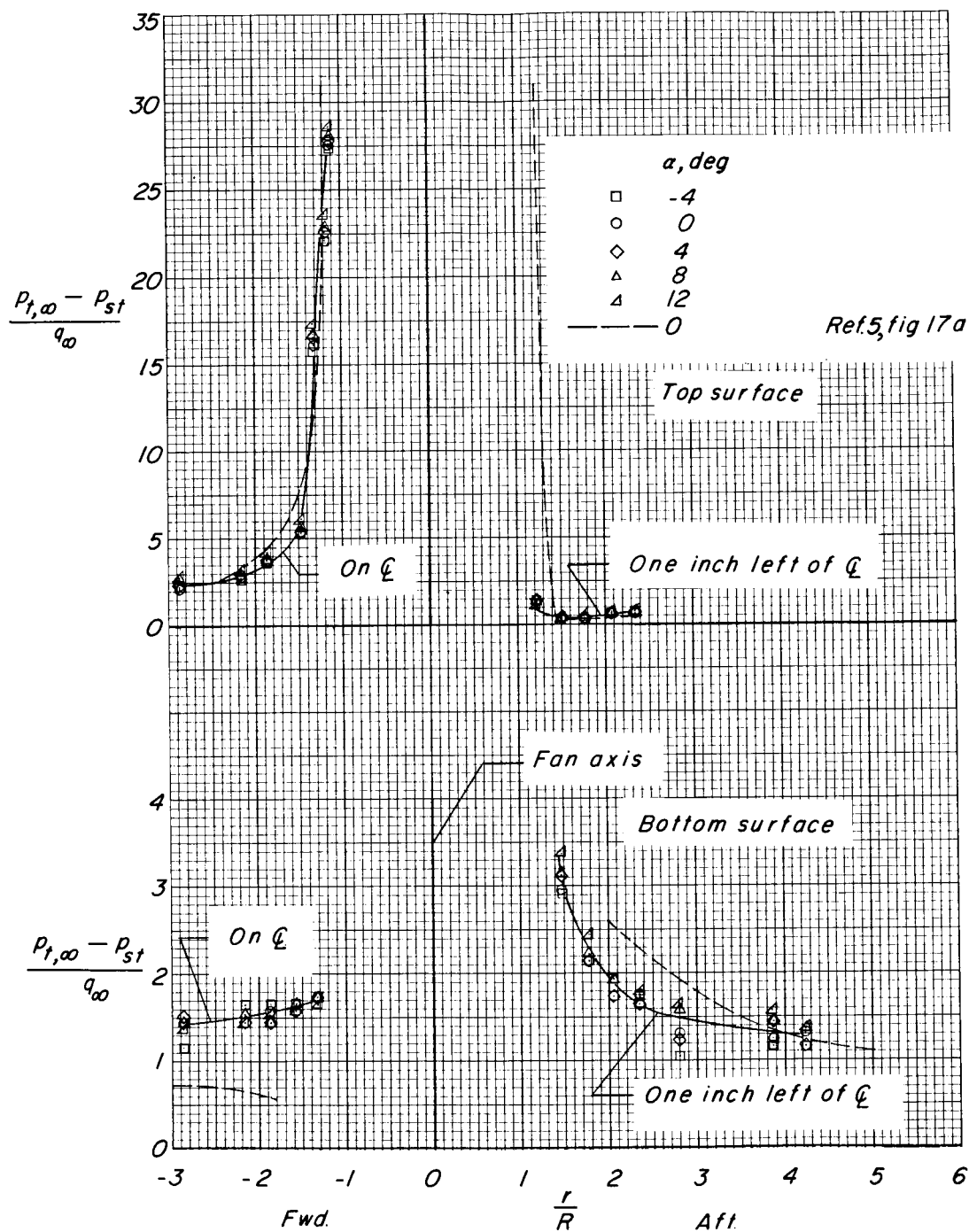
Figure 31.- Longitudinal pressure distribution on fuselage surface for four values of V_∞/V_j at $\delta_v = 35°$. Data from reference 5 were obtained along fuselage center line.
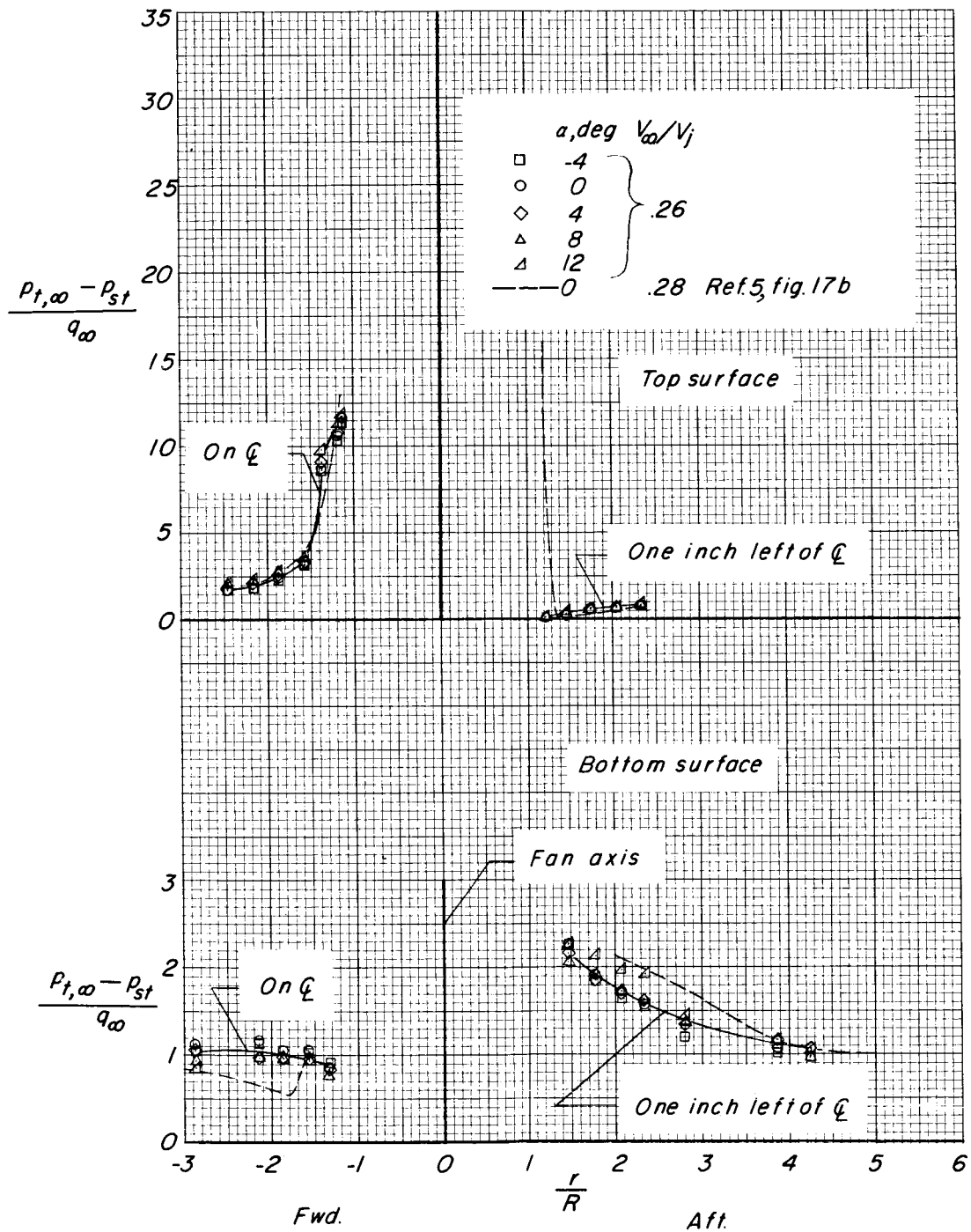
(b) $V_\infty/V_j \approx 0.26$.

Figure 31.- Continued.
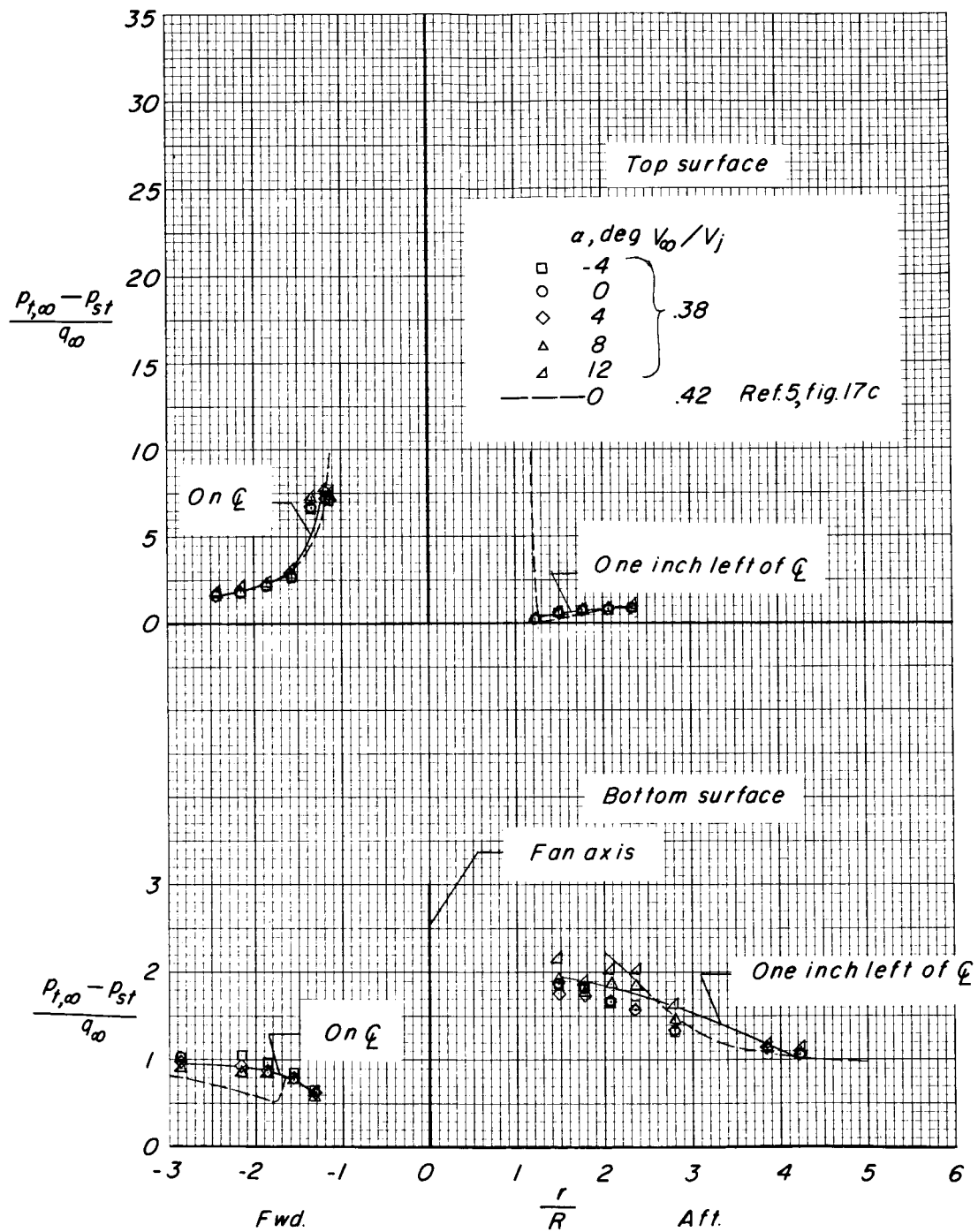
(c) $V_\infty/V_j \approx 0.38$.

Figure 31.- Continued.
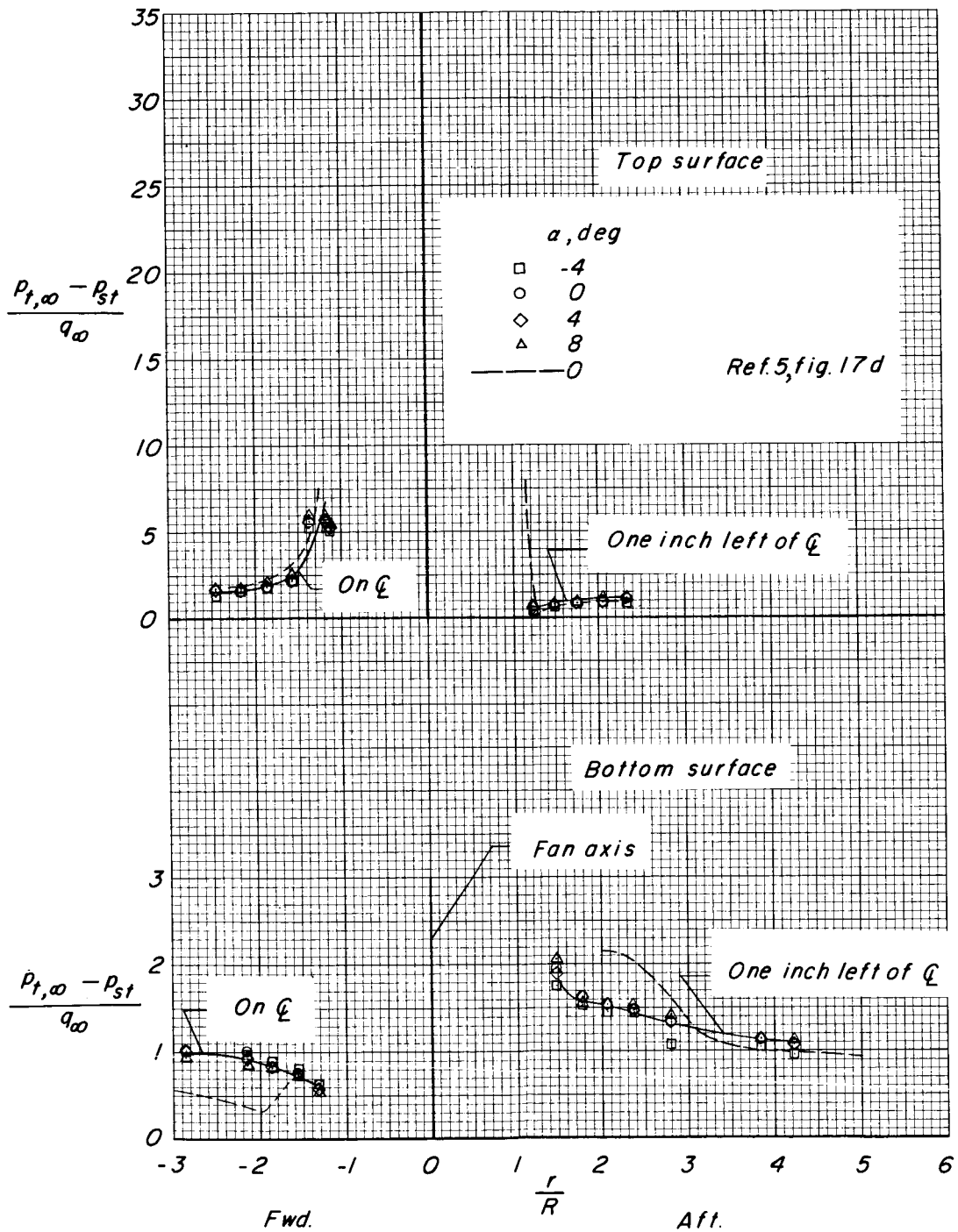
(d) $V_\infty/V_j = 0.53$.

Figure 31.- Concluded.
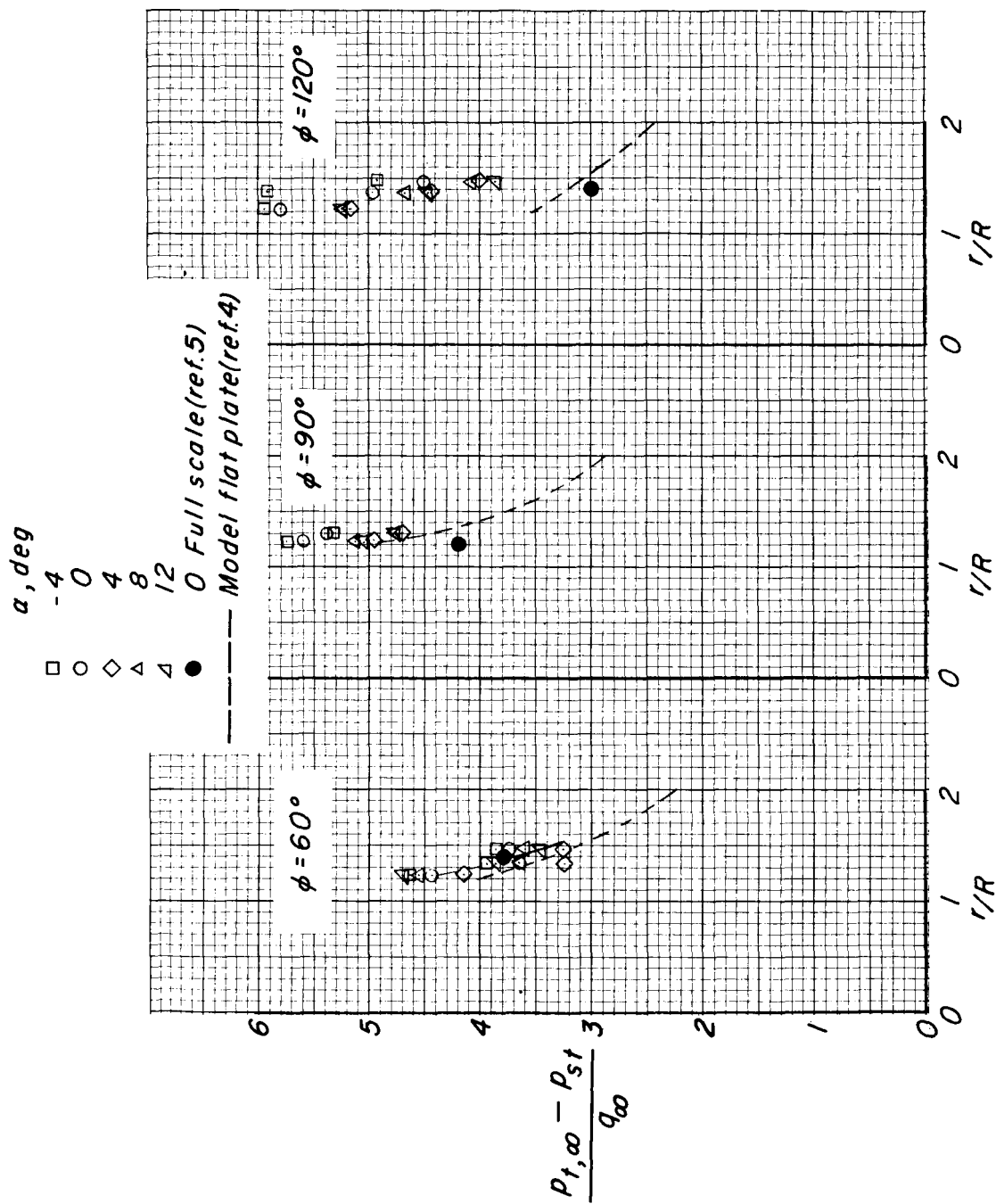
Figure 32.- Pressure distribution at three radial stations on fuselage undersurface. $\delta_v = 0^\circ$.
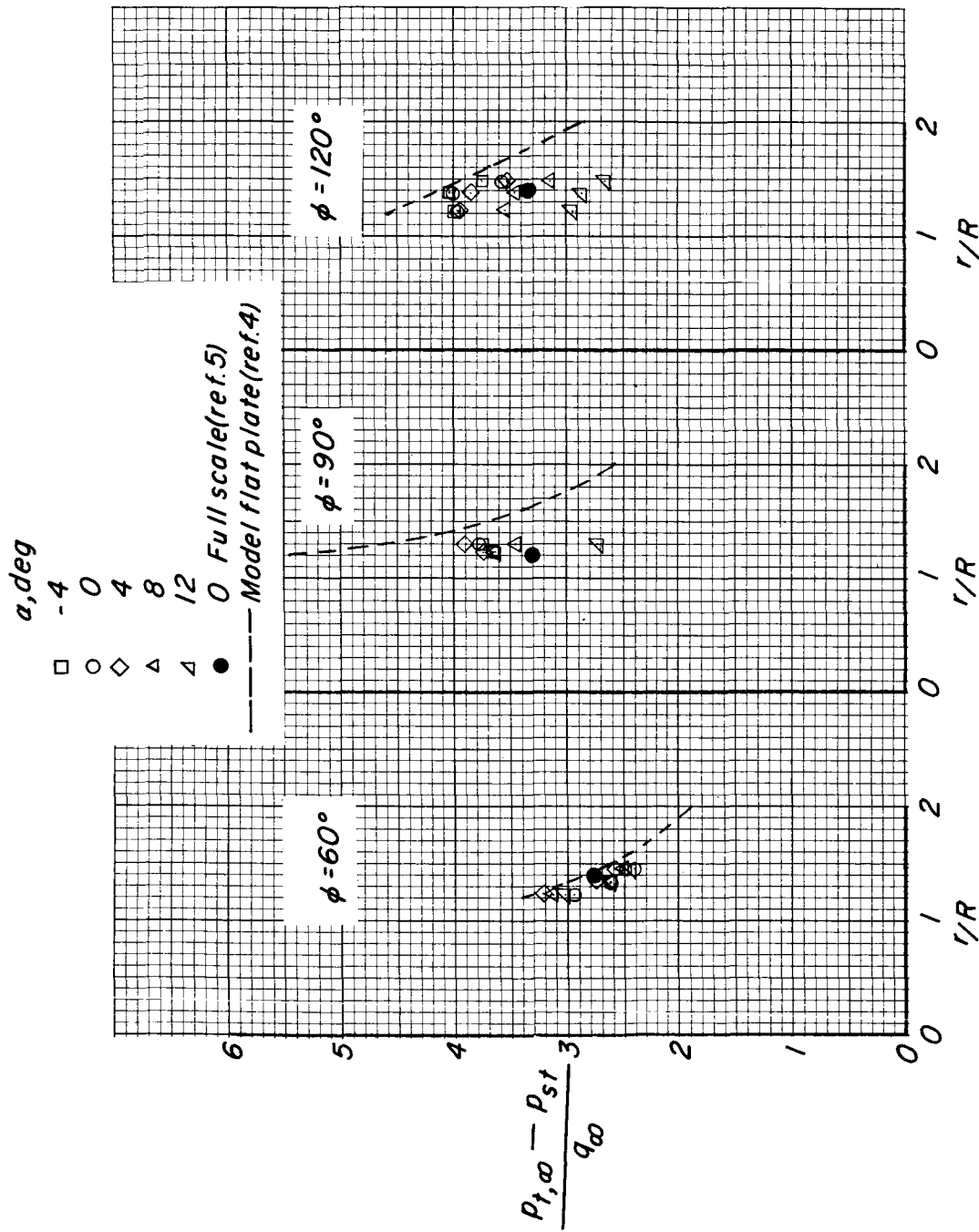
(a) $V_\infty / V_j = 0.15$.

(b) $V_\infty / V_J = 0.26$.

Figure 32.- Continued.

81
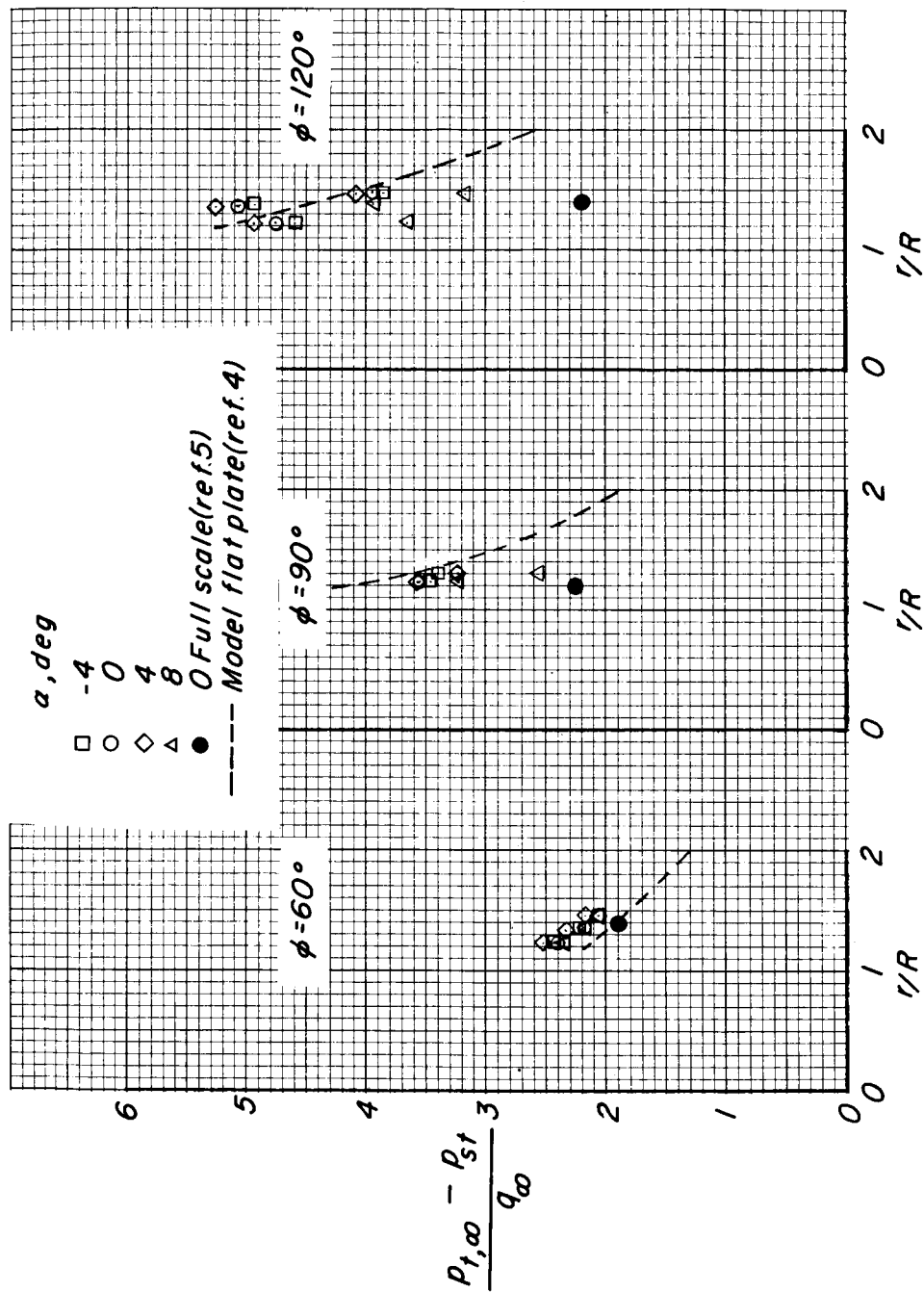
(c) $v_\infty/v_j = 0.38$.

Figure 32.- Continued.
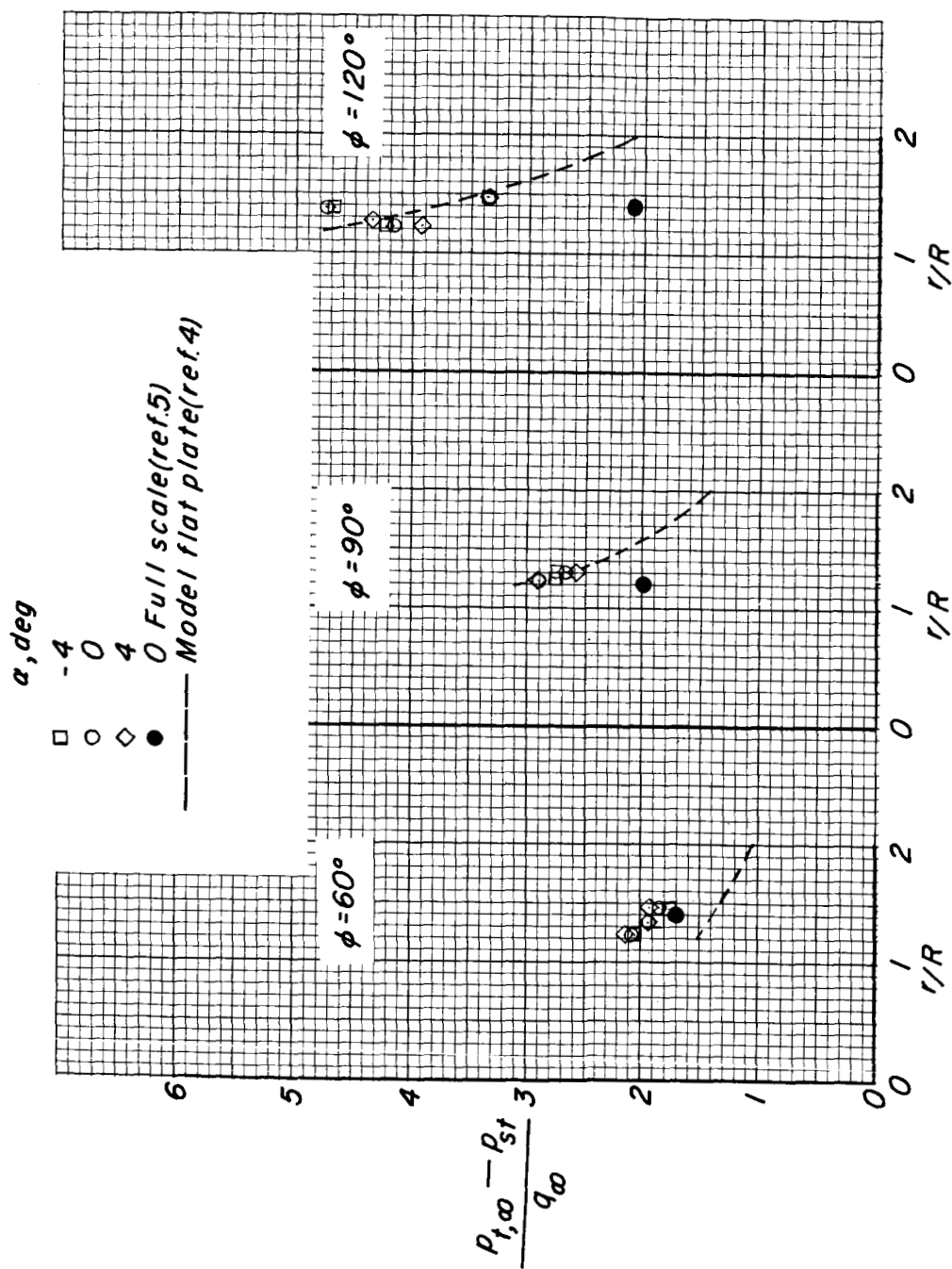
(d) $V_\infty/V_J = 0.53$.

Figure 32.- Concluded.
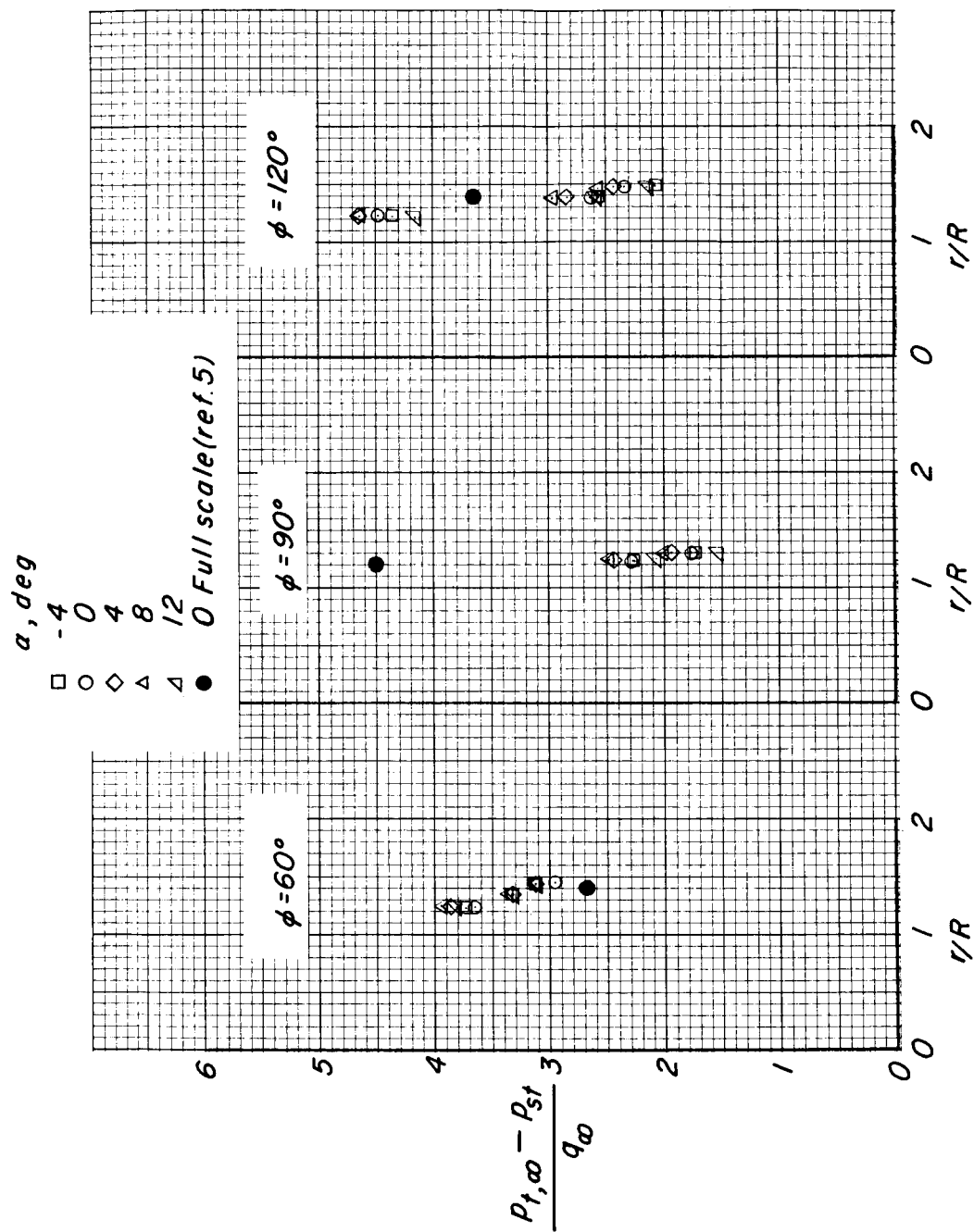
(a) $V_\infty/V_j = 0.15$.

Figure 33.- Pressure distribution at three radial stations on fuselage undersurface. $\delta_v = 20°$.
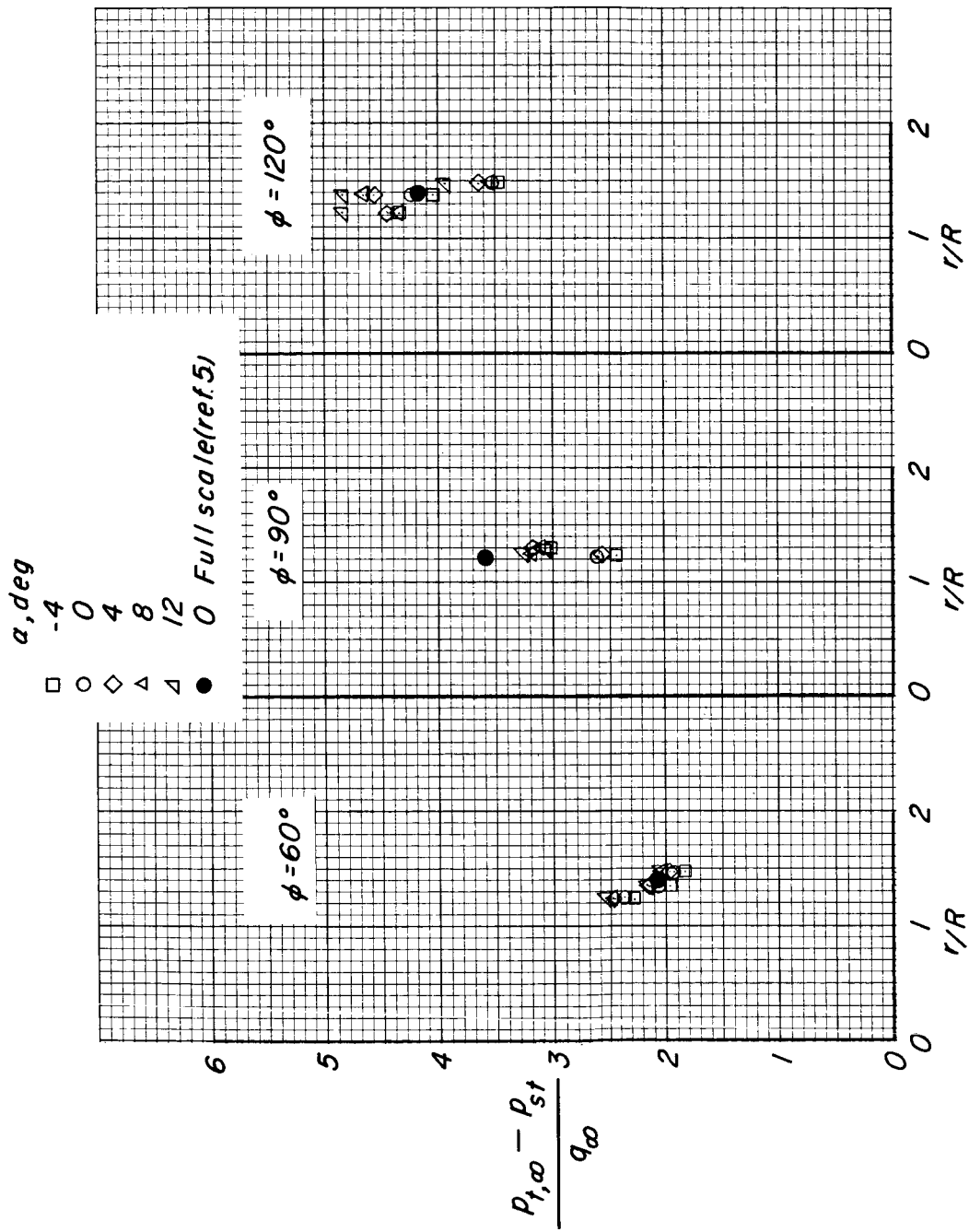
(b) $V_\infty/V_j = 0.26$.

Figure 33.- Continued.
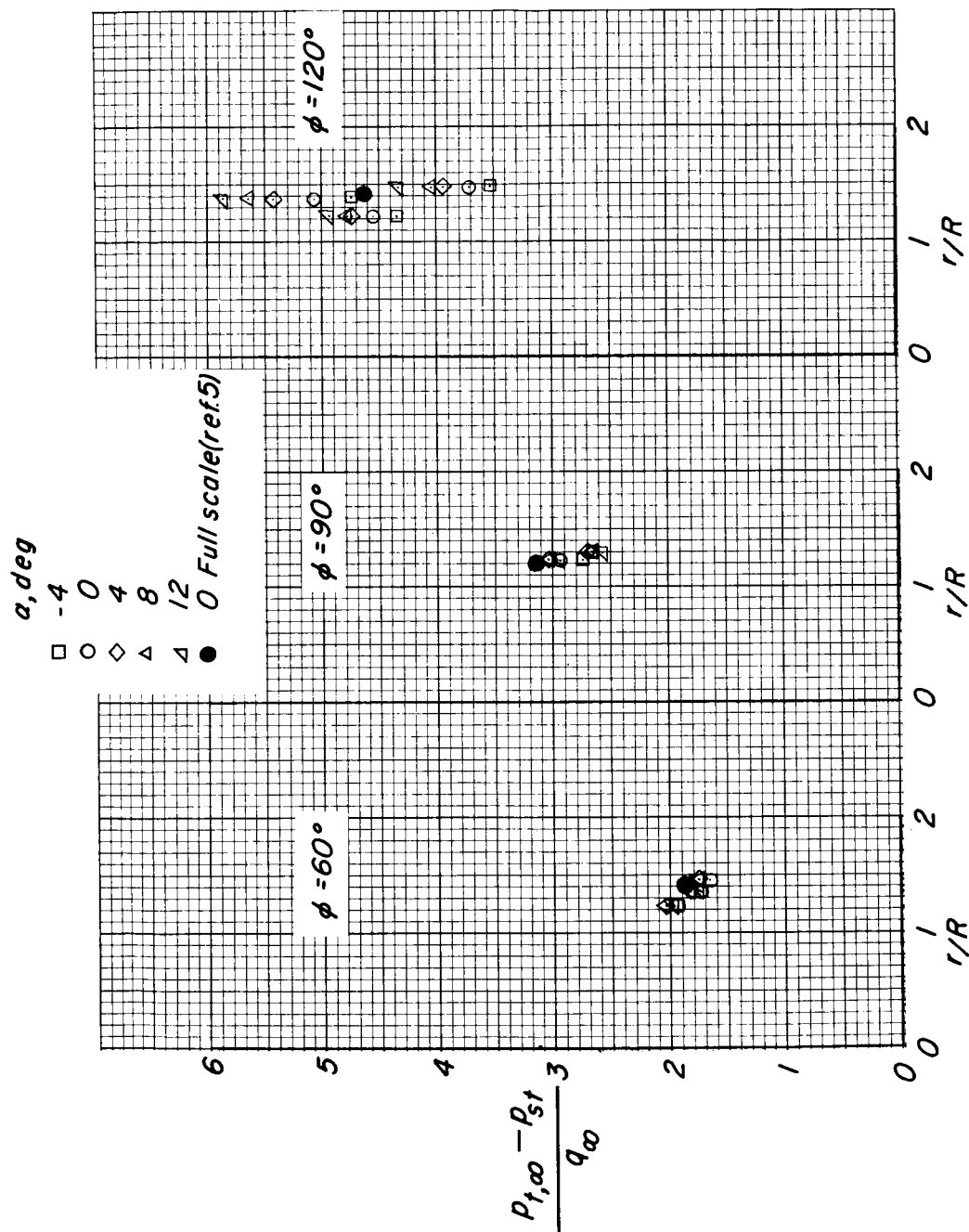
(c) $V_\infty/V_j = 0.38$.

Figure 33.- Continued.

(d) $V_\infty/V_J = 0.53$.

Figure 33.- Concluded.

(a) $V_\infty/V_j = 0.15$.

Figure 34.- Pressure distribution at three radial stations on fuselage
undersurface. $\delta_v = 35°$.
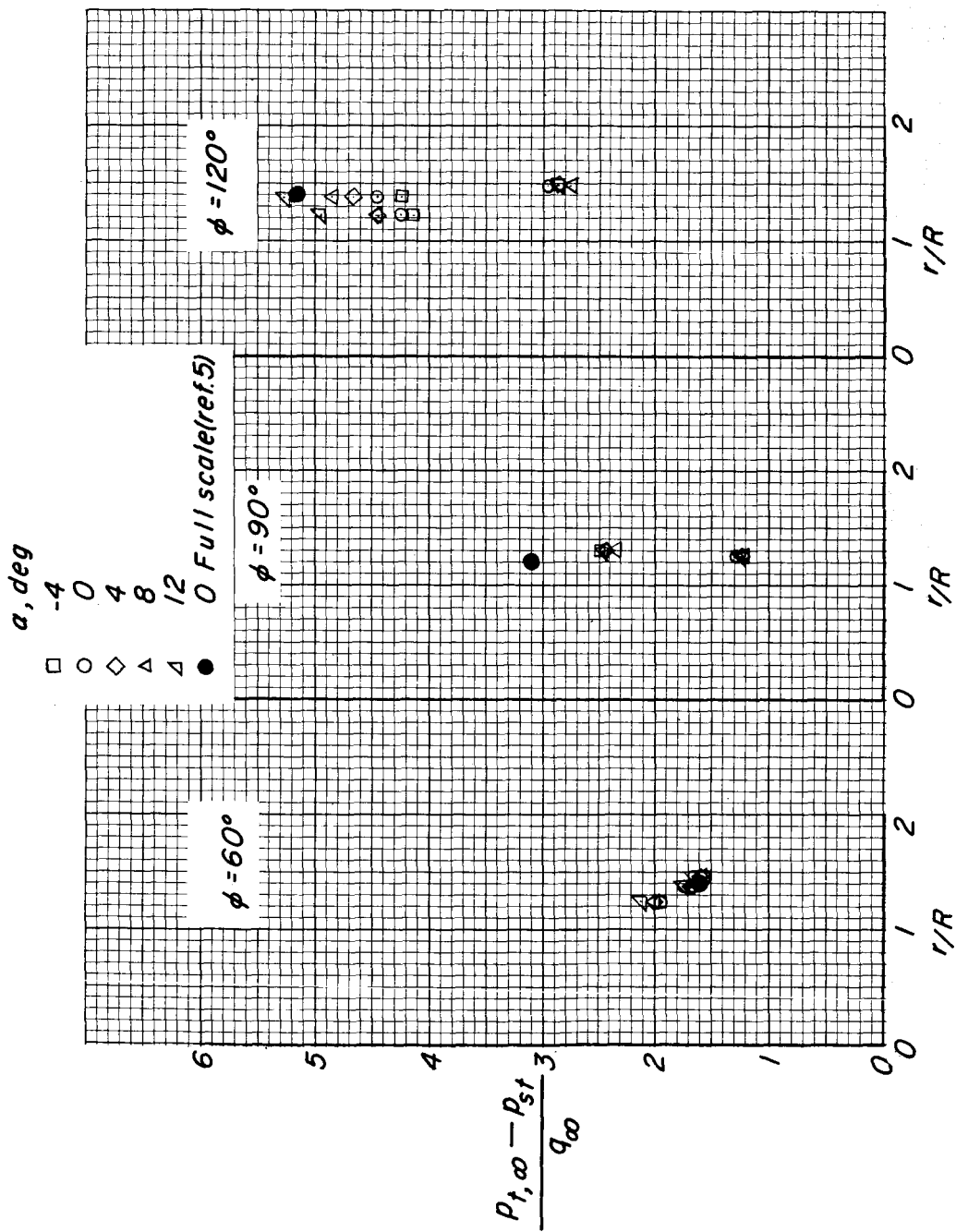
(b) $V_\infty/V_j = 0.26$.

Figure 34.- Continued.

(c) $V_\infty/V_j = 0.38$.

Figure 34.- Continued.
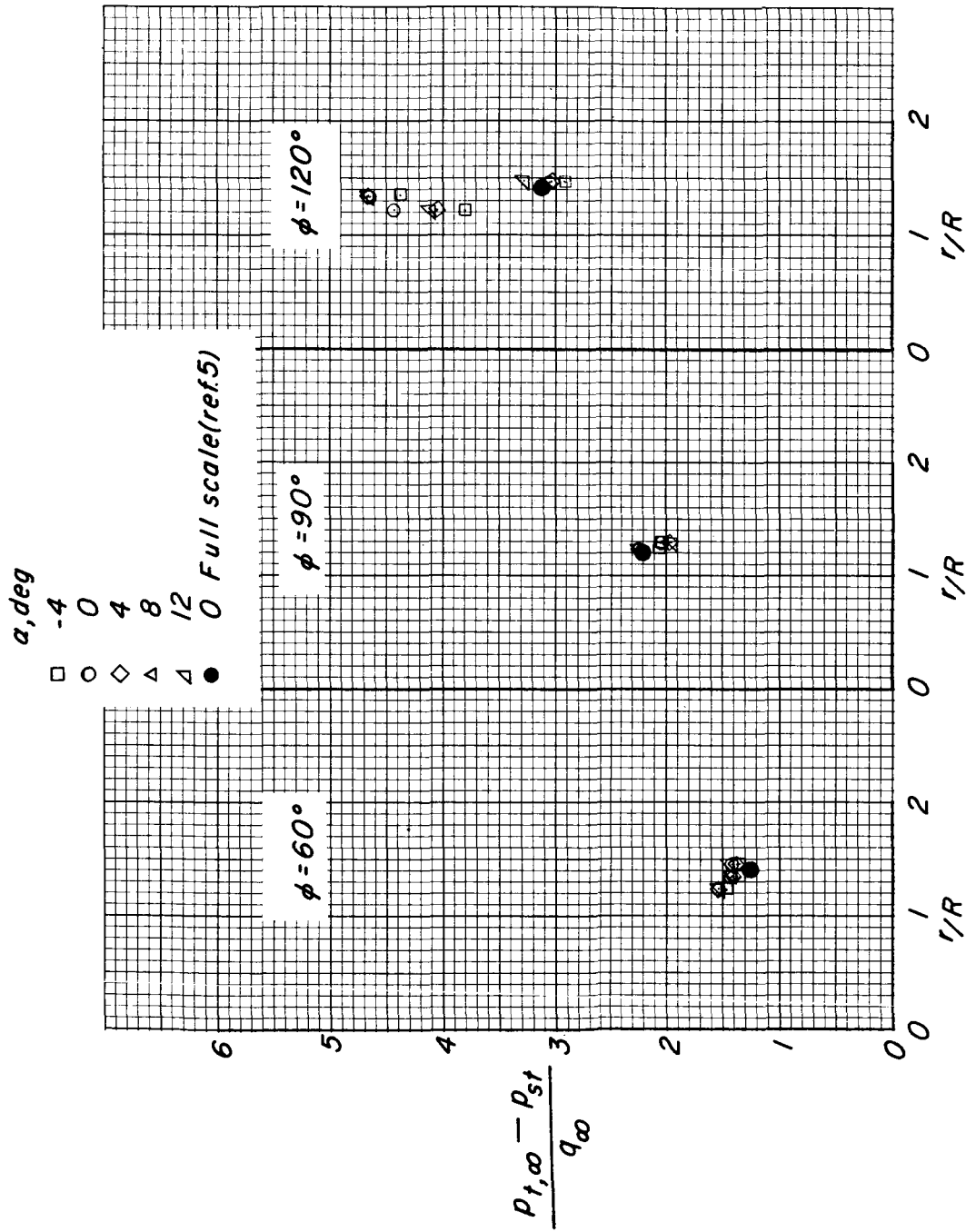
(d) $v_\infty/v_j = 0.53$.

Figure 34.- Concluded.
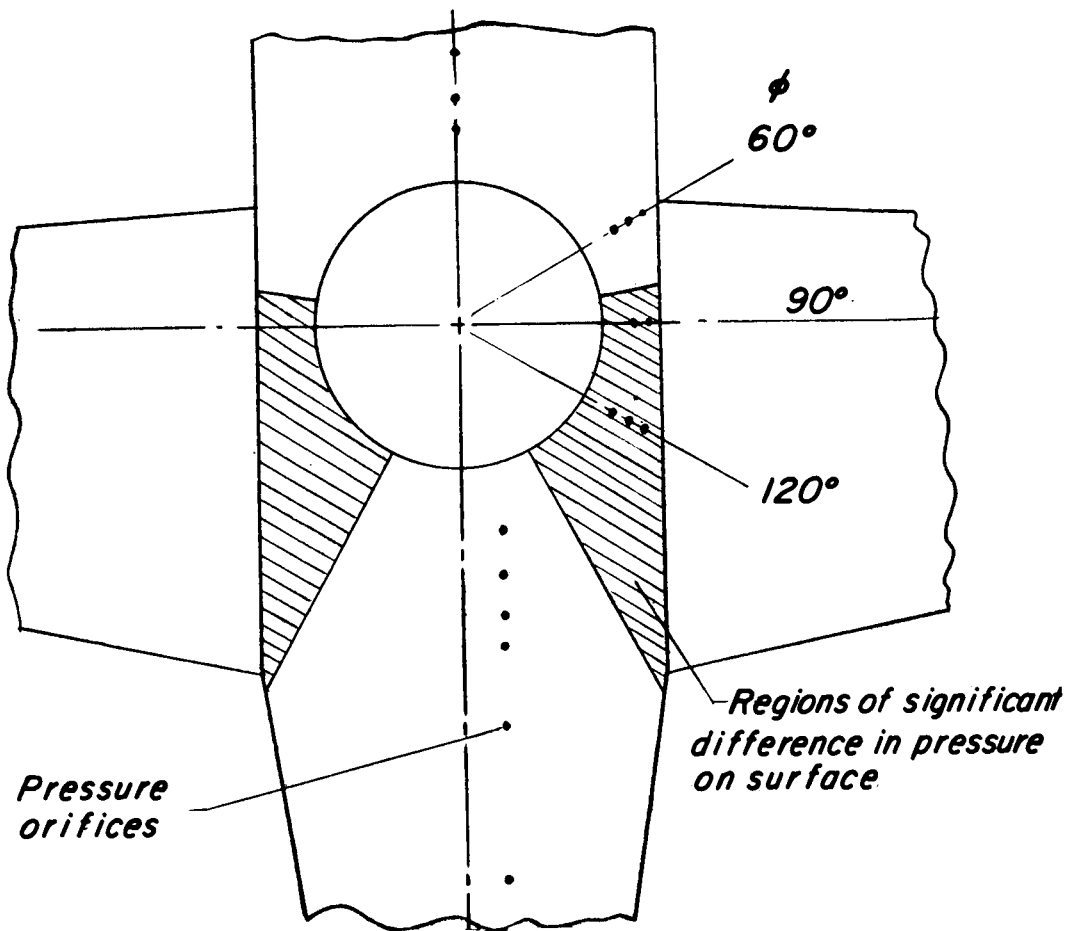
(a) Regions of pressure differences.
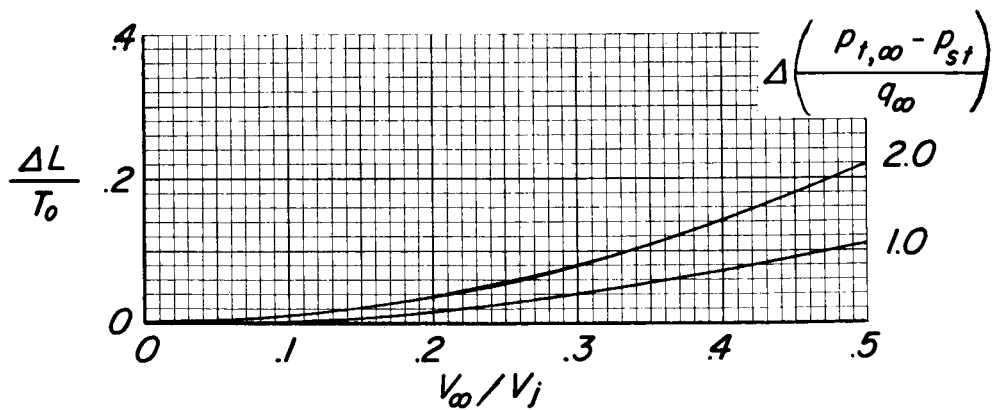
(b) Effect of pressure difference on lift.

Figure 35.- Differences between model and full-scale lower surface pressures. $\delta_v = 0°$.
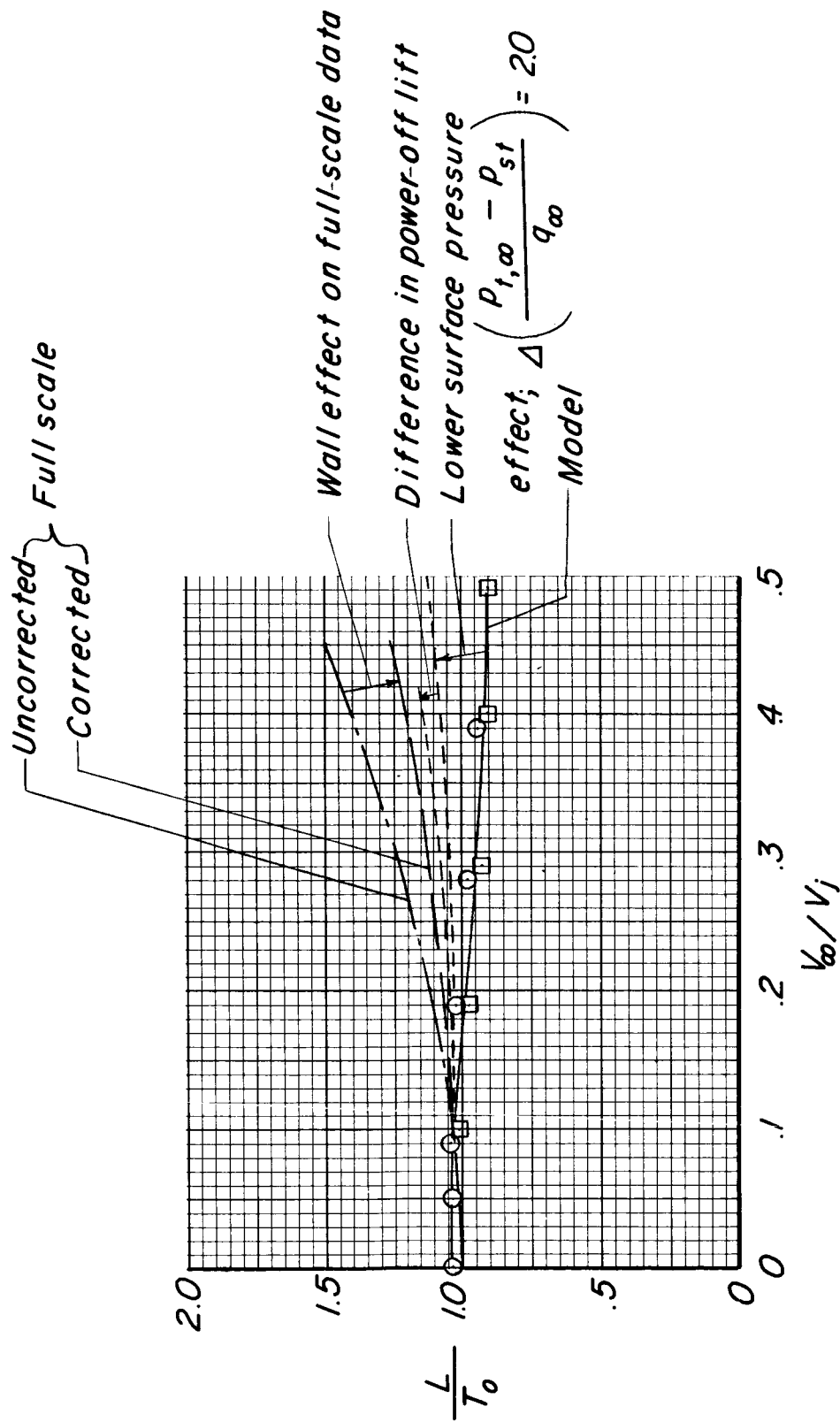
Figure 36.- Summary of factors affecting model and full-scale lift.

93
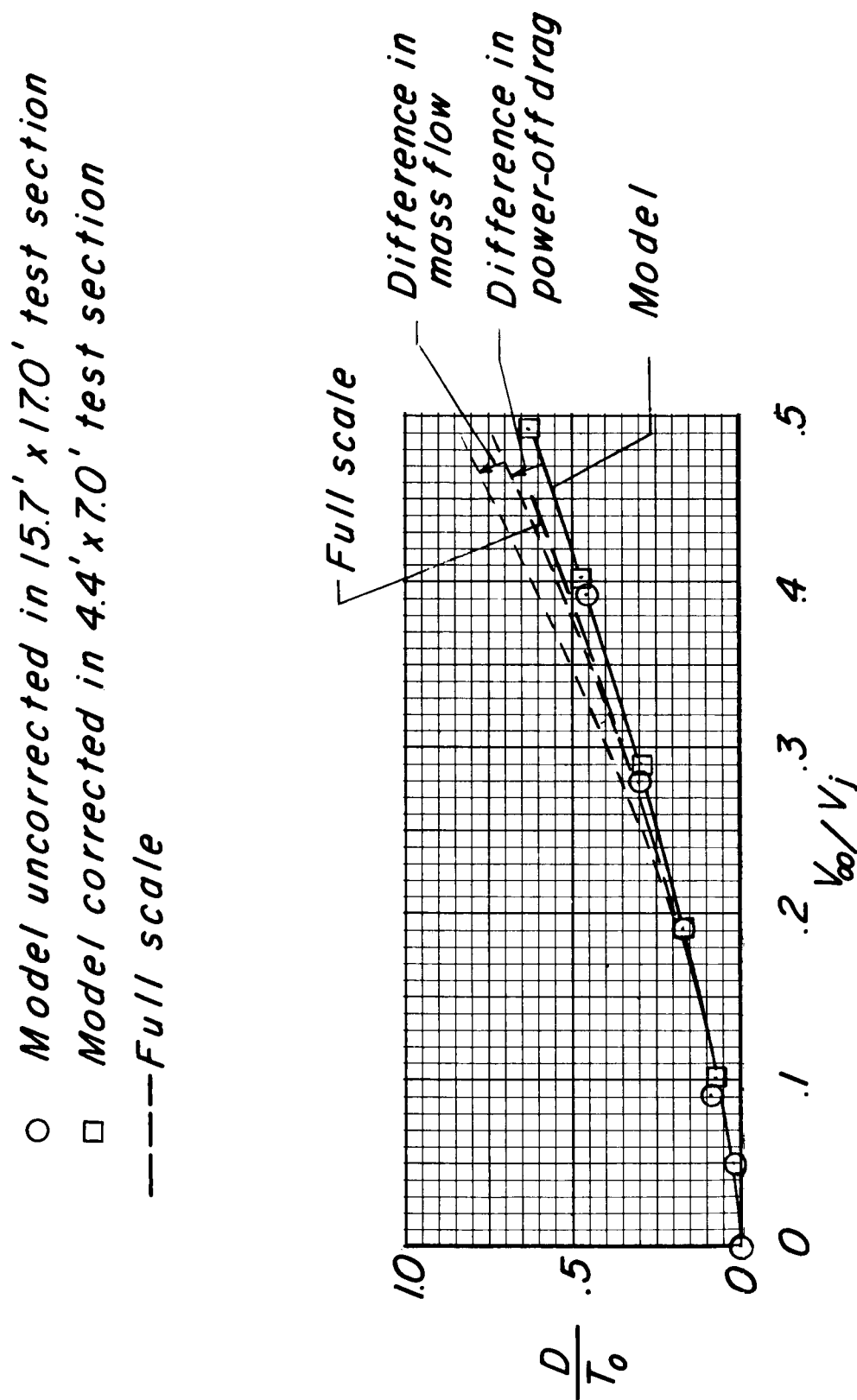
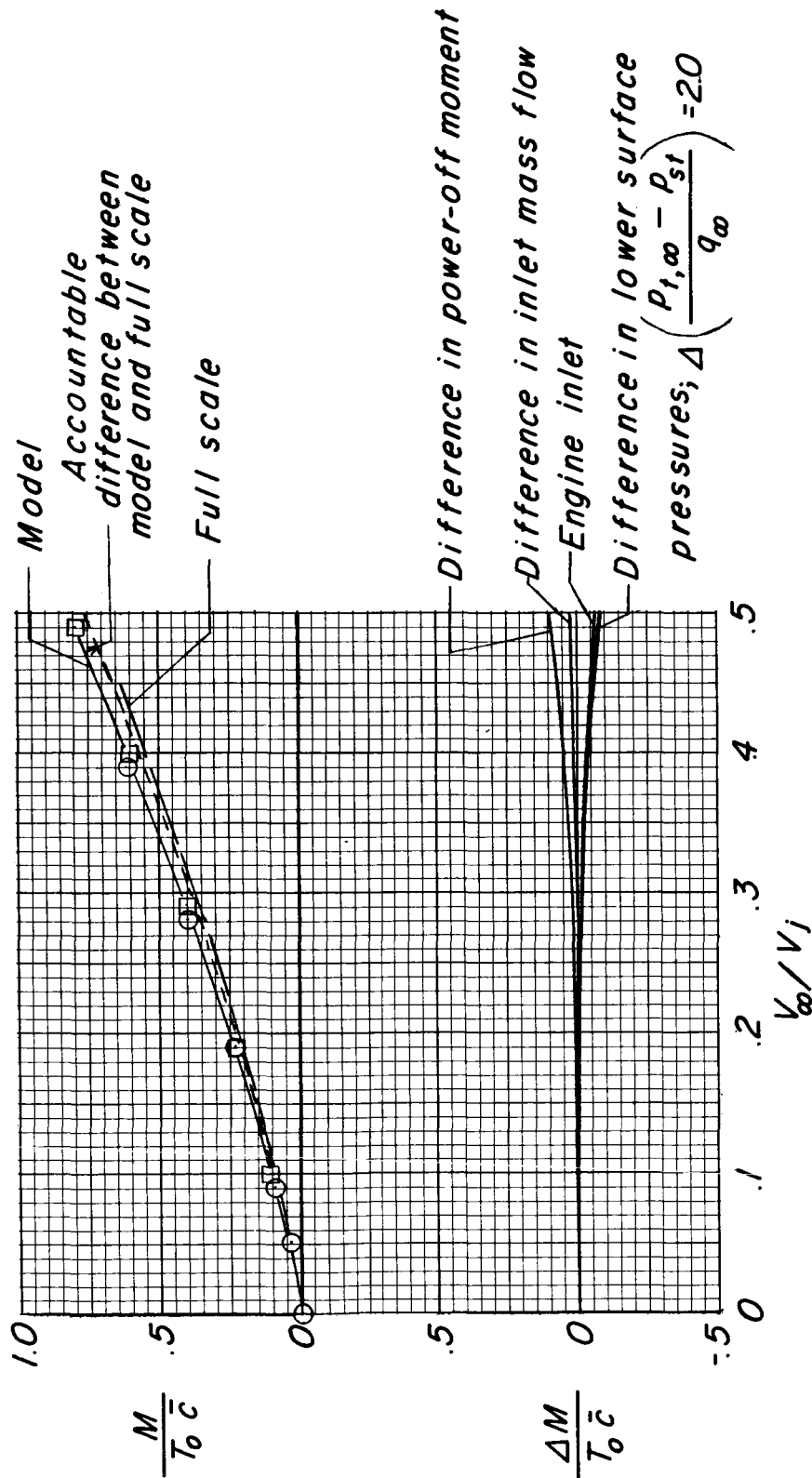Figure 37.- Summary of factors affecting model and full-scale drag.

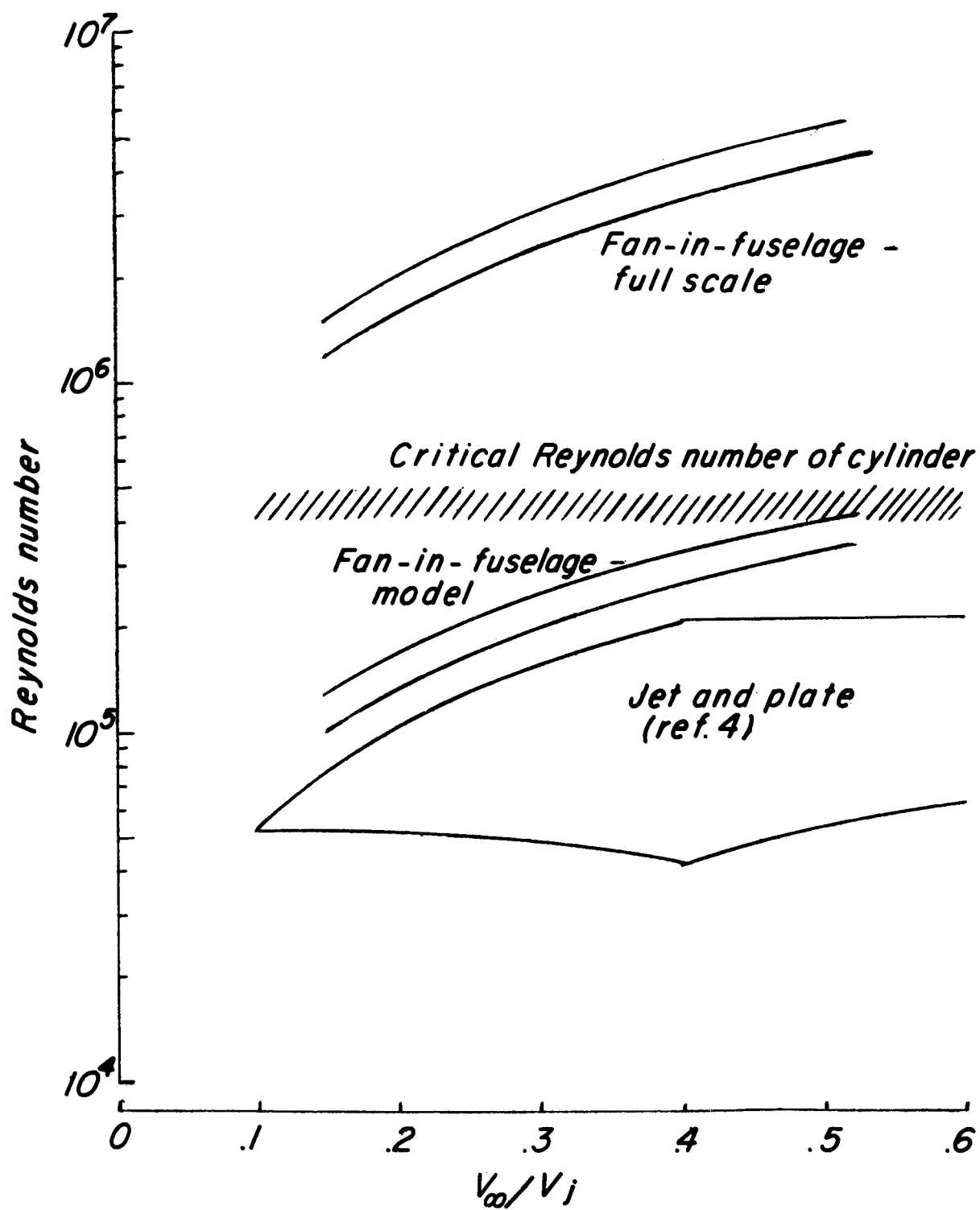Figure 38.- Summary of factors affecting model and full-scale pitching moments.

95

Figure 39.- Comparison of model and full-scale cross-flow Reynolds number. $\alpha = 0^{o}$.
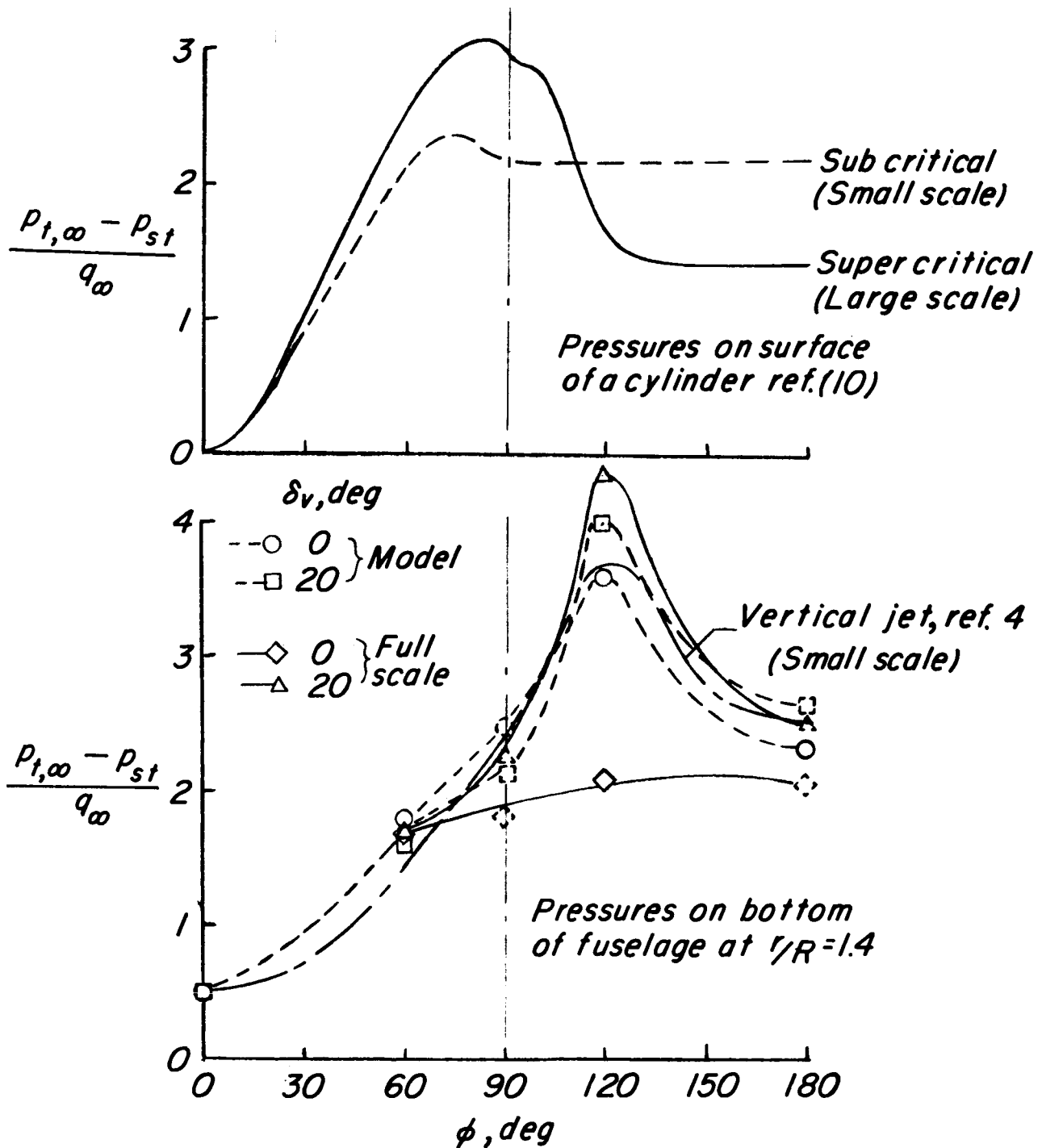
Figure 40.- Comparison of the pressure distribution on a cylinder and the pressures on a surface surrounding a jet at large and small scale. $\alpha = 0°$.